

2010-2011 AIAA Foundation  
Team Aircraft Design Competition



-Proposal-

---



USC Advanced Commercial Concepts Presents:

*Pandion*

University of Southern California

University of California, Los Angeles



**Azadeh Keyvani**  
Member # 280596  
UCLA  
Aerodynamics  
Weight

---

**Elias Montoya**  
Member # 436282  
USC  
Propulsion  
Structures

---

**Keith Homlund**  
Member # 413045  
USC  
Aerodynamics  
High-Lift Mechanism

---

**Todd Erickson**  
Member # 421648  
USC  
Thermal Control  
Aerodynamics (CFD)

---

**Kirsten Gradel**  
Member # 416897  
UCLA  
Aerodynamic Performance  
Configuration

---



**Dr. Geoff Spedding**  
Member # 233796  
USC  
Chairman & Project Advisor

---

**Dr. Ossama Safadi**  
Member # 283128  
USC  
Faculty Advisor

---

**Dr. Ron Blackwelder**  
Member # 1460  
USC  
Industrial Advisor

---

**Aaron Wang**  
Member # 437276  
USC  
Stability & Control  
Flight Dynamics

---

**Shawn Kailath**  
Member # 437297  
USC  
Electrical Systems  
Cost Estimation

---

**Michael Zarem**  
Member # 416621  
USC  
Structures  
Ground Operations

---

**Darin Gaytan**  
Member # 279164  
USC  
Team Manager  
Performance

---

**Sina Golshany**  
Member # 281677  
USC  
Lead Designer  
System Integration

---

**Dr. Jeff Eldredge**  
Member # 199555  
UCLA  
Faculty Advisor

---

## Table of Contents

---

|  |    |
|--|----|
| <b>Nomenclature</b>                                | 4  |
| <b>Acknowledgement</b>                             | 7  |
| <b>Executive Summary</b>                           | 8  |
| <b>Requirements Matrix</b>                         | 10 |
| <b>Configuration Highlights</b>                    | 11 |
| 1.0 <b>Design Methodology</b>                      | 12 |
| 2.0 <b>Preliminary Sizing</b>                      | 13 |
| 2.1 Preliminary Aerodynamic Analysis               | 13 |
| 2.2 Battery Technology Evaluation                  | 14 |
| 2.3 Mission Analysis                               | 15 |
| 2.4 Preliminary Weight Analysis                    | 16 |
| 2.5 Performance Sizing Chart                       | 17 |
| 3.0 <b>Market Analysis</b>                         | 18 |
| 4.0 <b>Configuration Trade-offs</b>                | 20 |
| 4.1 Sensitivity Analysis                           | 20 |
| 4.2 Configuration Selection                        | 21 |
| 5.0 <b>Configuration Description</b>               | 23 |
| 5.1 Fuselage Geometry                              | 23 |
| 5.2 Cockpit & Ergonomics                           | 23 |
| 5.3 Cockpit Access                                 | 25 |
| 5.4 Cargo Stowage                                  | 25 |
| 5.5 Wing Planform, Winglets, and Folding Mechanism | 26 |
| 5.6 Empennage                                      | 27 |
| 5.7 Propeller                                      | 27 |
| 5.8 Electric Motor                                 | 28 |
| 5.9 Landing Gear                                   | 29 |
| 5.10 3-View Foldout                                | 30 |
| 5.11 Inboard Profile                               | 31 |
| 6.0 <b>Aerodynamics</b>                            | 32 |
| 6.1 Airfoil Design                                 | 32 |
| 6.2 Wing Planform Optimization                     | 33 |
| 6.3 Winglets                                       | 35 |
| 6.4 High Lift Devices                              | 35 |
| 6.5 Wetted Area Distribution                       | 36 |
| 6.6 Detailed Drag Polars and Breakdown             | 37 |
| 6.7 Full Airplane CFD Drag Verification            | 38 |
| 7.0 <b>Structural Analysis</b>                     | 42 |
| 7.1 Loads V-n Diagram                              | 42 |
| 7.2 Fuselage Structure                             | 43 |
| 7.3 Landing Gear Attachment and Structure          | 44 |
| 7.4 Wing Structure                                 | 45 |
| 7.5 Wing Flutter Considerations                    | 47 |
| 7.6 Empennage Structure                            | 50 |
| 7.7 Manufacturing Methods                          | 50 |
| 8.0 <b>Propulsion</b>                              | 51 |
| 8.1 Electromotor Type Selection                    | 51 |
| 8.2 Propeller                                      | 51 |
| 9.0 <b>Electrical Systems</b>                      | 54 |
| 9.1 Electrical Storage                             | 54 |
| 9.2 Electric Distribution Architecture             | 55 |

|  |    |
|--|----|
| 9.3 Avionics and Secondary Electrical Components ..... | 55 |
| 9.4 Electric System Foldout .....                      | 57 |
| <b>10.0 Systems Integration</b> .....                  | 59 |
| 10.1 Heat Management .....                             | 59 |
| 10.2 CFD Verifications .....                           | 60 |
| 10.3 Flight Control System .....                       | 62 |
| 10.4 Steering and Brakes .....                         | 63 |
| 10.5 Mechanical Systems Integration Foldout .....      | 64 |
| <b>11.0 Weight Justification &amp; Analysis</b> .....  | 65 |
| 11.1 Detailed Weight Analysis .....                    | 65 |
| 11.2 Class III Weight Estimation .....                 | 66 |
| 11.3 Exploded Weight Group Foldout .....               | 67 |
| 11.4 Center of Gravity Analysis .....                  | 68 |
| <b>12.0 Stability and Control</b> .....                | 69 |
| 12.1 Loading Cases .....                               | 69 |
| 12.2 Balance, CG Travel, and Wing Location .....       | 69 |
| 12.3 Tail Sizing and Trim Diagram .....                | 70 |
| 12.4 Stability & Control Derivatives .....             | 70 |
| 12.5 Aileron Sizing .....                              | 72 |
| 12.6 Dynamic Stability .....                           | 72 |
| 12.7 Propeller Tilting .....                           | 73 |
| <b>13.0 Performance</b> .....                          | 74 |
| 13.1 Performance of Installed Powerplant .....         | 74 |
| 13.2 Takeoff Performance .....                         | 74 |
| 13.3 Climb Performance .....                           | 75 |
| 13.4 Maximum Cruise Speed .....                        | 75 |
| 13.5 Maneuvering Performance .....                     | 76 |
| 13.6 Endurance .....                                   | 76 |
| 13.7 Landing Trajectory .....                          | 77 |
| 13.8 Stall Speed .....                                 | 77 |
| 13.9 Noise Assessment .....                            | 78 |
| <b>14.0 Maintenance &amp; Operations</b> .....         | 79 |
| 14.1 T-Hangar & Storage .....                          | 79 |
| 14.2 Battery Recharging Performance .....              | 80 |
| 14.3 Battery Lifecycle & Replacement .....             | 80 |
| 14.4 Extended Endurance Battery Package .....          | 81 |
| 14.5 Regular Inspections .....                         | 82 |
| 14.6 Accessibility Picture .....                       | 83 |
| <b>15.0 Safety Features and Analysis</b> .....         | 84 |
| 15.1 Deep Stalls and Propeller Tilting .....           | 84 |
| 15.2 Parachute Deployment .....                        | 84 |
| 15.3 G Seats, Seatbelts, and Airbags .....             | 85 |
| 15.4 Wings Folded .....                                | 85 |
| 15.5 Blade Loss .....                                  | 86 |
| 15.6 Lightning Strike .....                            | 86 |
| <b>16.0 Cost &amp; Risk Analysis</b> .....             | 87 |
| 16.1 Market Forecast .....                             | 87 |
| 16.2 Project Risk Assessment .....                     | 87 |
| 16.3 Itemized Cost Estimation .....                    | 88 |
| 16.4 Operating Cost .....                              | 91 |
| <b>References</b> .....                                | 92 |

## Nomenclature

|                                       |  |
|---------------------------------------|--|
| $\alpha$                              | Angle of attack  |
| $AR_W$                                | Wing aspect ratio  |
| $AR_S$                                | Reference Aspect Ratio   |
| $\bar{\gamma}$                        | Average flight path angle  |
| $C_a/C_w$                             | Aileron chord to wing chord ratio                                    |
| $C_D$                                 | Airplane drag coefficient  |
| $C_{D0_{TO}}, C_{D0_{clean}}$         | Airplanes zero-lift drag coefficient at takeoff, clean configuration |
| CGR                                   | Climb Gradient   |
| $C_{L_{maxS(Clean)}}$                 | Maximum lift coefficient for clean stall configuration               |
| $C_{L_{maxTO}}$                       | Maximum lift coefficient at takeoff                                  |
| $C_{L_{opt,MaxR}}$                    | Lift coefficient correspond to the optimum range performance         |
| $C_{l_a}$                             | Airplane rolling-moment-coefficient due to ailerons deflection       |
| $C_{m_a}$                             | Airplane pitching-moment-coefficient-due-to-AOA derivative           |
| $C_{m_T(PT)}$                         | Airplane moment-coefficient-due-to-thrust-from-prop-tilting          |
| $C_{l_\beta}$                         | Airplane rolling-moment-coefficient-due-to-yaw rate-derivative       |
| $C_{n_\beta}$                         | Airplane yawing-moment-coefficient-due-to-side-slip-derivative       |
| $C_p$                                 | Coefficient of Pressure  |
| $D_p$                                 | Diameter of the propeller  |
| $\Delta_h$                            | Change in altitude   |
| $f(AR)$                               | Function of Aspect Ratio   |
| $F_{MTOW}$                            | Fraction of Takeoff Weight   |
| $\zeta_{P, long}$                     | Longitudinal phugoid mode damping ratio                              |
| $\zeta_{SP}$                          | Short period mode damping ratio                                      |
| $\eta_{i_j}$                          | Flap inboard station, in term of wing half span                      |
| $\eta_{O_f}$                          | Flap outboard station, in term of wing half span                     |
| $I_{\infty_B}, I_{y_B}, I_{\infty_B}$ | Moment of inertia along the body axis                                |
| $Level_p$                             | Level for phugoid stability  |
| $Level_{\xi_{SP}}$                    | Level for short period damping                                       |
| $L/D _{TO}$                           | Lift-to-Drag ratio at takeoff  |
| $\lambda_w$                           | Wing taper ratio   |
| $\Lambda_w$                           | Wing sweep angle   |
| $\Lambda_{LE}$                        | Leading edge wing sweep  |
| $NP_{free}$                           | Free stick neutral point   |
| $n_{pull-up}$                         | Load factor during pull-up maneuver                                  |
| $n_{turn}$                            | Load factor during turning maneuver                                  |
| $P_{SpExPwr}$                         | Specific Excess Power  |
| $\Pi_{TO}$                            | Throttle setting at takeoff  |
| $Q_1$                                 | Dynamic Pressure   |
| R/C                                   | Rate of climb  |
| $R_{turn}$                            | Radius of maneuvering turn   |

|  |   |
|--|---|
| $S_{air}$                                      | Distance from obstacle height to the point of touchdown   |
| $S_L$  | Landing distance  |
| $S_{LG}$                                       | Ground roll landing distance  |
| $SM_{fee}$                                     | Stick free static margin  |
| $S_{TO}$                                       | Total field length  |
| $S_{TOG}$                                      | Take-off ground run distance  |
| $S_W$  | Wing surface area   |
| $SM$   | Static margin   |
| $t(1 \rightarrow 3)$                           | Time to climb   |
| $T_{\gamma_{2p}}$                              | Time to half amplitude in phugoid mode  |
| $T_{avail}$                                    | Thrust available  |
| $T_{req}$                                      | Thrust required   |
| $V_A$  | Approach speed  |
| $V_{CrMax}$                                    | Maximum cruise speed  |
| $V_D$  | Dive Velocity   |
| $V_{flutter}$                                  | Flutter velocity for a finite aspect ratio  |
| $V_{LOF}$                                      | Speed at liftoff  |
| $V_m$  | Speed in maneuver   |
| $V_{NE}$                                       | Never exceed velocity   |
| $V_o$  | Flutter velocity for an infinite aspect ratio   |
| $V_s$  | Stall speed   |
| $V_{SL}$                                       | Landing stall speed   |
| $V_{S_{TO}}$                                   | Takeoff stall speed   |
| $W_E$  | Empty weight  |
| $W_{fix}$                                      | Weight of Fixed Equipment   |
| $W_{PL}$                                       | Weight of the payload   |
| $W_{PP}$                                       | Weight of the powerplant  |
| $W_{Structure}$                                | Weight of the structure   |
| $W_{TO}$                                       | Takeoff weight  |
| $W_{TO,Extended}$                              | Takeoff weight, extended mission  |
| $W_{TO,Light}$                                 | Takeoff weight, light mission   |
| $(W/S)_{TO_{max}}$                             | Maximum take-off wing loading   |
| $(W/T)_{TO_{max}}$                             | Maximum take-off power loading  |
| $\varphi$                                      | Thrust vector inclination with respect to freestream airflow  |
| $X_{apex_W}$                                   | X coordinate of the wing apex (i.e. distance b/w wing quarter chord station and the nose reference point) |
| $\bar{x}_{ac}, \bar{x}_{ac_w}, \bar{x}_{ac_b}$ | X coordinate of aerodynamic center in terms of mean aerodynamic chord                                     |
| $X_{CG}, Y_{CG}, Z_{CG}$                       | Location of center of gravity   |
| $\bar{x}_{cg}$                                 | X coordinate of center of gravity in terms of mean aerodynamic chord                                      |
| $\omega_{n_P, long}$                           | Longitudinal phugoid mode undamped natural frequency  |
| $\omega_{n,S.P}$                               | Short period undamped natural frequency   |

## Acronyms:

|            |  |
|------------|--|
| AAA        | Advanced Aircraft Analysis                                     |
| AIAA       | American Institute of Aeronautics and Astronautics             |
| CAD        | Computer Aided Design  |
| AR         | Aspect Ratio   |
| CFD        | Computational Fluid Dynamics                                   |
| CFRP       | Carbon-fiber reinforced plastics                               |
| <i>cfm</i> | Cubic Feet per Minute  |
| CG         | Center of Gravity  |
| DOC        | Direct Operating Cost  |
| DSM        | Design Structure Matrix  |
| EPNdB      | Effective Perceived Noise in Decibels                          |
| ESDU       | Engineering Sciences Data Unit                                 |
| EIS        | Entry into Service Date  |
| ERP        | Extended Range Pack  |
| FAA        | Federation Aviation Administration                             |
| FAR        | Federal Air Regulation   |
| FEA        | Finite Element Analysis  |
| <i>fpm</i> | Feet per minute  |
| GAMA       | General Aviation Manufacturers Association                     |
| ISA        | International Standard Atmosphere                              |
| L/D        | Lift-to-Drag Ratio   |
| LAMA       | Light Aircraft Manufacturers Association                       |
| LSA        | Light Sport Aircraft   |
| MFD        | Multi-Function Display   |
| MLW        | Maximum Landing Weight   |
| NLF        | Natural Laminar Flow   |
| RDTE       | Research Development Testing and Evaluation                    |
| RFP        | Request for Proposal   |
| RPM        | Revolutions per Minute   |
| SAE        | Society of Automotive Engineers                                |
| SAR        | Specific Air Range   |
| S-LSA      | Special Light Sport Aircraft                                   |
| UACC       | University of Southern California Advanced Commercial Concepts |
| USAF       | United States Air Force  |



## Acknowledgement

We would like to express our appreciation for the help and support given by the faculty of USC's Aerospace and Mechanical Engineering department. First of all, we wish to thank the people who were integral to the creation of this project: *Dr. Geoff Spedding*, *Mr. Blaine Rawdon*, and *Mr. Mark Page*. With their experience in the field of aircraft design, they have been very supportive in all the phases of this project. During the first year of his retirement, *Dr. Ron Blackwelder* contributed greatly to all aspects of this project, including organizational support for team members. *Dr. Daniel P. Raymer*, president of the *Conceptual Design Corporation*, also contributed greatly by providing well needed advice and feedback. Special thanks are also due to *Marc Aubertine* in USC's engineering writing program for his contribution to the organization and composition of this proposal. During the development of this aircraft, UACC was provided with information regarding subsystem components and technologies presently under development in various fields: *Martin Gabrielsson*, CIO of *Amapola Flyg*, Sweden, provided great information regarding the present development of an iPad based avionics cluster. *Dr. Lutgard C. De Jonghe*, Faculty Senior Scientist at Lawrence Berkeley National Labs and *Dr. Binod Kumar*, from the University of Dayton Research Institute, provided UACC with critical information regarding the advancements in Lithium-Air battery technology. Also, great mentorship was provided by *Mr. Marty Bradley* of *The Boeing Company* with regard to electric aircraft architecture and subsystems.

We would also like to express appreciation for faculty and staff both at USC and UCLA, whose contributions made this project possible. Firstly, USC's Aerospace Engineering Department faculty and staff including *Dr. David Wilcox*, *Dr. Hai Wang*, *Samantha Graves*, *David Salter*, and *Silvana Martinez-Vargas* contributed greatly by providing organizational support. *Dr. Jeff D. Eldredge*, Associate Professor of UCLA's Department of Aerospace and Mechanical Engineering, assisted the team with regard to aerodynamic design. Last but not least, we wish to give thanks to all our friends and family for being there, providing both an understanding and supportive attitude in a multitude of ways.

May 2011, Los Angeles  
USC's Advanced Commercial Concepts Team

## Executive Summary

**D**ue to improvements in methods of production and design, owning a Special Light Sport Aircraft (S-LSA) has become increasingly popular over the past few years. However, with the expected increase in oil prices plus stricter environmental regulations, the ever rising operating cost limits the market for this type of aircraft. Through the recent advancements in electric motor design and battery technologies, new avenues are enabled for the next generation of S-LSAs which allow them to be more affordable, more reliable, and safer than models presently in production.

This proposal describes the design of Pandion, a fully electric S-LSA which implements state of the art electric propulsion technology as well as innovative features, promising an overall reduction in the operating cost through the elimination of the dependency on aviation fuel. Pandion also implements a specialized prop-tilting mechanism to improve its safety in recovering from a deep stall (a situation not uncommon with S-LSAs). As with all aircraft designs, emphasis is placed on obtaining a fail-safe configuration that complies with industry and federal standards for Light Sport Aircraft.

From the standpoint of aerodynamic configuration, Pandion utilizes high aspect ratio folding wings that provide compatibility with current airport infrastructure while increasing overall aerodynamic efficiency. Natural laminar flow technologies, verified using high resolution Computational Fluid Dynamics (CFD) simulations, are employed heavily in order to further reduce the friction drag produced by the airframe. The high aspect ratio wing planform dictates a need for particular attention to the structural design of the wing components to avoid aero-elastic flutter. Numerical methods and tools were developed to accomplish this task and ensure that the speed at which flutter of the wing structure occurs is well above the maximum speed anticipated in the flight envelope for Pandion. Carbon fiber composite components were used extensively throughout the structure enabling substantial weight reductions, as well as making the high aspect ratio wing planform structurally feasible.



Pandion features a specially designed, high performance Lithium-Air battery package, with the configuration providing room for an additional battery unit for extended-range missions. The electrical circuit and power management system has been fully designed and analyzed, enabling the accurate quantification of energy consumption and heat generation at each component to be addressed by the thermal management system.

During the conceptual design phase of the project, it was realized that the utilization of a fully electric power architecture presents difficulties with respect to thermal management. Due to limited volume and large amounts of dissipated heat, as well as the inherent inefficiency of composite structures in conducting thermal energy, design and implementation of effective heat management solutions received significant attention. High fidelity numerical tools were utilized to perform thermal simulations ensuring the effectiveness of the designed system even in the most critical flight scenarios.

As the intended users of the aircraft include aviation enthusiasts and private pilots who would use the aircraft for leisure purposes, particular attention was paid to the ergonomics of the cockpit interior, payload compatibility, and occupant visibility. Further, noise reduction played a decisive role in determining the technology level for the propeller system integrated into the design.

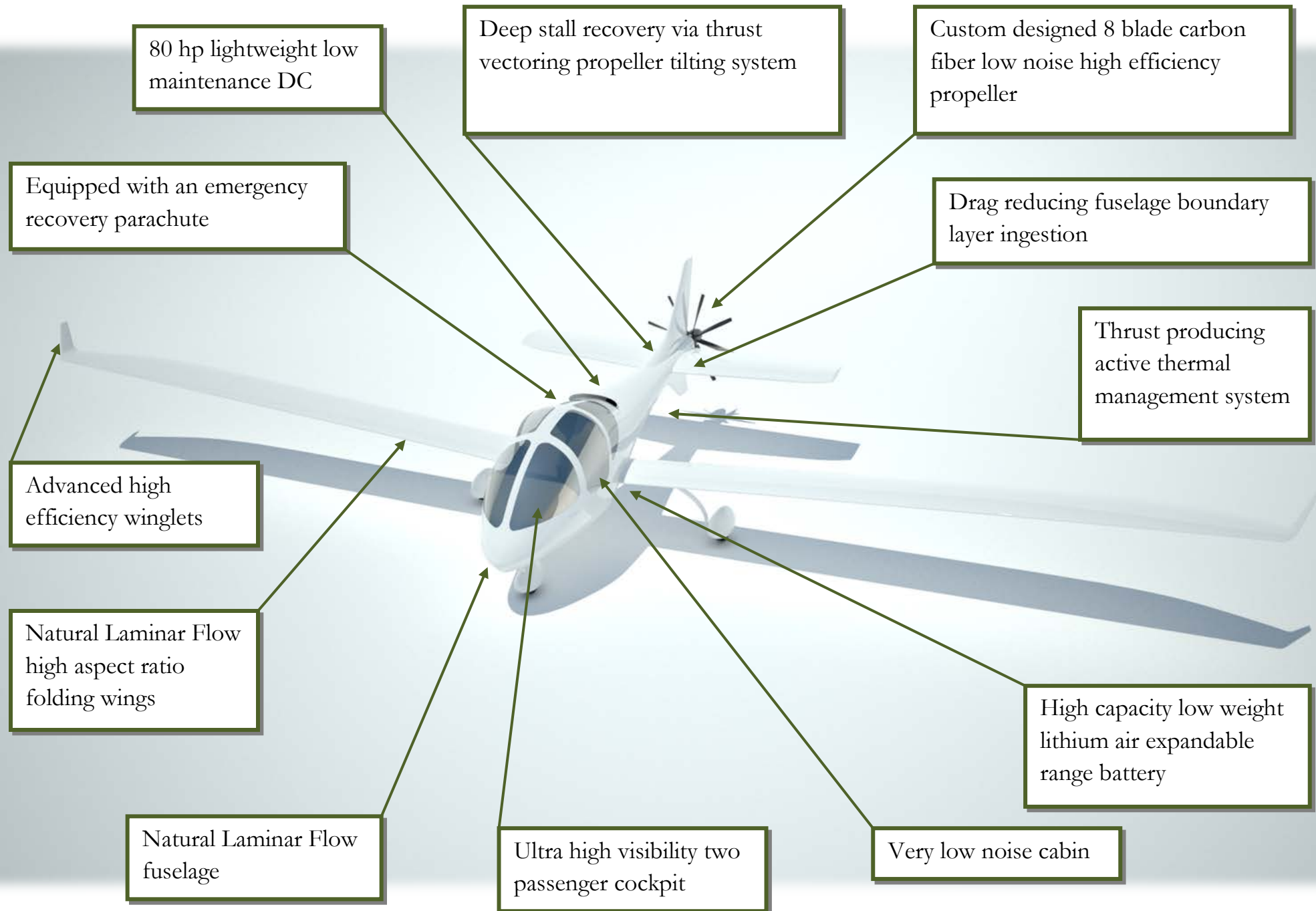
A wide variety of expertise was utilized due to the large number of disciplines involved and the high level of detail intended for the project. Team members from the University of Southern California, University of California, Los Angeles, and California State University, Los Angeles majoring in Aerospace Engineering, Mechanical Engineering, Electrical Engineering, Computer Science, and Physics collaborated on various aspects of the project to develop the final design.

Given the high level of detail considered and the high fidelity of the analysis methods utilized, it is the unilateral belief of UACC that Pandion represents an astute blend of design innovation, technology integration, and cost effectiveness presently unmatched by any similar craft in the market.

# Requirements Matrix

**Table 1. Selected design parameters**

| Parameter   | Requirement                                     | Pandion  | Section      |
|---|---|--|--------------|
| <b>RFP</b>  |   |  |              |
| Take-Off and Landing Distance over 50' Obstacle       | $\leq 1600'$                                    | 1500' takeoff,<br>1145' landing                          | §13.2, §13.7 |
| Climb Rate Sea Level                                  | $\geq 500 \text{ fpm}$                          | $625 \text{ fpm}$  | §13.3        |
| Cruise Speed  | $80 \text{ kts.}$                               | $\leq 80 \text{ kts.}$                                   | §2.3         |
| Max Operating Speed                                   | $110 \text{ kts.}$                              | 180 kts. No de-rating<br>147 kts. Never extend limit     | §13.4        |
| Max Altitude Capability                               | 11,500'   | $>11,500'$   | §13.3        |
| Climb Rate Max Operational Altitude (Std. Day +15 °F) | $\geq 100 \text{ fpm}$                          | $\geq 100 \text{ fpm}$                                   | §13.3        |
| Max Endurance   | 1 hr. 45 mins.                                  | 2 hrs. 45 mins.  | §13.6        |
| Extended Endurance                                    | 3 hr. 30 mins.                                  | 6 hrs. 10 mins.  | §13.6        |
| Seating   | 2   | 2  | §5.2         |
| Cabin Height & Width                                  | Compatible with two 6'5" Adult Males            | Compatible with two 6'5" Adult Males with winter outfits | §5.2         |
| Cargo Volume  | $\geq 10 \text{ ft}^3$                          | 14 ft <sup>3</sup>                                       | §5.4         |
| Useful Load   | $\geq 400 \text{ lb.}$                          | 400 lb.  | §12          |
| Battery Technology                                    | Technology EIS 2016                             | Lithium Air (available in the timeframe of 2016)         | §2.2, §9.1   |
| Battery Replacement                                   | 500 cycles                                      | 500 cycles   | §9.1, §14.3  |
| Charging Time   | $\leq 4 \text{ hrs. w/}$<br>220/240 volt source | 3.8 hrs.<br>220/240 volt source                          | §14.2        |
| <b>FAR §23 Adaptations</b>                            |   |  |              |
| §23.65 Rate of Climb                                  | $\geq 1.2 V_{S_1(\text{clean})}$                | Satisfied  | §13.3        |
| §23.65 Climb Gradient ISA                             | 8.3%  | 10%  | §13.3        |



## 1.0 Design Methodology

The general design philosophy of Pandion has been substantially influenced by methodology presented by *Jan Roskam*<sup>1</sup> and *Ed Heinemann*<sup>2</sup>. It should be noted that these methods are often quite extensive and cover technical aspects of the analysis in great detail. The majority of calculations performed and referenced within this proposal use published graphs and tables in order to determine the constants and parameters, often consisting of multiple time-consuming iterations. While the theoretical backgrounds of these methods are discussed in various parts of this proposal, many of the mathematical models and statistical data used in the design process are not presented in their entirety in the interest of brevity.

Design Structure Matrix (DSM), a modern method of development management, was used in order to determine the optimum design process. This method, described by *Eppinger et al.*<sup>3</sup>, is used to organize interrelated tasks in the design process in a way that minimizes feedback cycles and determines possible parallel analyses. The PSM 32 code, developed by Blitzkrieg Software, was utilized to implement the DSM in the routine process of developing Pandion. Utilizing this code, the entire design process was re-ordered based on the degree of dependency of each sub-process on the outputs of others. As a result, the design approach presented by *Roskam* has been slightly modified so as to allow for additional parallel processes, as dictated by specific needs of the Pandion concept, and consequently, improved development speed.

## 2.0 Preliminary Sizing

### 2.1 Preliminary Aerodynamic Analysis

Initial empirical drag polars were obtained using 2<sup>nd</sup> order regression methods presented by Roskam<sup>4,5</sup> as well as results from the preliminary weight analyses of Pandion. ESDU Performance Data Item 73018<sup>6</sup> was consulted to choose the critical parameters with the highest influence on maximum Specific Air Range (SAR). Three parameters were chosen to investigate the optimal lift coefficient for the aircraft when operating at cruise:  $C_L/C_D$ ,  $C_L^{0.5}/C_D$  and  $C_L/C_D^{3/2}$ . ESDU 73018 suggests  $C_L^{0.5}/C_D$  to be maximized, which corresponds to the maximum SAR at a fixed altitude, maintaining the same rate of energy consumption. Therefore, a battery powered airplane with a higher SAR would be able to fly further with the same battery pack\*. As it can be seen from Fig. 1, the SAR is maximized if the aircraft is operating at a lift coefficient of 0.65, which is significantly lower than the lift coefficient corresponding to maximum L/D (1.2). However, one could observe that the  $C_L/C_D$  curve in Fig. 1 is relatively flat around a lift coefficient of 0.5; therefore, the reduction in maximum air range as a result of optimizing the aircraft for maximum SAR is minimal.

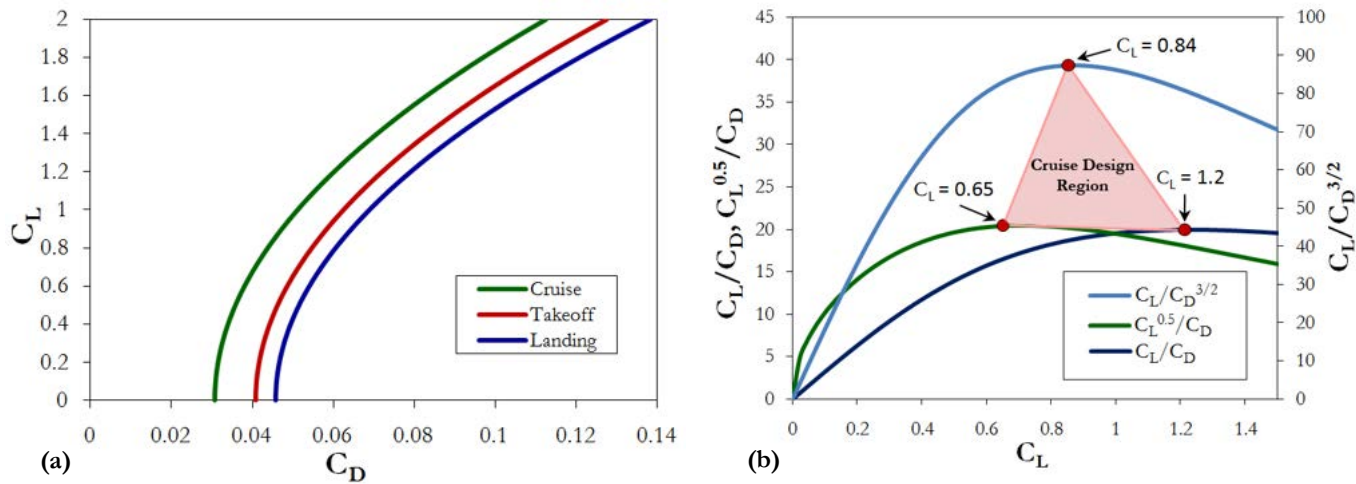


Fig. 1 Results of the preliminary aerodynamic projections. (a) Preliminary drag polars for different mission segments of the aircraft. (b) Parametric analysis of lift and drag data.  $C_L$  corresponding to maximum  $C_L/C_D$  maximizes the SAR at constant air speed.  $C_L$  corresponding to maximum  $C_L/C_D^{3/2}$  maximizes the SAR at constant thrust. Parameter  $C_L^{0.5}/C_D$  maximizes SAR at constant altitude and was selected based on the recommendations made by ESDU 73018 as a measure of merit, defining a design region of acceptable cruise  $C_L$ 's depending on the mission intended.

\* SAR, in a typical fuel-burning aircraft, represents essentially the sensitivity of the air range to the amount of fuel used. Comparably, as the fuel carried on board represents mostly the amount of work done to overcome aerodynamic drag, an electric airplane carries potential energy in a chemical form to be converted to electric power (i.e. the battery, which is a substantial portion of the takeoff weight).

## 2.2 Battery Technology Evaluation

In reviewing literature relevant to technology developed for high energy density battery packs, and in examining studies on the future of battery technologies for aerospace applications, it was determined that metal-air battery concepts will be a viable technology available in the timeframe of 2016. In particular, a paper published by *K. M. Abraham*<sup>7</sup> expressed very favorable opinions on the performance of metal-air batteries available for aerospace applications. Significant improvements in energy density are observed among next generation metal-air batteries that would make them a viable replacement for present state-of-the-art Lithium-Ion batteries. Performing a case study of performance and cost of various battery technologies, summarized in Table 2, it was observed that Lithium-Air batteries have the highest overall specific energy and energy density of all current and near future battery technologies. Although the specific costs of Lithium-Air batteries are projected to be substantially higher than Lithium-Ion batteries, it appears that this general difference is more than compensated by their improvements in specific energy and energy density. Such improvements make them ideal for applications in aerospace design, where space is limited and weight has significant effect on vehicle performance. Further investigation into the operation of Lithium-Air batteries<sup>8</sup> revealed that their generic operating temperatures are very high (122 °F to 158 °F) due to their exothermic internal chemistry. This potentially leads to a need for a compact cooling system to prevent the temperatures from exceeding their optimal range.

**Table 2 Summary of battery technology study. \* denotes cost values that have been extrapolated from battery technology cost trends.**

| Battery Type                     | Specific Energy<br>(Whr/kg) | Energy Density<br>(Whr/L) | Cost<br>(\$/kg) |
|----------------------------------|-----------------------------|---------------------------|-----------------|
| <i>Lithium-Ion:</i>              |                             |                           |                 |
| LiMn <sub>2</sub> O <sub>4</sub> | 100                         | 243                       | 15              |
| LiFePO <sub>4</sub>              | 108                         | 145                       | 12              |
| LG LiPo Gen 3                    | 95                          | 155                       | 11.84*          |
| LG Li-Ion                        | 200                         | 480                       | 31              |
| Tadiran XOL                      | 252                         | 645                       | 40.50*          |
| <i>Lithium-Air:</i>              |                             |                           |                 |
| Li-Air (PolyPlus)                | 700                         | 1000                      | 122.25*         |
| Li-Air (UDRI)                    | 1000                        | 1000                      | 177*            |

### 2.3 Mission Analysis

In order to determine the mass of the battery, it was necessary to compute the amount of energy required to perform the mission outlined by the RFP. Using the results of the preliminary aerodynamic analysis as well as basic physical principles, the work done by the major forces acting on the airplane (namely Drag, Lift, and Gravitational Forces) was computed considering the mission presented in Fig. 2 and summarized in Table 3.

**Table 3 Summary of Mission Energy Requirements**

| Flight Condition | Altitude (ft) | Speed (kts.) | Duration (min) | Preliminary $C_D$ | Energy (Wh) | Energy Fraction |
|------------------|---------------|--------------|----------------|-------------------|-------------|-----------------|
| 1. Takeoff       | 0             | 45           | 10             | 0.077             | 1,200       | 4 %             |
| 2. Climb         | 4,750         | 60           | 15             | 0.046             | 7,000       | 23 %            |
| 3. Cruise        | 9,500         | 80           | 60             | 0.037             | 15,000      | 50 %            |
| 4. Descent       | 6,000         | 60           | 7.7            | 0.048             | 1,300       | 4.33 %          |
| 5. Loiter        | 2,500         | 60           | 30             | 0.044             | 4,500       | 15 %            |
| 6. Descent       | 1,250         | 60           | 7.7            | 0.044             | 600         | 2 %             |
| 7. Landing       | 0             | 40           | 3              | 0.089             | 400         | 1.33 %          |

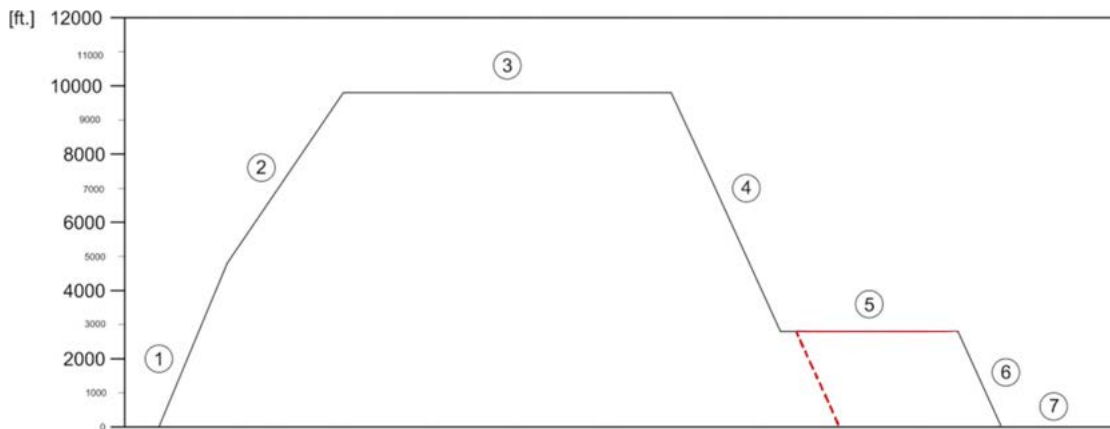


**Fig. 2 Mission Profile.** Note that the red solid line signifies the reserve mission, and the red hashed line signifies landing with the loiter segment in reserve.

From this analysis it was determined that the mission profile will involve a total of 30,000 Wh. of mechanical work done by the airplane. In order to account for losses due to propeller inefficiency, battery heat loses, and other energy loses in the circuit, an overall efficiency factor needed to be computed. Yuneec International states that the efficiency for an 80 hp DC brushless motor for aerospace applications is about 90%<sup>9</sup>. In personal correspondence with UACC, *Dr. Lutgard C. De Jonghe* claims that the efficiency for a high performance Lithium-Air battery pack is

approximately 70% at relatively high drain rates<sup>10</sup>. It was also assumed that a ground adjustable propeller with the efficiency of 85% can be designed to operate satisfactorily at all mission segments<sup>11</sup>. Another efficiency factor of 98% was assumed to account for power loses due to circuit inefficiencies, electric power extraction to run the cooling system, avionics, and lighting. Therefore the overall efficiency was computed from multiplying all the individual efficiencies yielding an efficiency factor of about 52%, accounting for all power extractions and thermal loses. This computation yielded the first order estimate of battery capacity to be 67  $kWhr$ . Inquires were made to the University of Dayton Research Institute (a leading institution in the field of metal-air battery technologies) with regard to the energy density of a generic Lithium-Air battery with an expected EIS of 2016. In response, *Dr. Binod Kumar*<sup>12</sup> cited an energy density of 1,000  $kWhr./kg.$ , resulting in an approximately 160  $lb.$  battery required.

#### 2.4 Preliminary Weight Analysis

Using the weight fractions obtained from *Roskam*<sup>8</sup>, initial estimations for the empty weight of the aircraft were performed. This analysis was done using regression coefficients presented by *Roskam* that are derived using available weight data for similarly sized airplanes. Table 4 presents the results of this analysis. Note that these results only reflect the statistical trends in light sport aircraft design and are later refined in two phases using higher order methods of estimating weight, to be presented in Ch. 11. Despite the electric propulsion system, the weight estimation method that is used for traditional aircraft was assumed to yield similar powerplant weights for either electric or fuel-powered system architectures. This assumption was later verified to be sufficiently accurate for the purpose of preliminary design, as will be presented in Ch 11.

**Table 4. Summary of initial weight analysis**

| Component            | $F_{MTOW}$ | Weight ( $lb.$ ) |
|----------------------|------------|------------------|
| Fuselage             | 0.16       | 190              |
| Wing                 | 0.15       | 180              |
| Empennage            | 0.03       | 30               |
| Landing Gear         | 0.07       | 85               |
| Engine Cowling       | 0.01       | 15               |
| Structure            | 0.42       | 500              |
| Powerplant           | 0.05       | 60               |
| Battery              | 0.13       | 160              |
| Fixed Equipment      | 0.07       | 80               |
| <i>Empty Weight</i>  | 0.67       | 800              |
| Passengers & Payload | 0.33       | 400              |
| MTOW                 | 1.0        | 1200             |

## 2.5 Performance Sizing Chart

The initial performance sizing of the aircraft was completed based on the performance requirements presented by the RFP, summarized in Table 1, and methods presented by *Roskam*<sup>13</sup>. The wing loading and weight-to-power ratios were obtained by solving performance boundary equations. Based on ESDU Aerodynamics 95021<sup>14</sup>, it was assumed in this analysis that a maximum lift coefficient up to 2.0 is achievable by using stand-alone single slotted Fowler flaps and no leading edge high lift devices. Weight figures obtained from preliminary weight estimates were used in conjunction with lift and drag characteristics obtained from preliminary aerodynamic analysis, which are presented in Sec. 2.1 and 2.4, respectively. A matching plot was constructed by overlaying the performance boundary graphs to identify the acceptable design space for wing loading and weight-to-power ratio for Pandion. The result of this analysis is presented in Fig. 3. With regard to climb performance, requirements set by FAR §23.77 were adopted as the RFP did not specify any climb performance for the aircraft. The design point was selected to minimize the required wing area and engine power while satisfying all performance requirements. A margin of error of 0.4 for  $C_{L\max}$  (25% from the target  $C_{L\max}$ ) and  $2 \text{ lb}/\text{ft}^2$  (20% from the wing area target) was considered to allow for containment of weight growth in further development. According to the performance sizing chart and mindful of the preliminary weight analysis presented in Sec. 2.4, a target wing area of  $136\text{ft}^2$  and engine power of  $80 \text{ hp}$ . was selected as the initial design point.

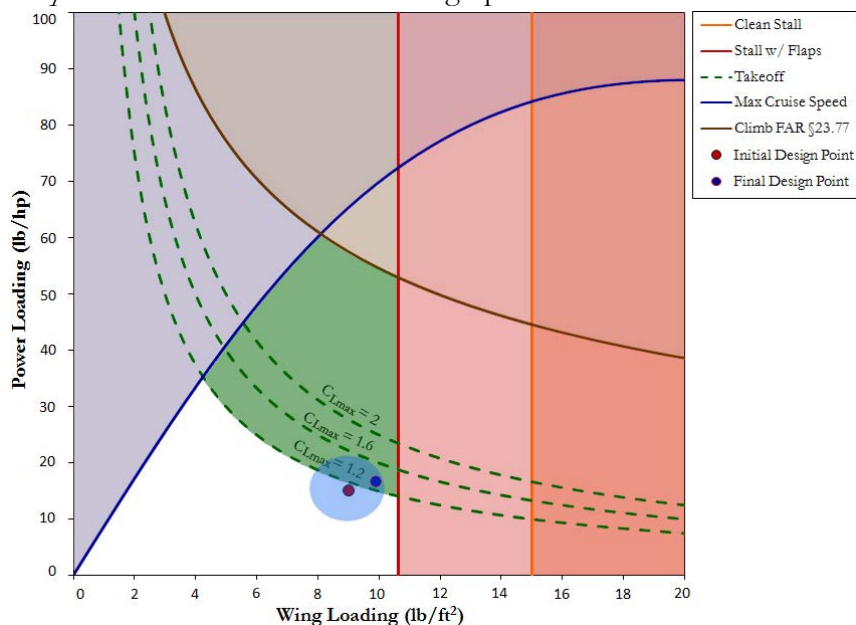


Fig. 3 Performance Sizing Chart. The blue circular region denotes a margin of development around the initial design point. In later design phases, a final design point was determined, lying within the margin.

### 3.0 Market Analysis

Starting with the release of the Light Sport Aircraft rules in 2005, the market has seen a steady rise in the popularity of this class of airplane. According to FAA estimates, at the end of 2009, there were 6,547 active LSAs. The FAA predicts this number to continue to increase at the rate of 450 per year until 2013 when it should start to abate and continue rising thereafter at a rate of 300 per year.<sup>15</sup> Outside of the US, there is also a strong market for this type of airplane. The European Microlight Federation is looking to expand the microlight rules into an LSA category the same way that LSA in the US was born of the ultralight movement. This is expected to be adopted at standards very close to the US standards as that over 65% of the US sold S-LSAs are manufactured in Europe.<sup>2</sup> Further, an all-electric LSA would have additional value in Europe where the primary distracter from personal aviation is the cost (attributed to both fuel and fees.) Based on this, we recommend an initial release into the US market with the future direction of expanding to Europe and Asia Pacific.

Reviewing comparable designs currently in operation, it was observed that a heavy emphasis is placed on cockpit visibility. Additionally, manufacturers actively market such a feature to be used for the purposes of sight-seeing and leisure flights. Extrapolating from this trend, UACC decided to provide astute visibility and ergonomics for the cockpit to improve sales.

Typically, LSAs utilize high performance internal combustion engines and low blade number propellers installed forward of the cockpit. Such a configuration, combined with the tendency to minimize weight by reducing the amount of acoustic insulation, leads to aggravated noise levels in the cockpit, reducing the overall passenger comfort. In response, it was decided that a configuration that inherently minimizes cockpit and community noise levels would be preferable if no major sacrifice has to be made in airplane performance.

A general survey of presently operational airplanes was performed by reviewing the data collected and published by the General Aviation Manufacturers Association<sup>16</sup> (GAMA) and the Light Aircraft Manufacturers Association<sup>17</sup> (LAMA). The statistics gathered by GAMA were

analyzed to identify market and technology trends in general aviation airplanes that may apply to S-LSAs.

As it can be observed from Fig. 4, about 95% of the top selling general aviation airplanes and 80% of top selling LSAs shipped within the past 12 years were designed with a side-by-side seating arrangement. It is noteworthy that the increase in the market share of tandem cockpit LSAs is highly influenced by the replicas of the legendary Piper J-3 Cub. As the general customer group of S-LSA airplanes is dominated by personal flyers and flight schools<sup>18</sup>, it was decided to utilize a side-by-side cockpit arrangement for the development of Pandion in order to maximize its marketability. This seating arrangement facilitates face-to-face communication, desirable during personal and instructional flights.

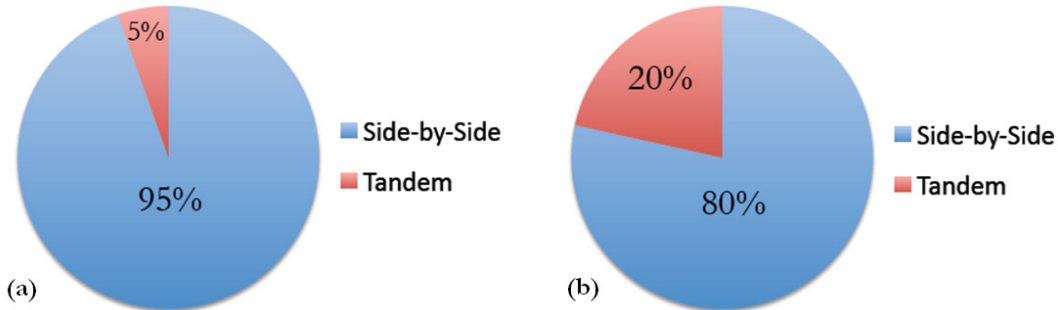


**Fig. 4 Seating Arrangement Categories among top selling airplanes from 1999-2011: a) FAR 23 GA airplanes and b) light airplanes**

As suggested by Roskam<sup>19</sup>, aesthetics and ramp appeal of light airplanes can heavily improve their commercial success. Therefore it was decided that the design, considering continuous improvements in manufacturing methods and cost effectiveness of composites, will feature complex geometries to improve its aesthetics, as well as performance. It was also decided that, to be a commercially successful project, Pandion has to employ a significantly different design style, distinguishing it from its competitors as an independent and original design.

Reviewing the recent market environment for similar items, it was observed that goods that incorporate innovative technologies achieve better sales as buyers typically appreciate and choose creative designs. Therefore, it was decided that Pandion must incorporate innovative features that focus on enhancing safety, performance, and airport compatibility.

## 4.0 Configuration Trade-offs

### 4.1 Sensitivity Analysis

A basic sensitivity analysis was performed in order to obtain a more detailed understanding of the relationship between the performance figures and the planform geometry, mainly the aspect ratio. As the range is the factor limiting the practicality of an electric airplane, the effects of aspect ratio and range received particular attention. To compute the effects of the change of aspect ratio on the air range of the airplane, Eq. 1 was used,

$$\left(\frac{\partial R}{\partial AR}\right)_{Cruise} = \left(\frac{\partial C_D}{\partial AR}\right)_{Cruise} \cdot \left(\frac{\partial R}{\partial C_D}\right)_{Cruise} \quad (1)$$

Partials  $\partial C_D / \partial AR$  and  $\partial R / \partial C_D$  were computed numerically by changing the aspect ratio and obtaining the respective steady state drag coefficient and range during cruise and loiter within the environment of the *Advanced Aircraft Analysis* tool as well as an in-house developed performance tool. Cruise and loiter were selected due to their long durations and their large impact on sizing the battery for the aircraft. The sensitivity of range to aspect ratio was plotted versus aspect ratio and can be seen in Fig. 5. It is noteworthy that the range performance is optimized where the  $\partial R / \partial AR$  derivative is very small but positive. It can also be observed that the  $\partial R / \partial AR$  derivative during loiter does not change significantly and therefore was found to not be a design parameter for wing geometry. Reviewing the results of this analysis, it was decided that a relatively high aspect ratio wing ( $\sim 18\text{-}19$ ) will be needed to optimize the range performance of the airplane at cruise. Relatively higher aspect ratios ( $\sim 20\text{-}25$ ) are routinely seen in sailplane configurations with comparable maximum speeds and, given the increased stiffness of modern composite wing structures, such very high aspect ratios may be used with no adverse effect.

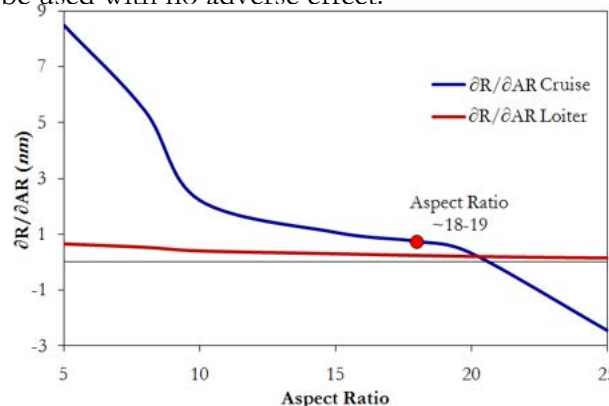


**Fig. 5 Results of the sensitivity of range to AR at various ARs, at cruise and loiter.  
Note that each data point is a fully sized airplane.**

## 4.2 Configuration Selection

Once the seat arrangement and the aspect ratio were selected for Pandion, it was possible to explore the different possible configurations by evaluating the available options for main component configurations, as summarized in Table 5. The components for which available configurations were explored were wings, empennage, motor installation, and propeller placement.

For the wings, three possible vertical locations were evaluated: low wing, mid wing, and high wing. Mid-wing aircraft have better takeoff characteristics<sup>20</sup> and are lighter than high-wing aircraft. It also aids passengers in entering the cockpit, eliminating the requirement for a separate ladder. Mid-wings are aesthetically more pleasant than low-wings, which makes them more desirable. Given these desirable characteristics of mid wing over both high and low wings, this configuration was selected for Pandion.

For the empennage, three possible configurations were also evaluated: conventional layout, in which the horizontal stabilizer is attached to the fuselage; cruciform, in which the horizontal stabilizer is attached to the vertical stabilizer; and V-tail, in which vertical and horizontal stabilizers are combined into diagonal surfaces that perform the functions of both. Given the lower weight, structural simplicity, and lower stick forces required, a conventional empennage layout was selected for Pandion.

An analogous process was followed for landing gear layout and engine mounting. A tricycle landing gear was selected given its superior ground handling characteristics. A mid-engine configuration was selected for its improved balance characteristics, due to its proximity to region of desirable CG location. Finally, and after having selected the location of the engine and the overall configuration layout of the airplane, a rear-mounted propeller system was selected given promising improvements to aerodynamic performance, visibility, and noise.

After this synthesis was completed, the configuration of Pandion was developed into much higher level of detail to allow for higher order analyses to be performed. A description of the final configuration is presented in Sec. 5 of this document.

Table 5. Configuration Selection

| Wing Location   |  |            |              |  |  |
|-----------------|--|------------|--------------|--|--|
| Options         | High   | Mid        | Low          |  |  |
| Justification   | Mid-wing aircraft have better takeoff characteristics and are lighter than high-wing aircraft. It also aids passengers in entering the cockpit, eliminating the requirement for a separate ladder. Mid-wings are aesthetically more pleasant than low-wings, which makes them more desirable.                                      |            |              |  |  |
| Empennage       |  |            |              |  |  |
| Options         | Conventional   | Cruciform  | V-Tail       |  |  |
| Justification   | Conventional empennages require lower stick forces relative to V-tails, and are lighter than cruciform empennages.   |            |              |  |  |
| Landing Gear    |  |            |              |  |  |
| Options         | Tricycle   | Tail Wheel |              |  |  |
| Justification   | Aircraft with tricycle landing gear have better ground handling characteristics than aircraft with tail wheel landing gear. Takeoff visibility is also improved relative to a tail wheel configuration. Finally, tricycle landing gear aircraft are more desirable for instructional use due to their improved view of the runway. |            |              |  |  |
| Engine Location |  |            |              |  |  |
| Options         | Front  | Mid        | Rear         |  |  |
| Justification   | Locating the engine in the middle section of the fuselage makes it easier to provide cooling air for the engine than mounting it in the rear. It is also preferred for balance considerations over rear and front mounted engines, as it will have a lower effect on the location of the CG of the aircraft.                       |            |              |  |  |
| Prop Placement  |  |            |              |  |  |
| Options         | Front  | Rear       | Wing-Mounted |  |  |
| Justification   | Placing the propeller in the rear of the fuselage improves the performance by reducing drag. This is caused by wake-filling effects generated by the propeller operation in this location. Twin wing mounted propellers with a single engine would require complicated gearing systems, increasing complexity and weight.          |            |              |  |  |

## 5.0 Configuration Description

This section describes the final configuration of Pandion. This serves as a point of reference regarding the geometries and features discussed in later sections of this document that deal with engineering analysis and design of specific aspects of Pandion.

### 5.1 Fuselage Geometry

The fuselage features smooth polynomial cross-sections in the forward region and elliptical sections in the aft region. The side and top profiles are designed in a way that the mean surface curvature is always positive while preserving smooth curvature changes to minimize profile drag and delay the transition of the surface flow to turbulence. Efforts have been spent to maintain a constant mean curvature on the regions occupied by transparencies to reduce optical distortion. Figure 6 presents the values of mean curvature plotted on the fuselage surface. Sample cross-sections longitudinal profiles are presented in the three-view foldout and the inboard profile foldout at the end of this chapter.

The fuselage structure is of semi-monocoque construction assembled from mostly Carbon Fiber Reinforced Plastic (CFRP) parts to save weight and increase stiffness. Figure 7 presents a view of the structural arrangement of the fuselage.

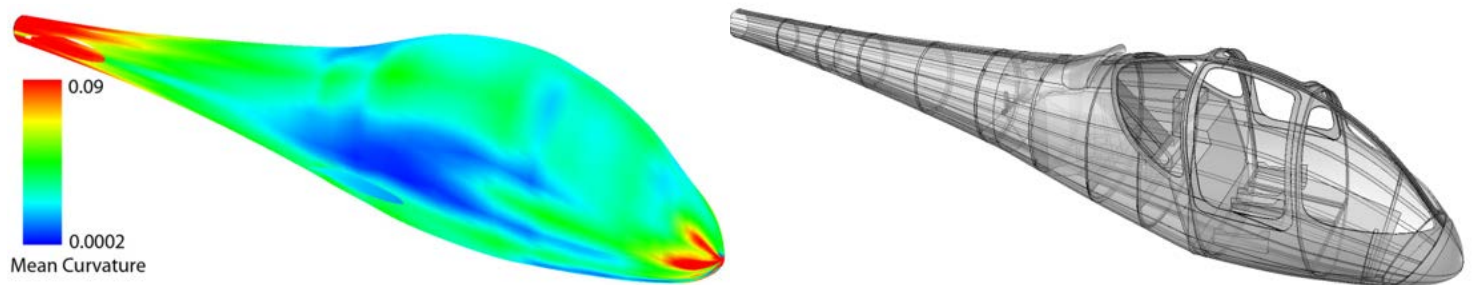


Fig. 6 Mean Curvature Distribution on the fuselage surface

Fig. 7 Structural Arrangement of fuselage

### 5.2 Cockpit & Ergonomics

As previously mentioned in the market analysis section, particular emphasis was placed on the comfort level of the occupants inside the cockpit. The cockpit was designed to accommodate two 6'2" tall male occupants with comfort, while providing astute visibility and access to flight

controls. The design provides  $25^\circ$  over-the-nose visibility while providing unobstructed visibility to the sides suitable for sightseeing flights.

Figure 8 presents the final visibility pattern of the cockpit. The adjustable seats were designed to provide good lumbar and lateral support as well as crash survivability. The control column was designed to allow for  $+9^\circ$  and  $-17^\circ$  deflection in the pitch direction, and  $\pm 8^\circ$  in the roll direction. Cockpit pedals were designed to allow for maximum rudder surface deflections by  $\pm 2''$  of pedal movement, as can be seen in Fig. 9.

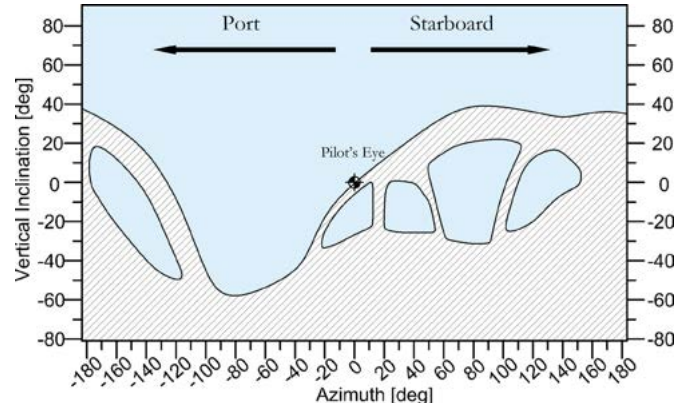


**Fig. 8 Visibility Pattern from pilot seat**

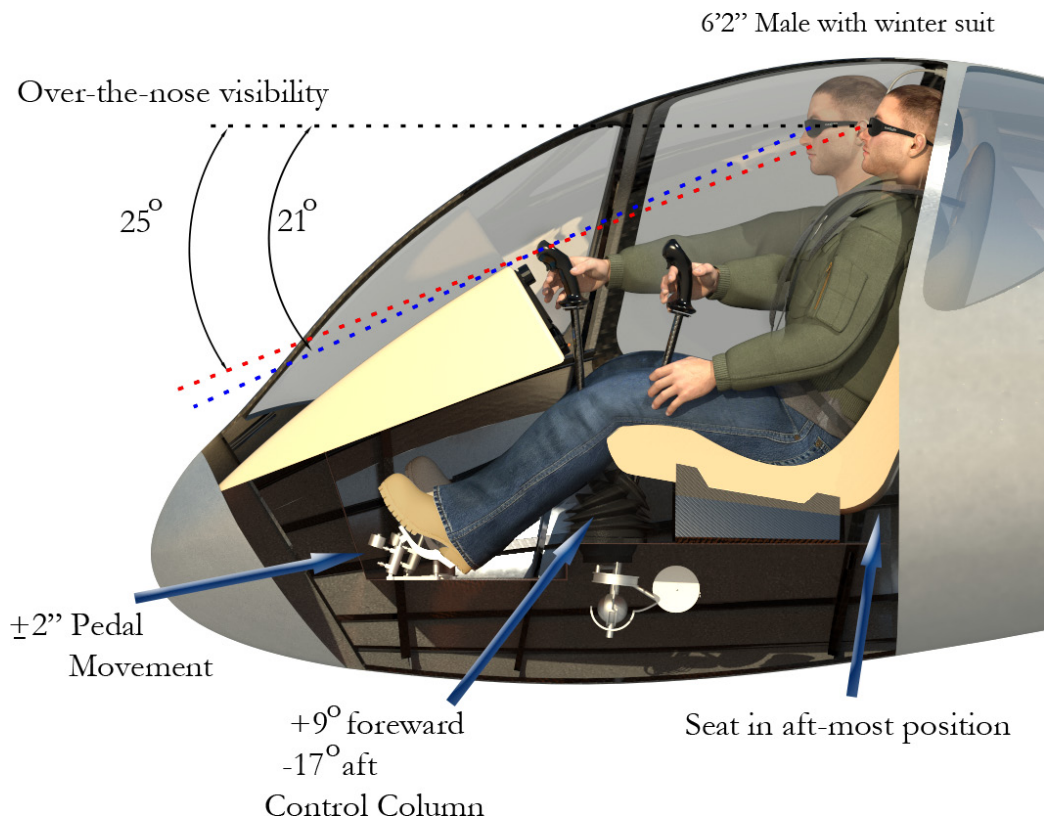


**Fig. 9 Cockpit Cutaway Highlights**

### 5.3 Cockpit Access

The cockpit of Pandion is accessible via two gull-wing doors from the side. A full glass canopy was originally implemented, but after more synthesis, it was decided that the gull-wing arrangement will have a lighter weight and can be designed with a small impact on cockpit visibility, while providing more crash reinforcement to the forward fuselage structure. The doors have a slight curvature to keep them closed and in position using the air flow, should the doors become accidentally opened during flight. Figure 10 presents the location of the gull-wing cockpit doors.



**Fig. 10 Gull-wing cockpit doors**

### 5.4 Cargo Stowage

14 ft.<sup>3</sup> of useful volume for cargo stowage is provided, which exceeds the 10 ft.<sup>3</sup> requirement by the RFP. The internal arrangement of the components in mid-fuselage is designed in way to allow oversized popular cargo items for small aircraft (such as a bag of golf clubs, hunting or camping gear). Figure 11 and 12 present a view of the cargo stowage and an inboard profile of the stowage, both displaying the capacity to carry oversized items.

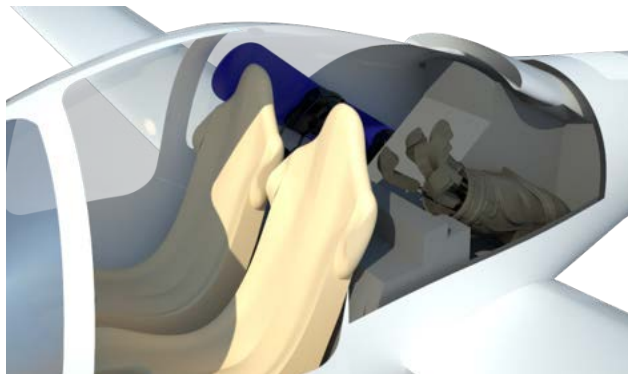


**Fig. 11 Cargo Stowage with a golf bag and a snowboard**

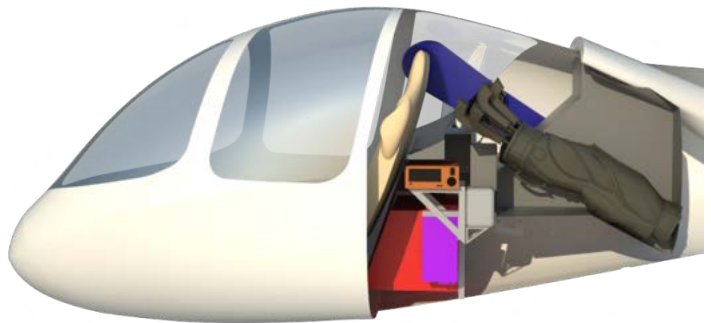


**Fig. 12 Cargo Stowage inboard profile with a golf bag and a snowboard**

## 5.5 Wing Planform, Winglets, and Folding Mechanism

The wing planform for Pandion has an equivalent area of  $136.3 \text{ ft}^2$  and a span of 50', resulting in an aspect ratio of 18.35. The quarter chord sweep of the wing is  $-1.4^\circ$  while the leading edge is unswept. The taper ratio of the wing is 0.38, selected to optimize the Oswald's Efficiency factor for the wing at cruise. Choices surrounding planform are driven by aerodynamic trade studies and optimizations that are highly influenced by the concept of NLF. The low sweep of the wing planform, combined with relatively low Reynolds numbers and custom designed NLF airfoils, allows for extensive laminar flow (approximately 60%) on upper and lower surfaces of the wing, drastically reducing the friction drag of the configuration at cruise conditions. Sections 6.2 and 6.7 of this proposal present the wing planform optimization and CFD verification for NLF characteristics, respectively. To further increase the efficiency of the wing planform, a 1.28' high winglet is canted from the vertical at  $6^\circ$ . The outboard 7' of the wing is capable of folding via an internal electric folding mechanism to allow taxiing in narrow taxiways and to maintain compatibility with standard T-Hangers, as required by the RFP. The wing is equipped with two sets of single slotted Fowler flaps on the trailing edge extending up to 45% of the wing halfspan. An aileron surface starts at 45% of the wing halfspan and ends at 73% of the wing halfspan, coinciding with the location of the folding line of the outboard wing. Figure 13 presents the wing planform for Pandion.

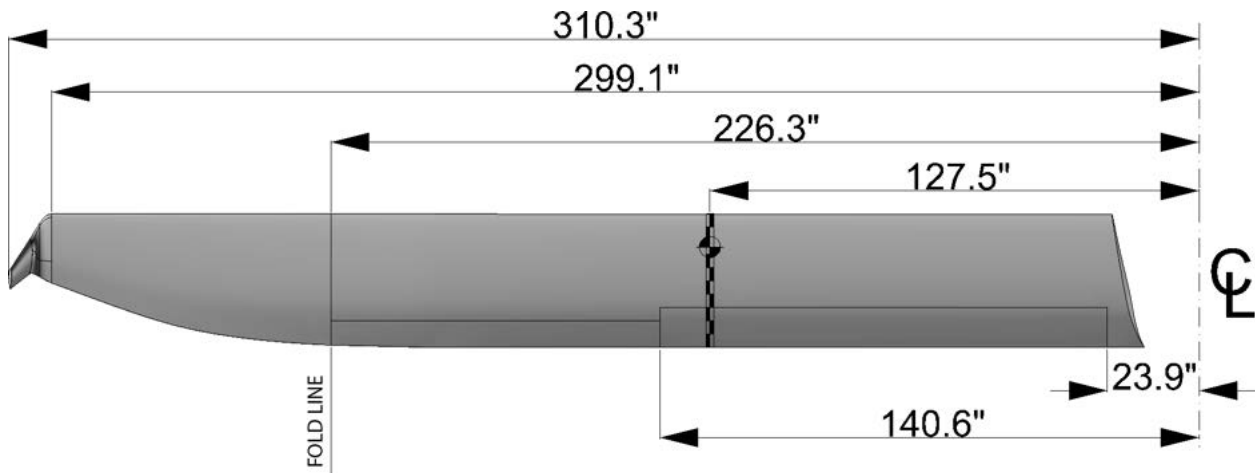


Fig. 13 Wing Planform

## 5.6 Empennage

The empennage of Pandion consists of a conventional configuration, offering lower weight and requiring lower stick forces than the considered alternatives. The horizontal tail has a planform area of  $42.2 \text{ ft}^2$  and a span of  $15.1'$ , resulting in an aspect ratio of 5.4. The quarter chord sweep of the horizontal tail is  $8.7^\circ$ . The vertical tail has an aspect ratio of 1.5 and features a lower ventral fin, with an area of  $3.4 \text{ ft}^2$ , designed to protect the propeller from expensive prop strikes in hard landings. The vertical tail surface is swept aft by  $38^\circ$ .

Both horizontal and vertical tail sweeps are cosmetic features designed to improve the aesthetic qualities of the airplane, which typically lead to better market performance<sup>21</sup>.

The horizontal tail is equipped with elevators on the trailing edge extending up to 90% of the tail span. The structures of the horizontal and vertical tails are conventional, two-spar, semi-monocoque, composite elements that are fixed on the upper and sides of the fuselage frames. Figure 14 details the empennage structure of Pandion.

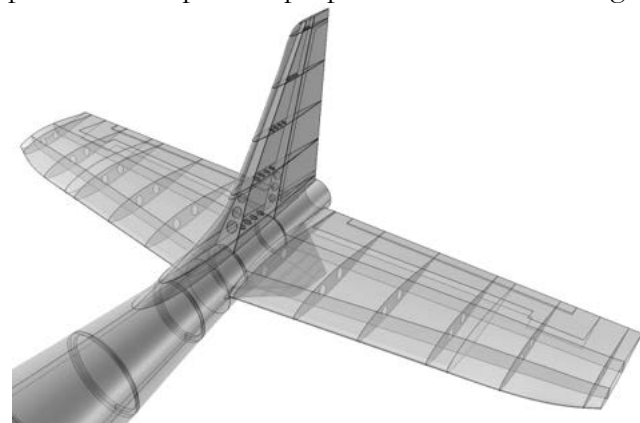


**Fig. 14 Empennage Arrangement**

## 5.7 Propeller

A ground-adjustable propeller was designed for its implementation in Pandion. Size and noise considerations were the main driving parameters for the design, given the relatively small space available and the goal of improving comfort by reducing noise. In order to obtain the required thrust and match aforementioned constraints, the propeller diameter and number of blades were maximized within the limits imposed by the location selected. Figure 15 presents the propeller of Pandion. The final design is an 8-blade, 55" diameter, high advance ratio propeller with composite blades and an aluminum hub. A propeller cone was designed

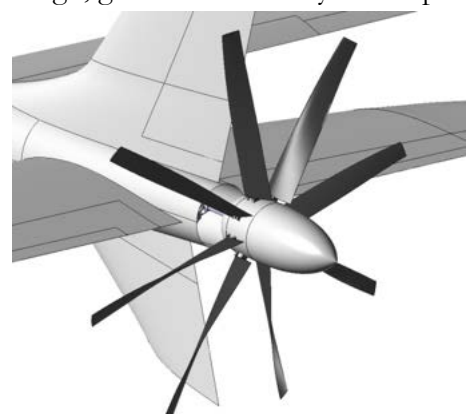


**Fig. 15 8-blade low-noise propeller**

to improve the aerodynamic performance of the airplane by faring the base of the fuselage geometry. A propeller tilting mechanism was designed to increase safety in flight by helping in deep stall recovery. This system tilts the propeller generating a vertical thrust component, which results in a nose down pitching moment. This feature will be further discussed in Section 12.7. The propeller design and performance will be described in detail in Section 8.2.

### 5.8 Electric Motor

Pandion is powered by a Yuneec PowerDrive60 DC brushless electric motor for aerospace applications. It is capable of producing a maximum of  $80 \text{ hp}$ . and  $240 \text{ N}\cdot\text{m}$  of torque at 2,400 RPM. It is designed to operate at a voltage of  $166 \text{ V}$  and current of  $340 \text{ A}$ . It is essentially an air-cooled electric motor, which dissipates  $3,000 \text{ W}$  of heat yielding an overall mechanical efficiency of 90%. It requires an airflow rate of  $1.2 \text{ kg/sec}$ . rate at cruise to maintain its optimal operating temperature, which is provided by a dedicated S-duct located on the upper side of the fuselage. The electric motor weight is  $66 \text{ lb}$ . and requires a power management unit to regulate its voltage and current at different RPMs. The power control unit is installed in the dorsal electronics bay and occupies  $170 \text{ in.}^3$  of volume. The electric motor is installed via a simple truss in the mid fuselage section and can be accessed from a dedicated access panel from below. Figure 16 presents the electric motor as installed inside the fuselage. The power from the motor is transmitted to the propellers through a  $100''$  long,  $7/8''$  diameter drive shaft made of SAE 4131 steel. Figure 17 presents the drive shaft installation path through the aft fuselage.

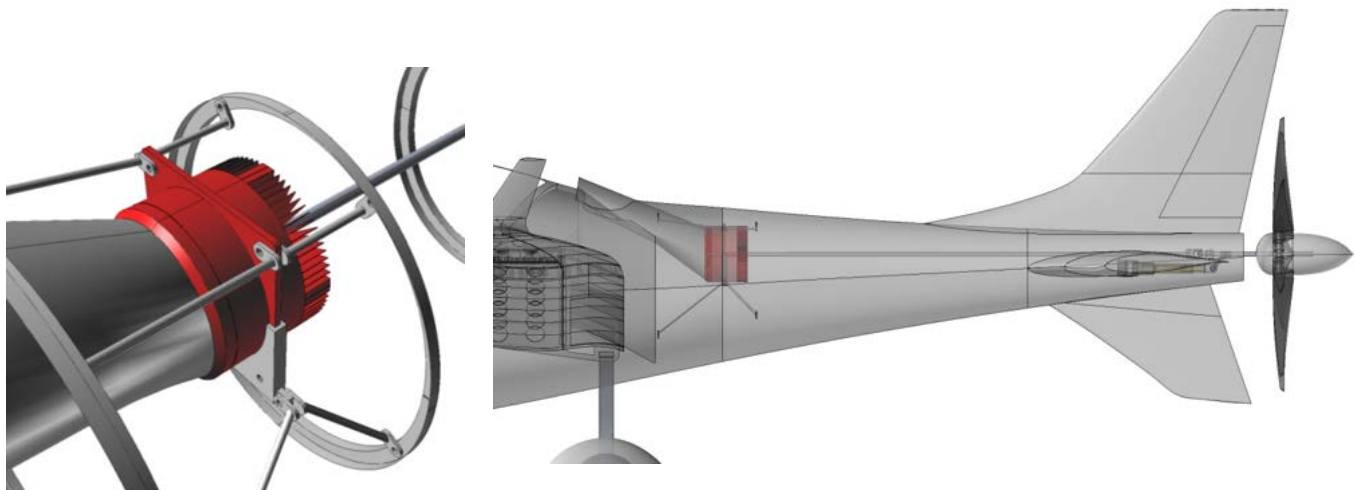


Fig. 16 Electric Motor Integration attached to fuselage frames

Fig. 17 Propeller-Drive Shaft integration

## 5.9 Landing Gear

Pandion utilizes a tri-cycle landing gear equipped with 5.00-5" main tires and a 5.00-4" nose tire. A tri-cycle configuration was selected over a tail wheel configuration given its better ground handling characteristics as well as improved takeoff visibility. The main and nose tires can withstand maximum operating loads of 800 *lb.* and 700 *lb.*, respectively<sup>22</sup>. The nose landing gear is equipped with a steering mechanism directly linked to rudder pedals. Both of the main landing gears are equipped with a closed circuit hydraulic brake system, each individually controlled by brake cylinders coupled with the rudder pedals. A detailed description of the steering and braking systems is given in Sec. 10.4.

The suspension for the main landing gear is provided via a set of leaf springs made of 4130 low-carbon steel designed to absorb landing impact energy resulting from a sink rate of up to 10 *ft./sec.* The leaf spring is attached to the main structure via a carbon-fiber composite bracket that is mounted to two dorsal frames in the fuselage. Nose and main landing gears are equipped with fairings for the purpose of reducing drag as well as controlling their tire spray, which is discussed in detail in Sec. 10.1. Figures 18 and 19 present the landing gear arrangement and a detail of the nose wheel turning, respectively.



Fig. 18 Landing gear arrangement

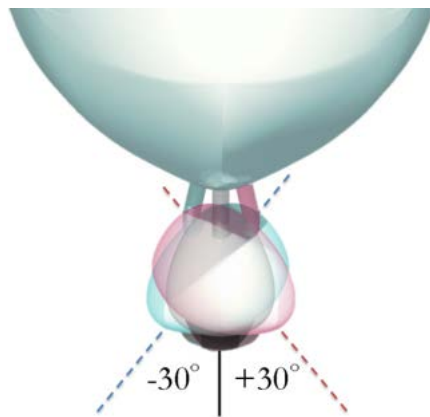
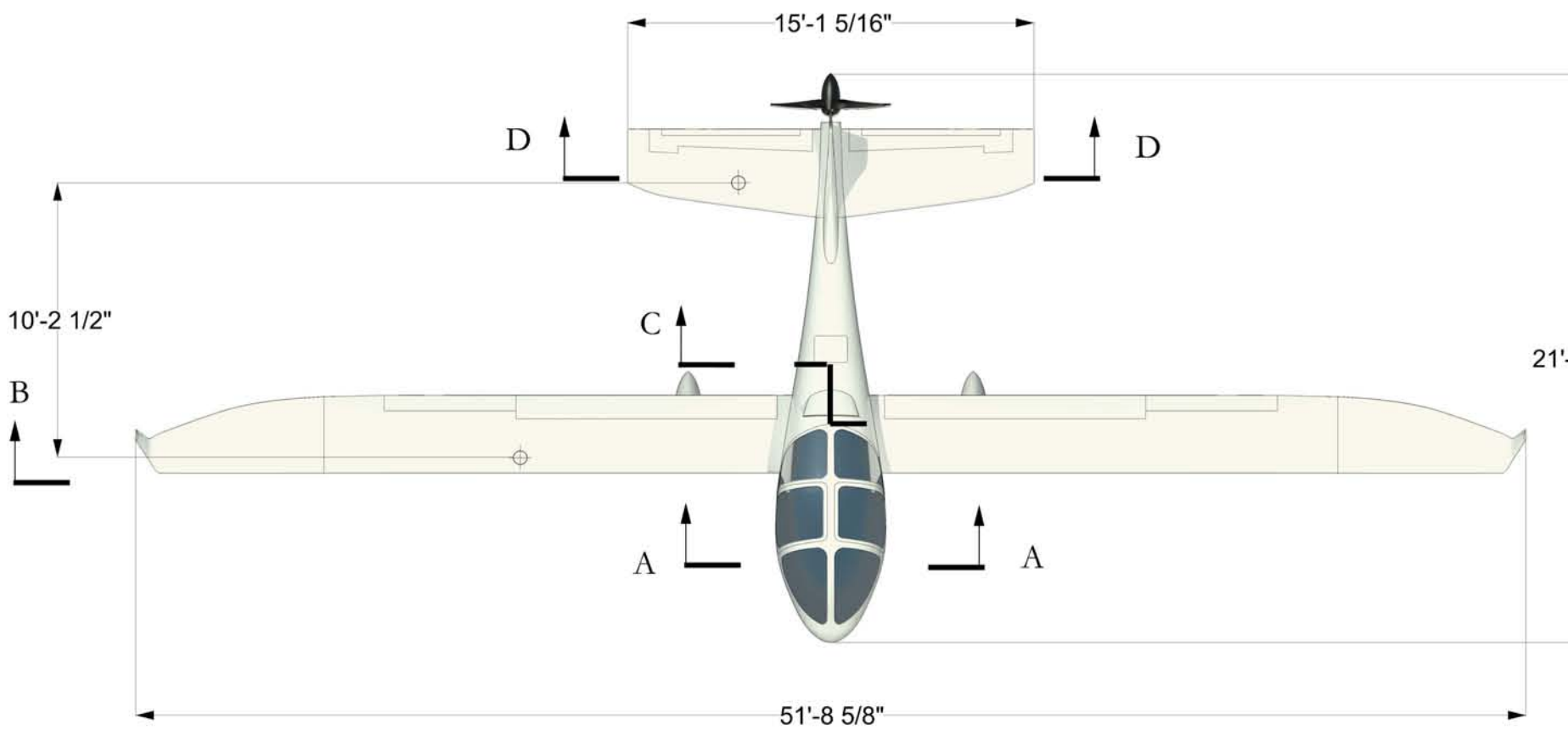


Fig. 19 Detail of nose wheel turning

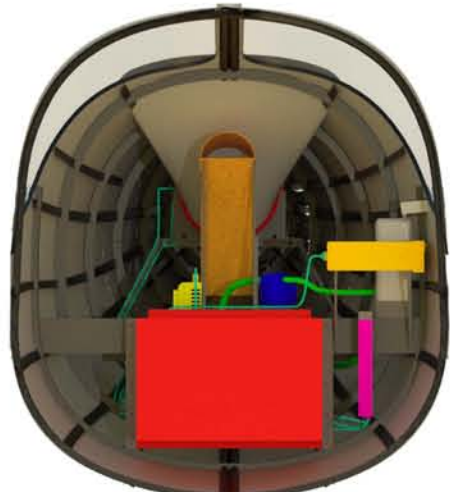


# Pandion

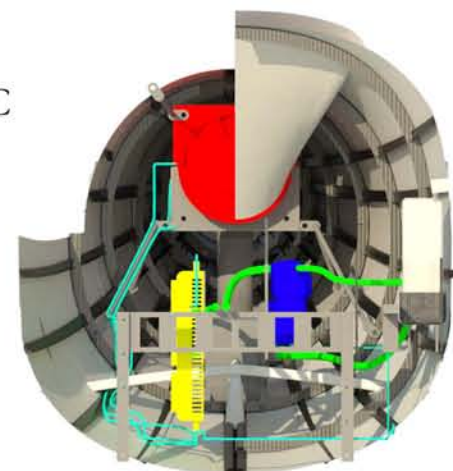
Three view and cross-sections.



A-A



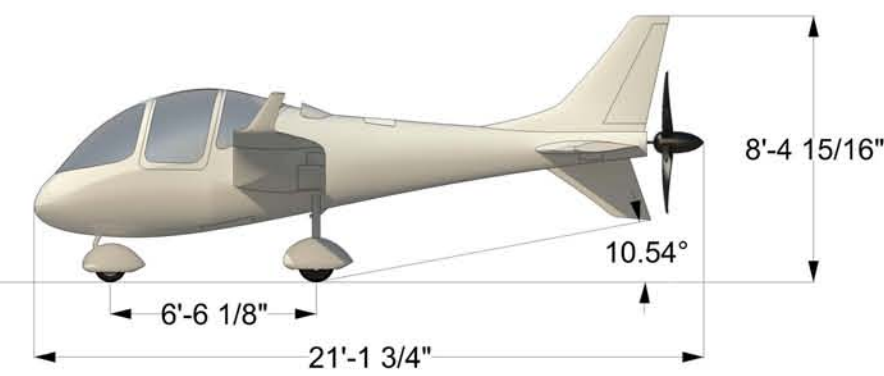
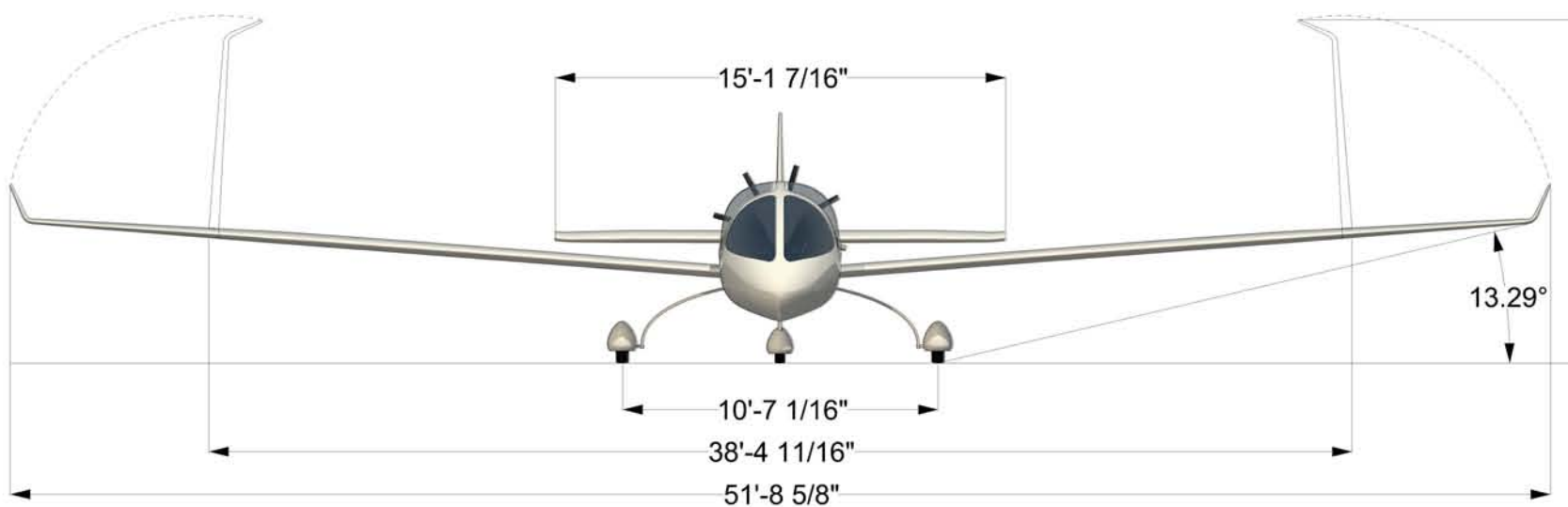
B-B

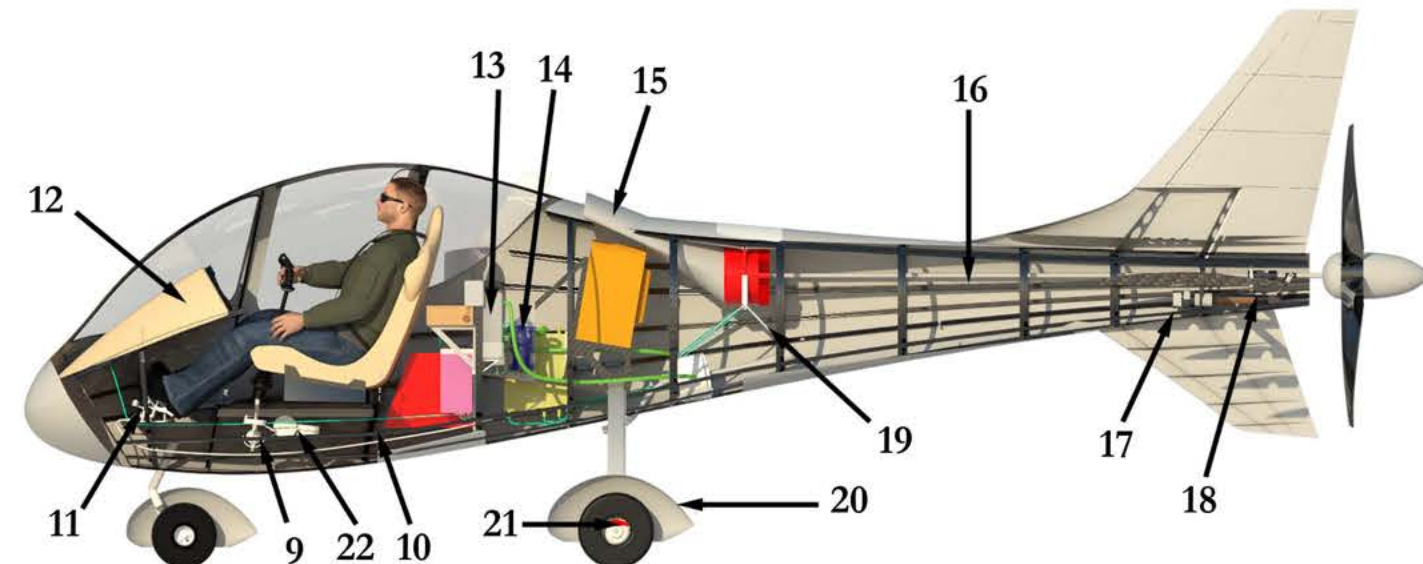
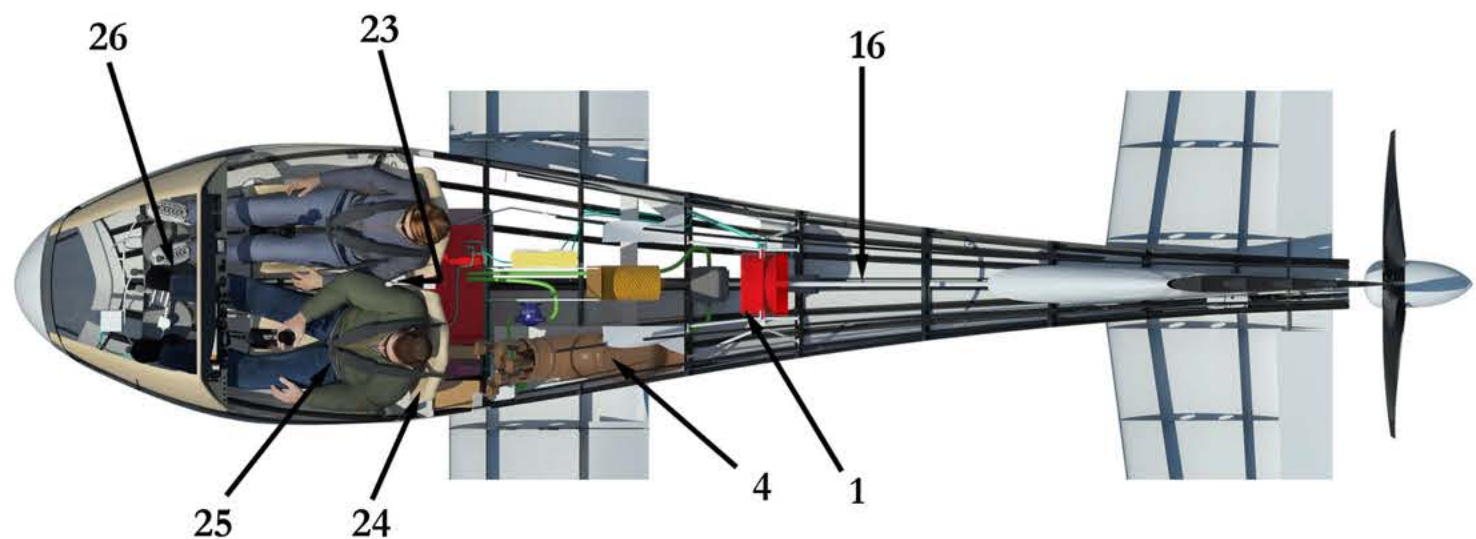


C-C



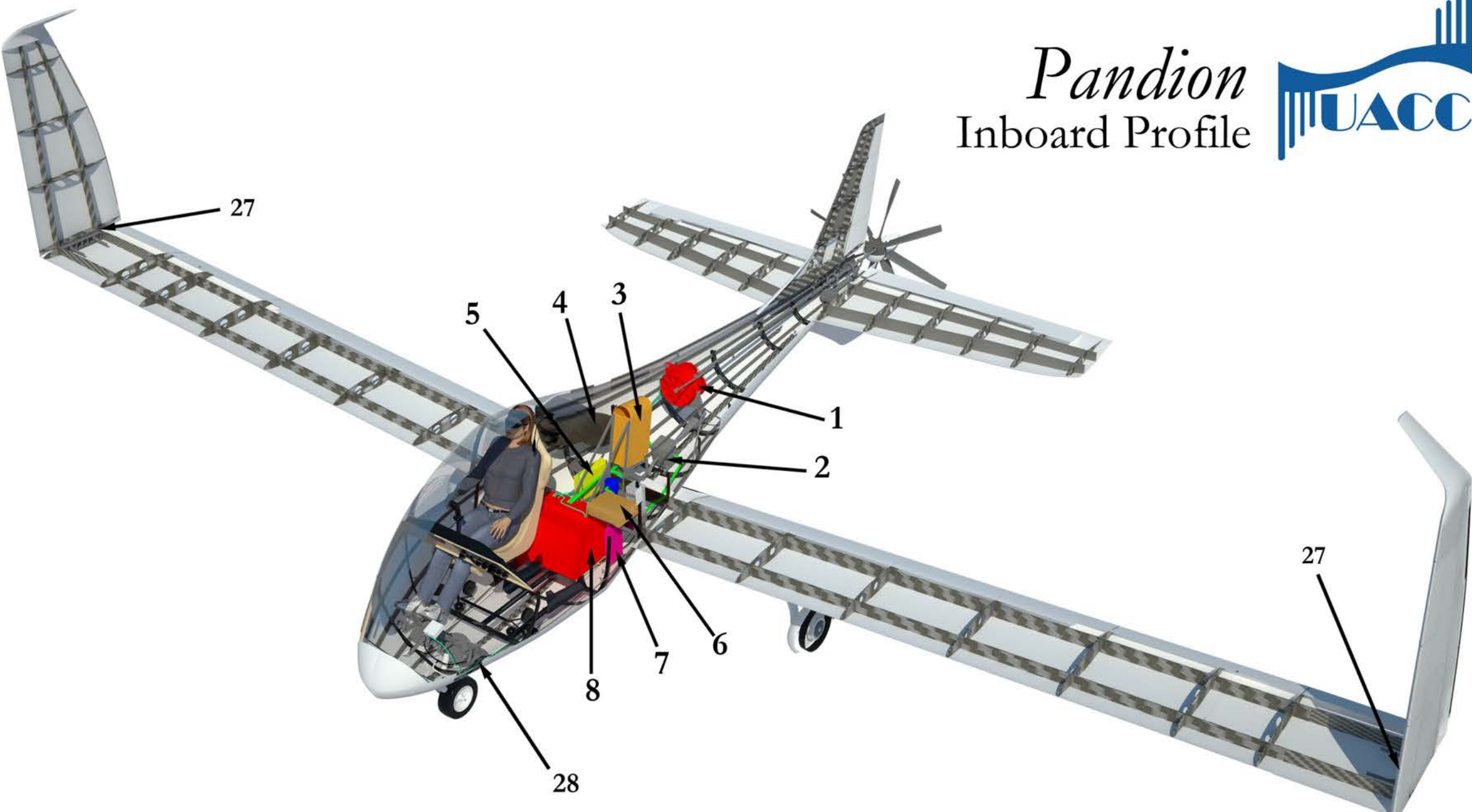
D-D





1. 80 hp Electric Motor
  2. Battery Heat Exchanger
  3. Recovery Parachute Pack
  4. Golf Club Bag
  5. Motor Controller Unit
  6. Battery Charger Unit
  7. DC-DC Converter
  8. Li-Air Battery
  9. Control System
  10. Brake Line
  11. Rudder Pedal
  12. Dashboard
  13. Coolant Reservoir
  14. Coolant Pump
  15. Air Inlet
  16. Propeller Shaft
  17. Propeller Tilting Actuator
  18. Propeller Tilting Mechanism
  19. Motor Mount
  20. Landing Gear Fairing
  21. Brake Calipers
  22. Control Cable Pulley
  23. Flood Light
  24. G-Seat
  25. Four Point Safety Belt
  26. Instrument Panel
  27. Wing Folding Mechanism
  28. Steering Mechanism

# *Pandion* Inboard Profile



## 6.0 Aerodynamics

### 6.1 Airfoil Design

The method for selection of airfoil profiles was dictated by two main criteria. First, in order to maximize the extent of natural laminar flow on the upper surface (thus reducing friction drag), the selected airfoils needed a favorable “rooftop” shape pressure coefficient distribution<sup>23</sup>. Second, the airfoil geometry must have moderate pitching moment coefficients to avoid larger horizontal tail planform areas required to balance the aircraft. In order to obtain a reasonable baseline airfoil, a study of 15 low Reynolds number, natural laminar flow airfoil geometries (available on University of Illinois at Urbana-Champaign’s<sup>24</sup> web portal) was conducted. The airfoils were analyzed using the *DesignFoil* software on the merit of the maximum extent of laminar flow at  $C_L$  0.65 (selected in Sec. 2.1). Figure 20 presents a summary of the airfoil selection.

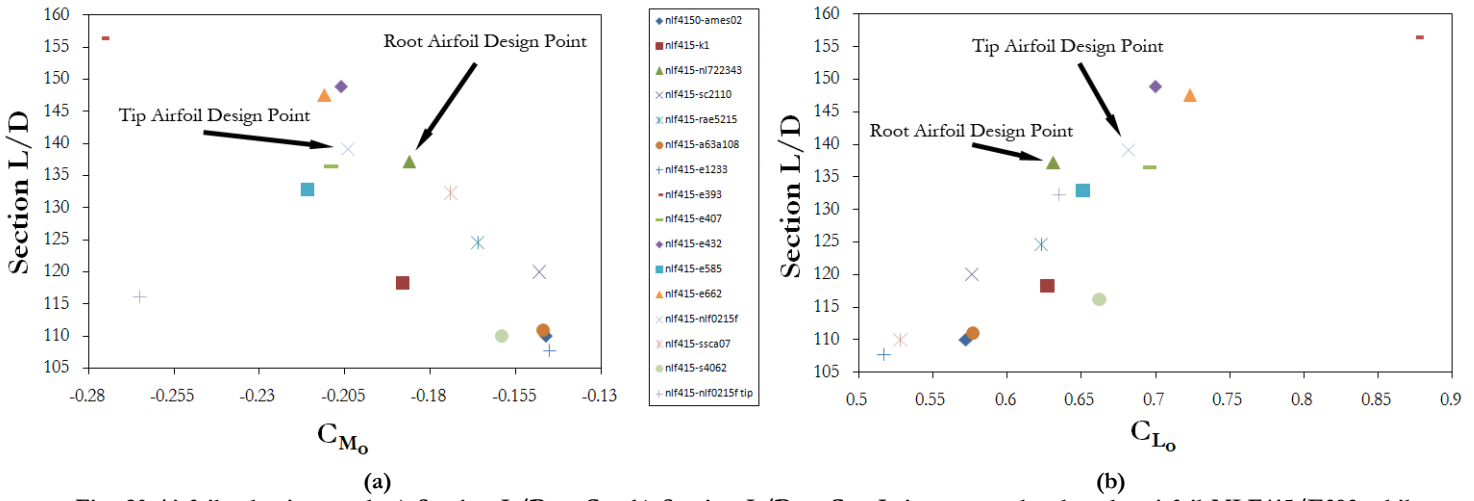


Fig. 20 Airfoil selection pool. a) Section L/D v.  $C_{M_0}$  b) Section L/D v.  $C_{L_0}$ . It is noteworthy that the airfoil NLF415/E393 while having outstanding L/D and  $C_{L_0}$  performance, attains too large of a moment coefficient, making it unsuitable as a wing airfoil.

Using these airfoils, multiple combinations of upper and lower surface curves were analyzed in order to select the best performing combination. NASA Langley’s NLF-415 was selected as the upper airfoil profile for both root and tip. The NL722343 was selected for the lower root airfoil profile and NLF 0215F was chosen for the lower tip airfoil profile. Camber adjustment was performed on the root and tip airfoils to increase their section cruise L/D. As the extent of laminar flow plays a significant role in airfoil performance, CFD analyses (using *ANSYS CFX*) were then performed to verify the locations of transition to turbulence as well as general airfoil characteristics.

Figures 21 and 22 present a summary of the results of the CFD analyses performed on the root and tip airfoils.

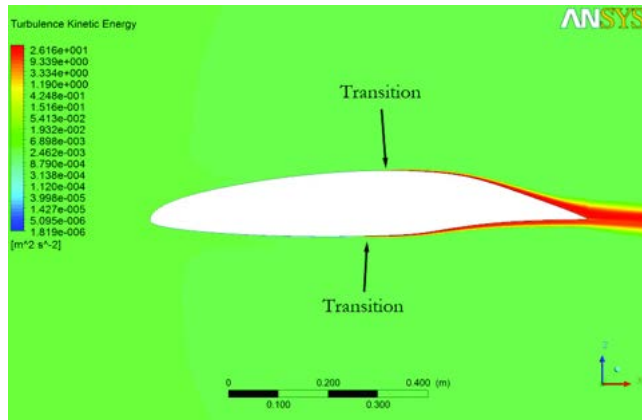


Fig. 21a Root airfoil turbulent kinetic energy

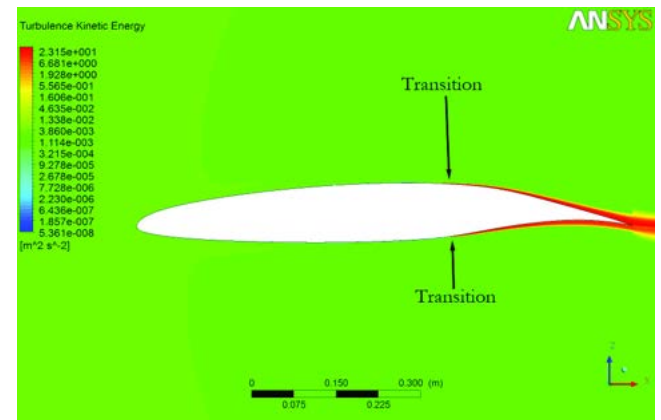


Fig. 22a Tip airfoil turbulent kinetic energy

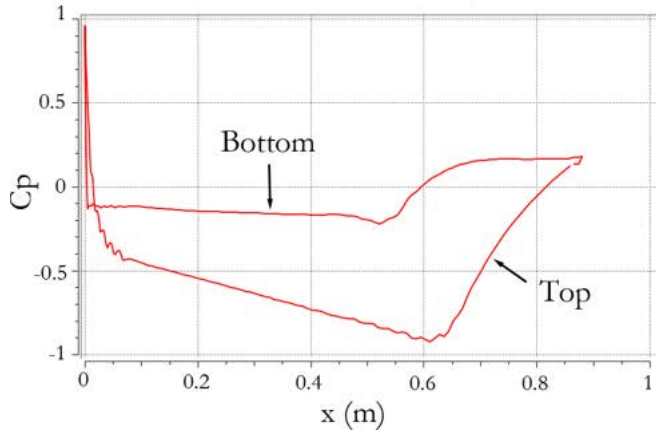


Fig. 21b Root airfoil pressure coefficient plot

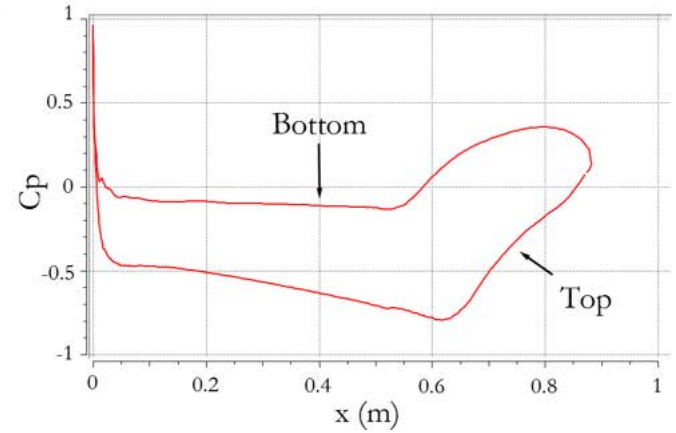


Fig. 22b Tip airfoil pressure coefficient plot

CFD analyses were performed on tip and root airfoil profiles to determine the location of the transition to turbulence. The analyses are simulating the stream wise flow speed of 80 *kts.* with ISA atmospheric conditions at 9,500'. The chord length selected for the analysis corresponds to the final wing planform geometry. A structured mesh was constructed and refined near the boundaries according to  $y^+$  rules for modeling transition. A shear stress transport turbulence model was coupled with a  $\gamma\theta$  transitional model. The sand roughness and geometric roughness were prescribed to be  $0.509016 \mu\text{m}^{25}$  and  $0.05 \mu\text{m}^{26}$  respectively. As it can be observed from the pressure plots, the airfoils feature a “rooftop” shape pressure coefficient plot, indicating the existence of favorable pressure gradients for a large portion of the airfoil chord.

## 6.2 Wing Planform Optimization

As presented in Sec. 4.1, one of the first steps in determining the general dimensions of Pandion was to establish the wing aspect ratio. Using the results of the preliminary drag analysis, it was determined that a high aspect ratio wing would maximize range for the longest flight segments

(cruise and loiter). After a detailed drag analysis was performed on Pandion, it was possible to make a more detailed study on the effect of AR on the overall performance and efficiency of the aircraft.

The aspect ratio directly affects the aerodynamic performance of the aircraft, as it has a direct effect on reducing the induced drag. A lower induced drag results in a lower required power and, for the same battery, a longer range. However, a very large aspect ratio might result in undesirable aeroelastic flutter which can have catastrophic effects on the structure. Therefore, it is important to optimize the AR for both performance and safety reasons. A detailed sensitivity study was made, following the process described in Sec 4.1, using the results of the detailed drag analysis. The results of this study are summarized in Fig. 23. As in the preliminary study, the optimum AR value is achieved as the value of the derivative  $\partial R / \partial AR$  is close to zero. If range was plotted against aspect ratio, a maximum range would occur at this value of AR. However, the derivative reaches zero at a very high AR ( $\sim 21$ ), resulting in structural problems associated with wing flutter. Therefore, a value of 18.35 was selected as the final design point for the AR of the wings, signifying a synthesis between airplane performance and airframe safety. Given the wing area of  $136.3 \text{ ft}^2$ , a wingspan of 50' is obtained for Pandion. Since this span is longer than the width of the 40' T-Hangars required by the RFP, UACC has decided to implement a wing folding mechanism, which will be described in Secs. 7.4 and 14.1.

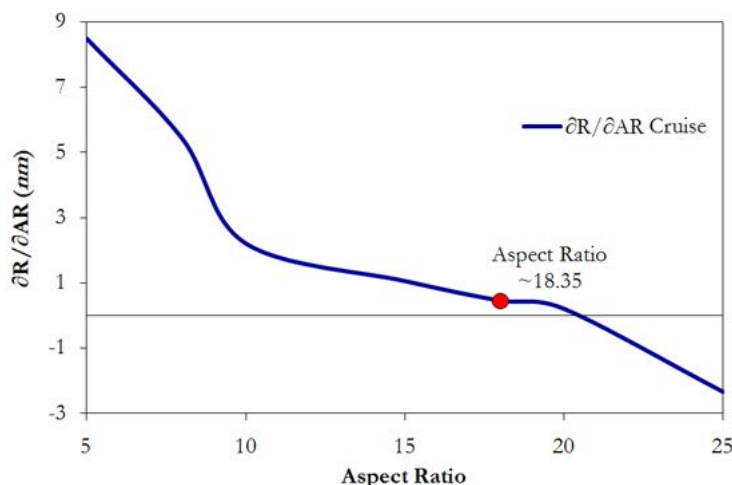


**Fig. 23 Results of Aspect Ratio analysis using a detailed drag analysis. For simplicity, the results of loiter are not shown since its  $\partial R / \partial AR$  derivative did not change significantly. Wing aspect ratio selected as 18.35.**

### 6.3 Winglets

To improve the aerodynamic efficiency of the wing and lower the lift-induced drag, winglets were implemented into Pandion. Particular attention was paid to the loft generated between the wingtip chord and the winglet root to ensure a smooth transition preventing adverse effects that may arise from rapid curvature changes near the wingtip<sup>27</sup>. The PSU 94-097 airfoil was selected for the cross-section of the winglets because it is specially designed and optimized for the purpose of minimizing interference with the wing pressure field. Additionally, it helps to maximize the wing's yawing moment coefficient, therefore assisting in the overall lateral directional stability of the aircraft<sup>28</sup>. Figure 24 presents a CFD analysis of the local pressure distribution on the winglet airfoil. Given that the winglets are installed at the tip of a relatively high aspect ratio wing, it was decided that they should be manufactured using lightweight and stiff carbon-fiber honeycomb materials to reduce their adverse effects on wing flutter. Figure 25 presents the final integrated geometry of the winglets.

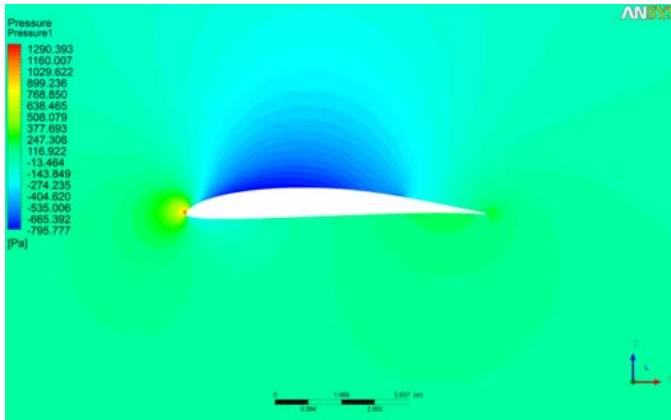


Fig. 24 CFD analysis of the local pressure distribution on the winglet airfoil

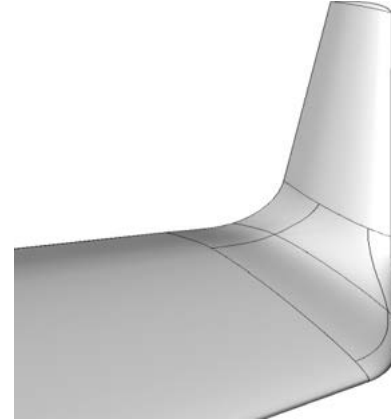


Fig. 25 Winglet geometry

### 6.4 High Lift Devices

The strategy to maintain maximum laminar flow on the wing surfaces dictated that no moving part on the leading edge should be incorporated. This led to the decision to incorporate only the most efficient trailing edge devices that can generate a  $C_{L_{max}}$  up to 2.0, as was assumed in Sec. 2.5, given that the flap will extend to 76% of the wing half-span (as dictated by the location of the wing folding line).

Reviewing the ESDU Data Item 95021<sup>29</sup>, it was determined that a set of single-slotted Fowler flaps would generate sufficient lift for this purpose.

Using Roskam's<sup>30</sup> method for sizing flaps, a parametric study was performed to determine the required flap chord to wing chord ratio that will generate sufficient  $C_{L_{max}}$  at takeoff and landing.

Figure 26 shows the results of this analysis for flaps having a streamwise extent between 15% and 35% of the wing chord. The takeoff and landing position of 30° and 35°, respectively, were selected for a 30% flap chord to wing chord ratio. Efforts were made to define

the geometry of the flap segments to ensure attachment of an accelerated airstream through the flap vane with the flaps deployed. A low speed, steady-state CFD analysis was used to verify the attachment of flow, as well as a maximum lift coefficient exceeding 2.2, attained at landing conditions with a flap deflection of 35°. Figure 27 presents the results of this analysis as velocity contours and pressure gradients.

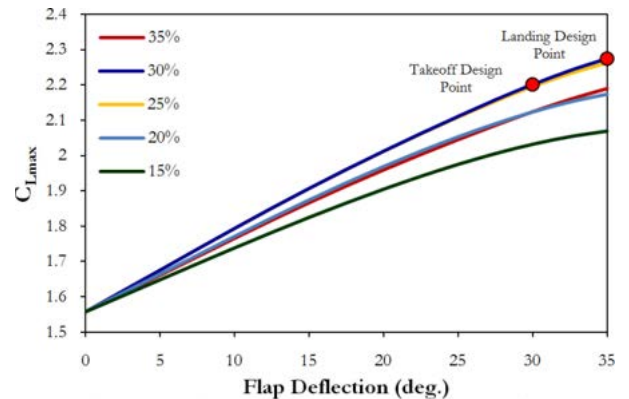


Fig. 26 Aircraft maximum lift coefficient vs. flap deflection for different flap chord to wing chord ratios. The takeoff position of 30° and landing flap setting of 35° are indicated for 30% flap to wing chord ratio.

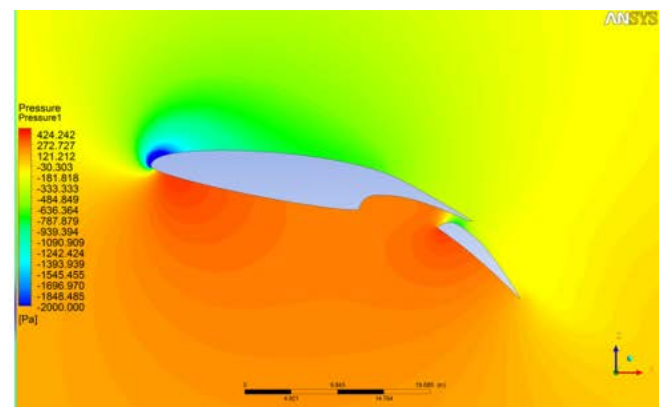
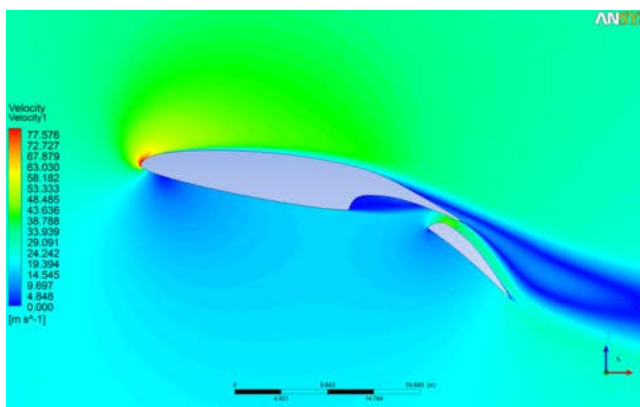


Fig. 27 CFD analysis on wing section with flaps, at landing conditions with a flap deflection of 35°. Left displays velocity contours and Right displays pressure contours.

## 6.5 Wetted Area Distribution

To perform detailed Class II<sup>31</sup> drag estimations, a precise measurement of the wetted area of the airplane was necessary. This was accomplished after initial CAD surface models for the

configuration were finalized. The areas were extracted numerically with high precision tools and were used in the drag calculations that are presented in the sections to follow. Table 6 and Fig. 28 summarize the result of the wetted area distribution analysis.

**Table 6 Summary of Wetted Area Distribution analysis**

| Component           | Wetted Area ( $\text{ft}^2$ ) | % Total |
|---------------------|-------------------------------|---------|
| Fuselage            | 158.49                        | 28.14   |
| Wing                | 264.86                        | 47.03   |
| Winglets            | 5.37                          | 0.95    |
| Horizontal Tail     | 82.18                         | 14.59   |
| Vertical Tail       | 18.63                         | 3.31    |
| Ventral Fin         | 6.95                          | 1.23    |
| Intake              | 3.21                          | 0.57    |
| Landing Gear Strut  | 6.49                          | 1.15    |
| Landing Gear Faring | 13.60                         | 2.42    |
| Tires (Exposed)     | 3.40                          | 0.60    |

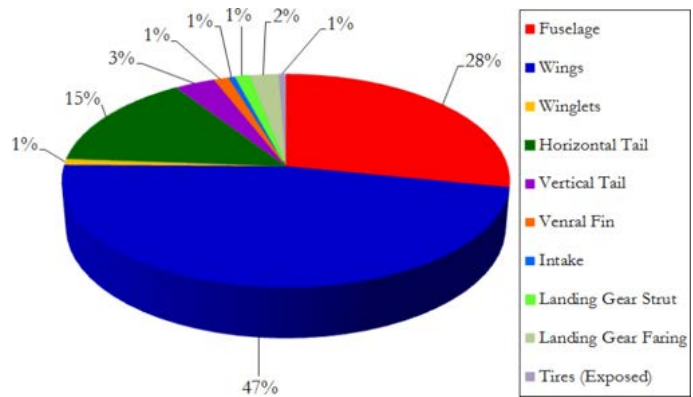


**Fig. 28 Pie Chart Representation of Wetted Area Distribution**

### 6.6 Detailed Drag Polars and Breakdown

To obtain a more accurate estimate of the lift and drag forces, a detailed analysis of the aerodynamics of the aircraft was performed using the methods presented by *Roskam*<sup>32</sup>. The high lift drag polar methodology is adopted from *Torenbeek*<sup>33</sup> and used to correct the nominal drag polars to account for drag due to deployed flaps at takeoff and landing. The results of the airfoil CFD analysis related to the verification of the extent of laminar flow, presented in Sec. 6.1, were used to compute the wing drag.

The concept of fuselage boundary layer ingestion (BLI) using a pusher propeller played an important role in prescribing the configuration choices made in Pandion. Detailed analyses were performed to quantify the improvements in the drag characteristics of the airplane. Such improvements are closely associated with favorable pressure gradients induced over the surface of the aft fuselage section. These favorable pressure gradients delay the turbulent separation, which preserves laminar flow over larger portions of the fuselage, therefore reducing friction drag. Although there exists a great deal of literature on experimental data regarding the improvements possible by preserving natural laminar flow on the fuselage using a pusher configuration<sup>34,35,36</sup>, no

analytical model was found in the public domain that would quantify such improvements. Therefore, a detailed CFD analysis was performed, the results of which were post-processed and used to correct the initial Class II drag polar for BLI effects. Figure 30 presents the drag breakdown of Pandion at cruise conditions. Figure 29 presents the results of detailed drag analysis using 5th order drag polar equations, which will be used later in Ch. 13 to verify the satisfaction of performance requirements.

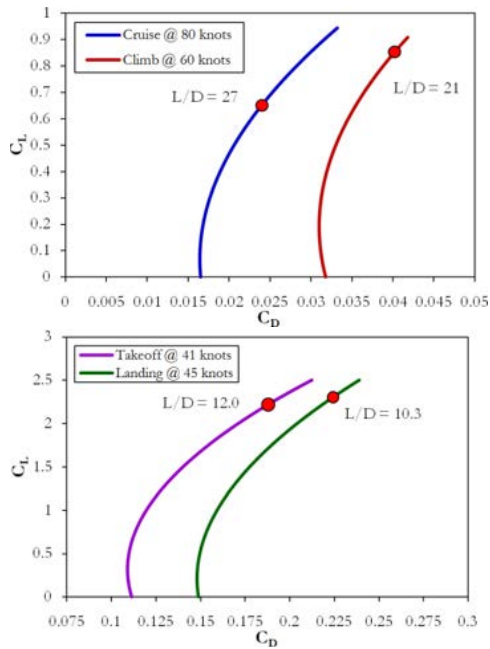


**Fig. 29 Drag Polars @ Takeoff, Climb, Cruise, and Landing**

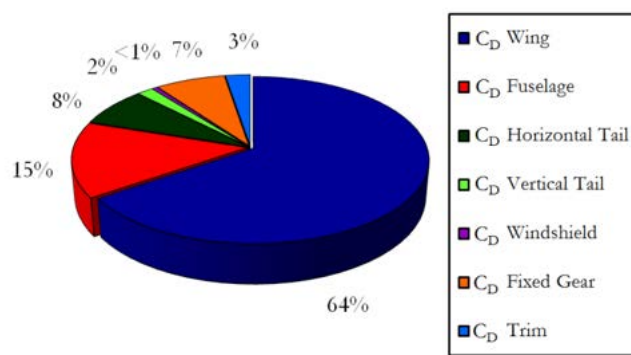


**Fig. 30 Drag Breakdown @ Cruise**

## 6.7 Full Airplane CFD Drag Verification

CFD analysis were performed to validate the feasibility of maintaining natural laminar flow on the surfaces of the airplane, as well as evaluating the parasite drag contribution of various components and the thrust generated by the accelerated and heated air exiting the fuselage from the heat management system.

A NURBS model of the aircraft's exterior surfaces was placed within the analysis domain presented in Fig. 31. Simplifications were made to allow for proper meshing of the full aircraft geometry with available computational resources.

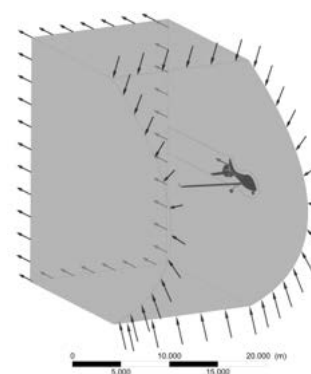


**Fig. 31 CFD Domain analysis**

Both air intakes were removed and control surface gaps were not modeled to allow for efficient meshing of the geometry. Then, using ANSYS ICEM CFD, the surfaces were meshed using an all-tri patch conforming surface mesh, with size controls placed on each surface, as shown in Fig. 32. After the placement of volumetric element control regions, an all-tetrahedral mesh was grown from the surfaces using a Delaunay algorithm in order to fill the volume with elements. In order to properly capture the boundary layer with enough detail to analyze the transition to turbulence, prism elements were grown from the surfaces into the volume mesh. With an aim of achieving a  $y^+ < 7$ , 15 prism layers were grown, with a first element height of 0.05 mm. the boundary layer elements can be seen in Fig 33.

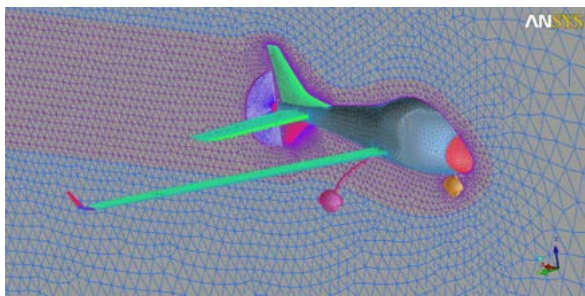


**Fig. 32 All-tri patch conforming surface mesh**

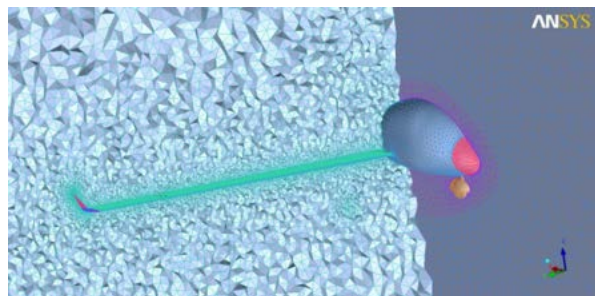


**Fig. 33 tetrahedral volume mesh**

This resulted in 9,554,665 elements connected by 2,877,301 nodes, with 5,482,144 elements being tetrahedral and 3,761,589 elements being prisms. Figure 34 shows a detailed view of the final mesh composition on lifting surfaces.

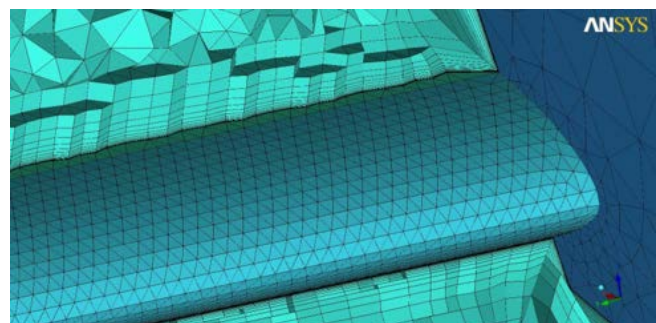


**Fig. 34 Prism volume mesh refinement to capture lifting surfaces**

ANSYS CFX-pre was used to apply appropriate boundary conditions on the model and to configure the solver for a steady-state analysis. The atmospheric conditions were set to those at cruise with a pressure of 69,674 Pa, temperature of 27.9 °F, and a flow field velocity of 107.4 ktas. Turbulence was modeled using a high resolution shear stress transport model with  $\gamma-\theta$  transitional turbulence, which allowed for the prediction of the transition from laminar to turbulent flow on the

surface of the aircraft. No-slip boundary conditions were applied to all airplane surfaces, assuming a sand roughness of  $0.51 \mu m^{37}$ , and a geometric roughness height of  $0.05 \mu m^{38}$ . The geometric height was used to correlate the transitional turbulence model. Both these heights correlate to a polished surface. The effects of the propeller were modeled using the results presented in Sec. 8.2 for the propeller's flow field on a disk shaped boundary. The exit flow from the thermal control system was modeled as a mass flow from the end of the tail cone.

The analysis was then performed using ANSYS CFX solver installed on a 64 bit computer with an eight core Intel i7 Q 720 processor clocked at  $1.6 GHz$  and allocating  $8 Gb$  of RAM. The analysis was converged to RMS values below  $10^{-3}$  over 100 iterations, which took about 6 hours.

The result of the analysis was then post processed using ANSYS CFX-post module. Pressure coefficient and kinetic energy plots were generated to verify the existence of favorable pressure gradient on the external surfaces of the aircraft, as well as attachment of the flow, and turbulence transition locations. Figures 35 through 37 present the highlights of these results.

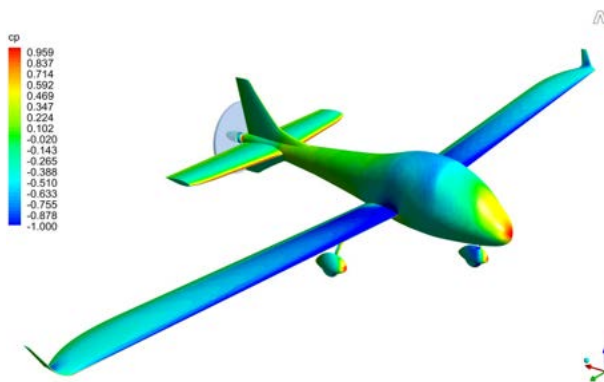


Fig. 35 Pressure Coefficient contour plot at Cruise

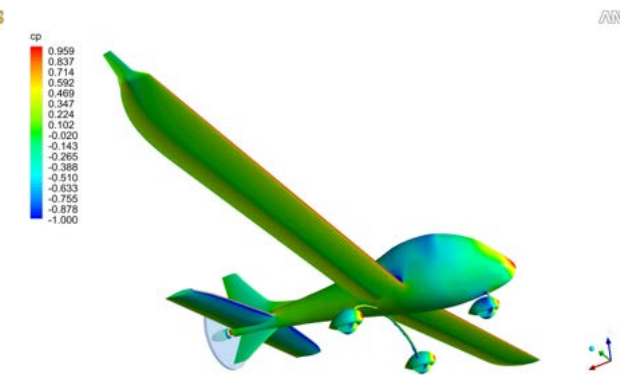


Fig. 36 Pressure Coefficient contour plot at Cruise

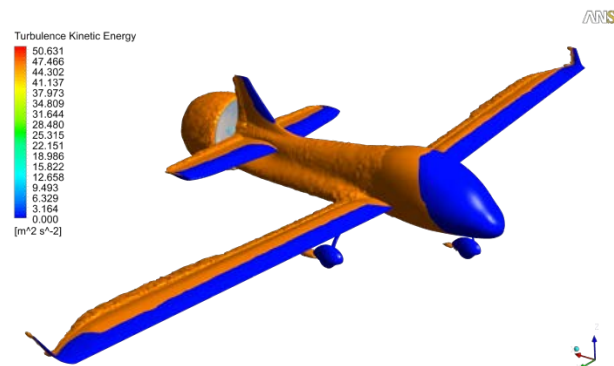
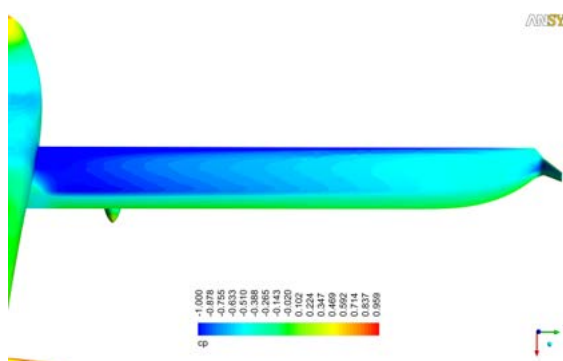
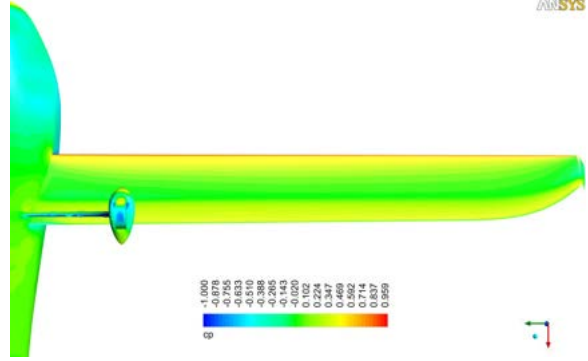


Fig. 37 Turbulence Kinetic Energy

As it can be seen in Figs. 38 and 39, the wing surfaces have substantial extents of favorable pressure gradient, so the lower surface of the wings are maintaining 70% of planform wetted area in laminar flow, while the upper surface maintains an average value of 60% laminar flow.



**Fig. 38 Pressure Coefficient contour top**



**Fig. 39 Pressure Coefficient contour bottom**

The fuselage forebody is also capable of maintaining significant amounts of laminar flow, estimated to cover 25% of the fuselage wetted area. This is assuming that transparency and door sealing is done with adequate precision to prevent the tripping of the surface flow to door and transparency edges.

Integrating shear forces acting on various surfaces of the aircraft, the breakdown of the total parasite drag was obtain and is shown in Fig. 40.

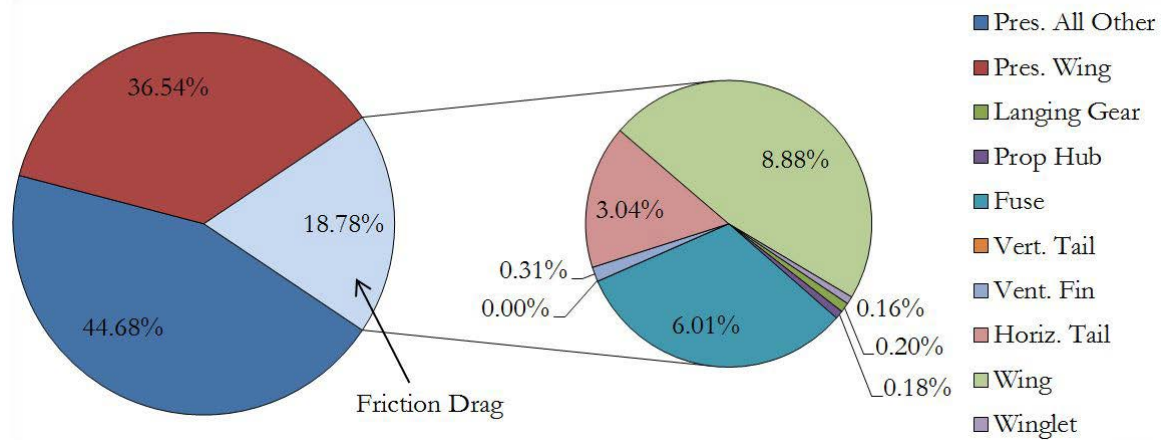


**Fig. 40 Breakdown of total parasite drag**

## 7.0 Structural Analysis

### 7.1 Loads V-n Diagram

In order to obtain the maneuver envelope for Pandion, the guidelines provided by FARs for general aviation aircraft were adopted due to the lack of directly applicable design codes for S-LSAs. The maneuver envelope was constructed using guidelines provided by FAR §23.335 to determine the critical case load factors for the structural design process of Pandion. This study indicated that the airframe is to be designed for a positive pull-up load factor of 3.8 g to occur at 88 keas at 9,500' and a negative push-over load factor of -1.52 g to occur at speeds between 55 and 83 keas. It was determined that the maneuver speed of Pandion is 85 keas. The dive speed at cruise altitude is computed to be 117 keas.

The shear and bending moment diagrams for wing and fuselage were computed along Libove's principal axes<sup>39</sup> to perform structural analysis and sizing using AAA's load module, which computes the total load by taking into account aerodynamic and dynamic loads in addition to concentrated and distributed weight sources on the lifting surfaces and fuselage structures. To accomplish this analysis, the aerodynamic loads acting on the wing structure were estimated using various high order methods presented in ESDU Data Item 8304072, the result of which is shown in terms of lift, drag, and moment diagrams in Fig. 41. The moment coefficient plotted is computed around the elastic axis of the wing considering both lift and twisting forces acting on the structure.

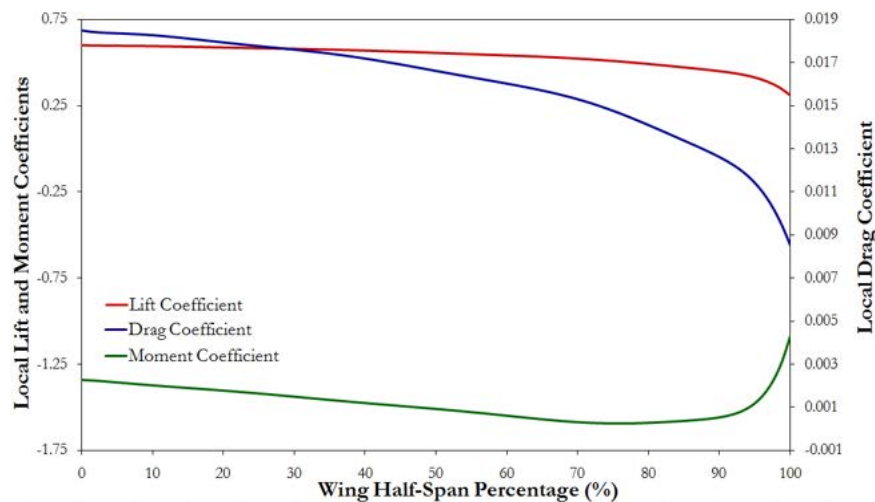
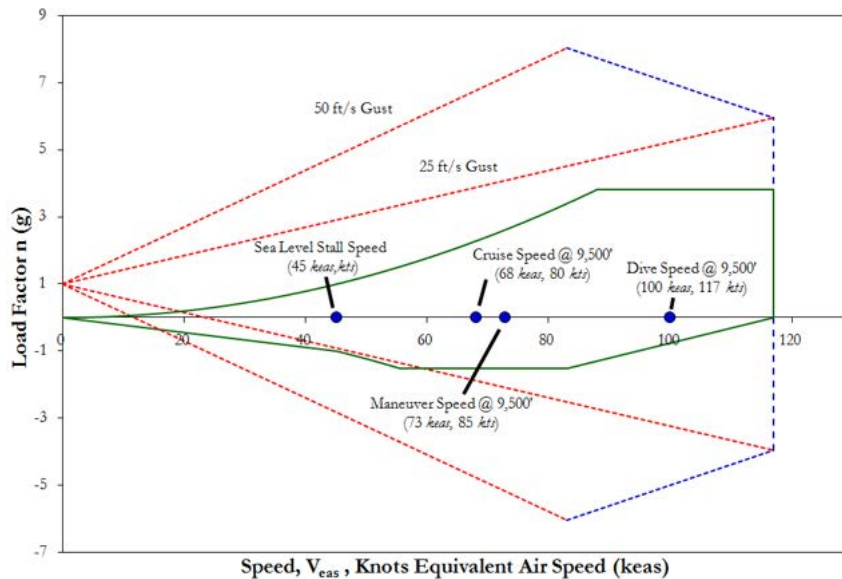


Fig. 41 Wing Loading

The loads acting on the wing structure were calculated by considering both the derived distribution of lift and drag forces as well as the torsional moment acting on the wing structure. The total acting forces and moments on the wing were computed by summing the aforementioned aerodynamic forces with the concentrated weight of the wing structure. These values were multiplied by a load factor of 3.8 to comply with the critical loading cases predicted by FAR §23.337. The final V-n diagram is shown in Fig. 42.



**Fig. 42 Maneuver Envelope**

## 7.2 Fuselage Structure

The structure of the fuselage consists of three major sections that are manufactured using carbon-fiber reinforced plastics (CFRP) with varying thickness depending on the longitudinal station of the section. Figure 43 presents the structural breakdown of the sub-assemblies of the fuselage.

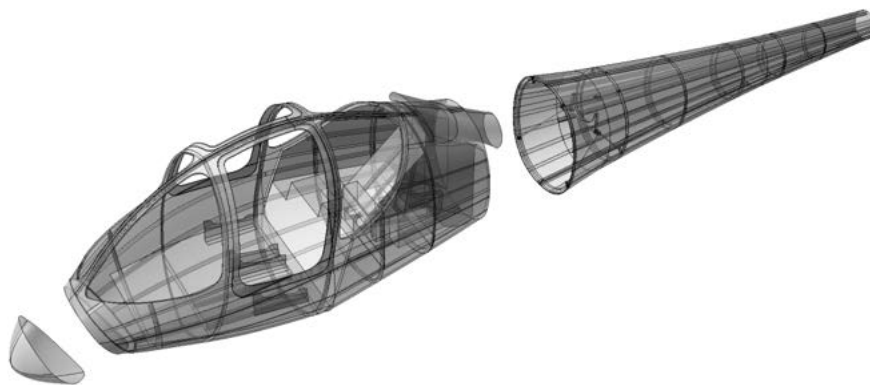


**Fig. 43 Fuselage Structural Isometric**

The outer skin is stabilized by adhesively-bounded longerons made from CFRP. The major sections of the fuselage are connected to each other via titanium links. There are also longitudinal floor beams along the cockpit that provide a base for the installation of seats as well as increased stiffness of the cockpit to improve crash survivability. Fuselage frames adjacent to cockpit doors are inclined to serve a dual purpose of stiffening the door edges and provide crash protection for the occupants along the axis of the seats. The cockpit and occupants are separated from dorsal and aft sections of the fuselage by an aluminum firewall, which also acts as cargo stowage. The wingbox extends into the main fuselage and is attached to reinforced frames via fasteners. The landing gear is also connected to the main wingbox by a carbon-fiber composite mount, which is fastened to the rear spar of the center wingbox. Figure 44 presents a view of the 3D CAD model constructed for the fuselage structure highlighting its main features.

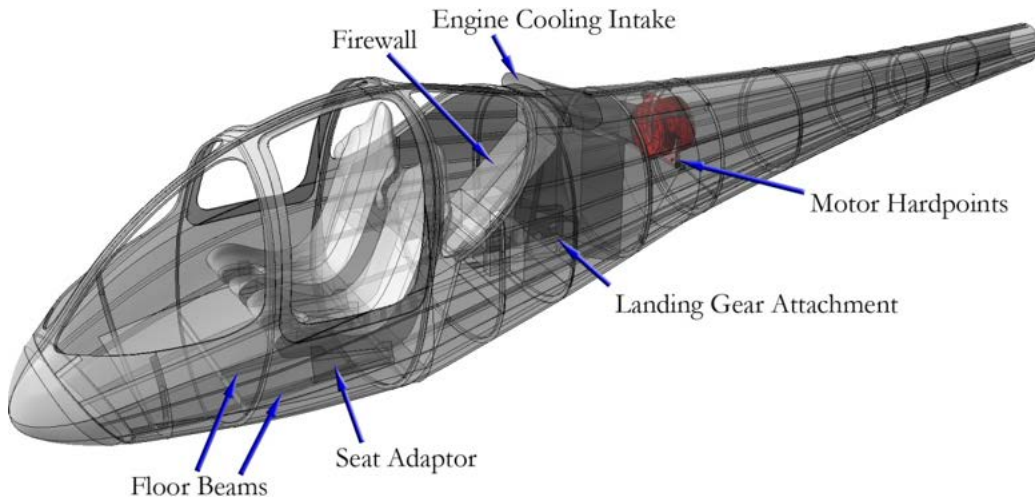


**Fig. 44 Fuselage Structural Highlights**

### 7.3 Landing Gear Attachment and Structure

The landing gear struts were designed to withstand a  $10 \text{ ft./sec.}$  sink rate as suggested by Roskam<sup>40</sup>. FEA analysis was utilized to optimize the geometry of the landing gear struts as well as their attachment points on the main structure. Low-carbon steel SAE 4130 was selected due to its high yield strength and good fatigue behavior. Figure 45 presents the results of the FEA optimization of the landing gear struts.

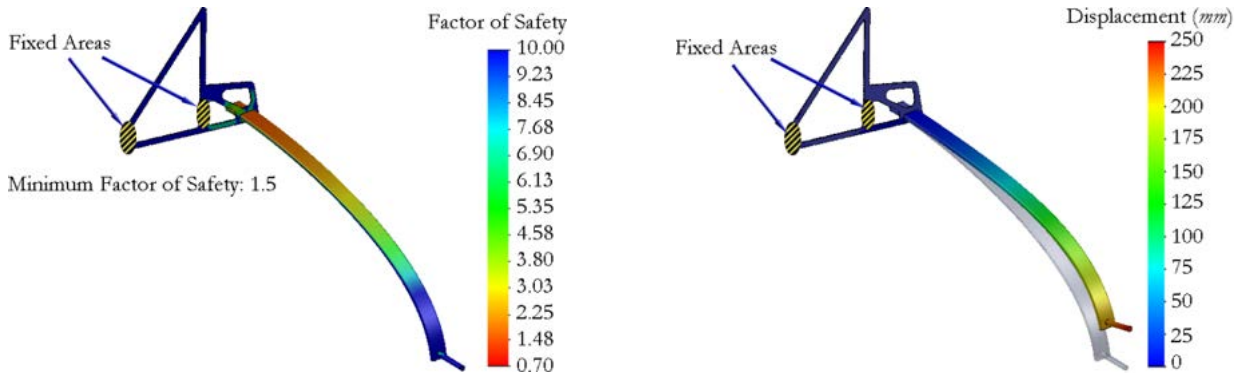


**Fig. 45 Factor of Safety and Displacement results of FEA analysis on landing gear struts**

#### 7.4 Wing Structure

The wing structure of Pandion presents a number of unique features that require novel design solutions. First, Pandion is designed to take advantage of maximum NLF on the surface of the wing to reduce airframe drag. However, slightly misaligned edges can trip the boundary layer causing unfavorable drag-increasing turbulent flow on the surface of the wing. Therefore, the wing skin structure is constructed from two single-piece, polished skin panels on the upper and lower surfaces to minimize the potential of misaligned skin panel edges, which is more likely to occur with multiple skin panels per surface. According to *Oberg et. al.*<sup>41</sup>, achieving a geometric roughness of  $0.05\mu m^*$  is feasible using modern polishing methods widely available. Second, the large wingspan of the wing planform can render Pandion incapable of using much of contemporary airport taxiways and hangers, thus UACC has integrated a wing-folding mechanism to allow the airplane to be taxied in narrow taxiways and stored in a T-hanger, as required by the RFP. Lastly, wing flutter was addressed in the design of the high AR wing planform by increasing the number of stiffener elements under the wing skin panels, which was later verified to be effective using numerical methods.

The wing manufacturing methods used for Pandion are not sensitive to the limitations of the manufacturing methods of an aluminum airframe, which restricts the size of the panels to the maximum overall dimensions of the raw material and the tooling machinery. Utilization of

\* The same assumption was applied to the CFD analysis of the wing airfoils presented in Sec. 6.1

composite materials and modern manufacturing technology allows the wing skin panels of Pandion to be laid up in two continuous pieces, therefore minimizing the potential for misalignment and the resultant turbulent flow experienced on the surface of the wing. Although this manufacturing strategy increases the size of the tooling and autoclaves needed to cure the composites after manufacturing, it improves the potential for maintaining laminar flow on the wing.

The wing super-structure consists of two primary spars, located at 18% and 65% of the chord length, and a series of composite ribs that are spaced on average 30" apart. The upper and lower wing skin panels are attached to the wing super-structure via reinforced brackets located on skin panel stiffeners that are connected to the wing ribs. The trailing edge fowler flaps are an independent structure that is installed on the rear spar. The surfaces of the trailing edge high-lift devices are constructed of composite sandwich panels, which result in a high-strength, low-weight structure. Figure 46 presents a detailed breakdown of the wing structure of Pandion.

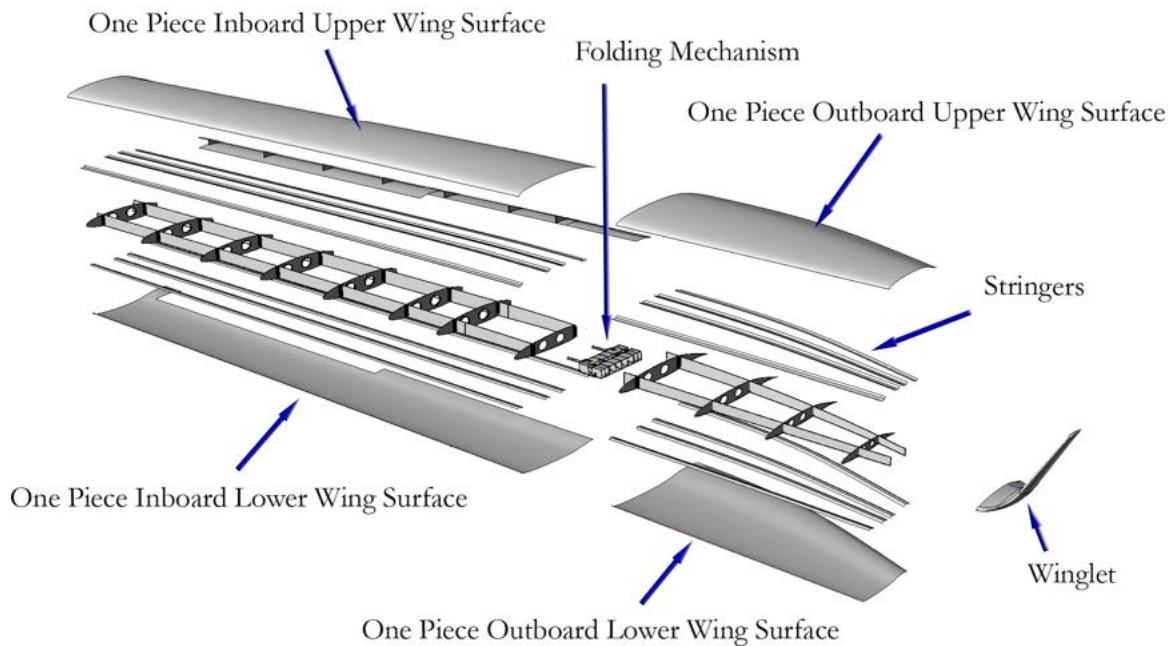


**Fig. 46 Wing Structure Breakdown**

The wing folding was accomplished through a multi-lug folding device, separating the outboard wingbox from the inboard wingbox and secured on the surfaces of the front and rear spars of the wingboxes, as well as the upper and lower skin panels. The folding is operated using electro-motors equipped with a worm-gearred mechanism and folds between the direction of the dihedral of

the wing and the direction perpendicular to the ground. The folding mechanism is secured before taxi and takeoff by mechanically operated latch pins that are inserted into the connector plate installed on both sides of the folding mechanism. Figure 47 shows the operation of the folding mechanism and Fig. 48 presents a close-up view of the locking mechanism.

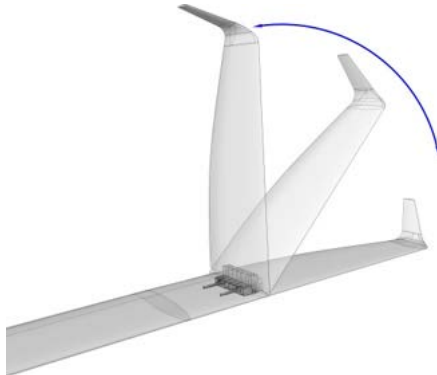


**Fig. 47 Demonstration of wing folding**

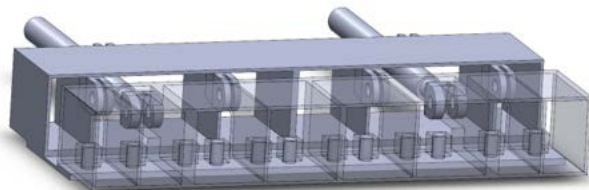


**Fig. 48 Close up of wing folding mechanism**

### 7.5 Wing Flutter Considerations

Due to the high aspect ratio of Pandion, flutter characteristics of the wing had to be considered. Numerous techniques exist for exploring the flutter characteristics of typical aircraft, ranging from pure analytic methods to procedures treating wings as a large set of coupled, damped and driven mechanical oscillators. Typically, these procedures are difficult to implement and do not yield dependable results unless considerable effort is expended to model the structural wing coefficients with as much detail as possible.

In lieu of such procedures, UACC opted for a semi-analytic method that makes use of known flutter velocities for a variety of similar aircraft and maps these flutter velocities to velocities for similar aircraft with the aspect ratio of Pandion. The procedure is based on a method of flutter analysis given by *Molyneux et al.*<sup>42</sup> which gives an analytic method for converting between flutter velocities of craft with infinite aspect ratio to craft of similar construct with finite aspect ratio. The method is completed by an empirically determined function which can be used to perform this conversion.

Using this method as a basis, UACC adopted a method of mapping flutter velocities between two crafts of similar construction, each with finite aspect ratio (as opposed to mapping

between two crafts of similar construct, one with finite aspect ratio, the other with infinite aspect ratio - as detailed by *Molyneux et al.*).

*Molyneux et al.* present an argument that the effect of aspect ratio on flutter velocity can be modeled by first considering a similar wing of infinite aspect ratio. It can be shown, by modifying the relevant quantities in the coupled oscillator equation, that the calculated flutter velocity for a finite aspect ratio craft is related to the calculated flutter velocity for an infinite aspect ratio craft of similar make by the following equation:

$$V_{\text{flutter}} = V_0 f(\text{AR}) \quad , \quad (2)$$

where  $V_0$  is the flutter velocity for an infinite aspect ratio,  $V_{\text{flutter}}$  is the flutter velocity for a finite aspect ratio (the quantity of interest) and  $f(\text{AR})$  is a function only of aspect ratio. The argument detailed in *Molyneux et al.* only shows that this equation is valid to merely consider the effect of aspect ratio by multiplicative scaling by some undetermined function (of aspect ratio only). However, it does not provide the exact form of the function - it only argues that a form with this dependence is sufficient to account for the relationship between aspect ratio and flutter velocity\*.

Determination of  $f(\text{AR})$  is necessary to complete *Molyneux et al.*'s procedure. Though possible analytically, it is simpler and more reliable to find  $f(\text{AR})$  empirically. Following this idea, UACC analyzed several sets of similar wing planforms with comparable aerodynamic and structural derivatives for each wing in a given set but varying in aspect ratio.

Using an analytically determined value for  $V_0$  (based on an infinite aspect ratio wing with the same structural and aerodynamic derivatives),  $f(\text{AR})$  was determined empirically yielding the following overall form:

$$V_{\text{flutter}} = V_0 \left( 1 + \frac{0.8}{\text{AR}} \right) , \quad (3)$$

This equation is sufficient to account for variation of flutter speed due to aspect ratio.

Now, for a new set of wings, *Molyneux et al.* suggests that  $V_0$  be calculated from a set of 2D

\* This is the extent of the result of the analytic portion of the method. For more detail on the derivation of this form, consult *Molyneux et al.*

aerodynamic strip derivatives for our wings. However,  $V_o$  can be computed using simpler methods: a craft with known  $V_{\text{flutter}}$  and  $AR$  can be used to calculate  $V_o$  for the particular family of wings sharing its aerodynamic and structural derivatives. From here, the formula can be reapplied to yield a new equation giving the flutter velocity for a new aircraft in terms of the known flutter velocity of another aircraft. Under this modification of the original method, the following equation giving the flutter velocity for Pandion is obtained:

$$V_{\text{flutter}} = V_s \left( 1 + \frac{0.8}{AR_t} + \frac{0.8}{AR_s} \right) , \quad (4)$$

where  $V_s$  is the measured or calculated flutter velocity of a structurally and aerodynamically similar reference aircraft,  $AR_t$  is the aspect ratio of Pandion,  $AR_s$  is the reference aspect ratio, and  $V_{\text{flutter}}$  is the calculated flutter velocity for the craft. Using listed values of  $V_{\text{NE}}$  and  $V_D$  for various aircraft which are relatively similar to Pandion, as well as regulations concerning the relationship between these velocities and flutter velocity, lower bounds for the flutter velocities of these various aircraft were derived. Using Eq.4 and the calculated flutter velocities (as well as the corresponding aspect ratios) of the reference aircraft, it is possible to create a list of possible  $V_{\text{flutter}}$ 's.

The sample aircraft were assumed to cover an extensive range of structural and aerodynamic characteristics similar enough to Pandion so that it falls somewhere within the parameter space mapped out by the sample aircraft. Therefore, the lowest estimate of  $V_{\text{flutter}}$  given by these aircraft is a worst case scenario for Pandion, since the previously estimated values for the various  $V_s$  are already pessimistic. Thus, it was found that it is highly unlikely for Pandion to have a flutter velocity below this worst case estimate. Therefore, if the estimated flutter velocity exceeds the velocity necessary for regular operation, Pandion satisfies the flutter requirements with high probability. Due to the extremely conservative and empirical nature of this estimate, UACC believes that its results are as dependable as those obtained by performing a computationally intensive analysis, but requiring significantly less effort. Using the procedure, a worst case value of 147 *kts*. for  $V_{\text{flutter}}$  was calculated, which is above the operational speed requirements, as discussed in Ch. 13.

## 7.6 Empennage Structure

The vertical tail of Pandion features a similar structure as the wing in terms of architecture and composite material application. The horizontal tail is supported through a linkage to two fuselage frames. The elevator incidence angle is varied by a double redundant mechanical system installed inside the horizontal tail of the aircraft. Figure 49 presents the general structural arrangement of the empennage of Pandion.

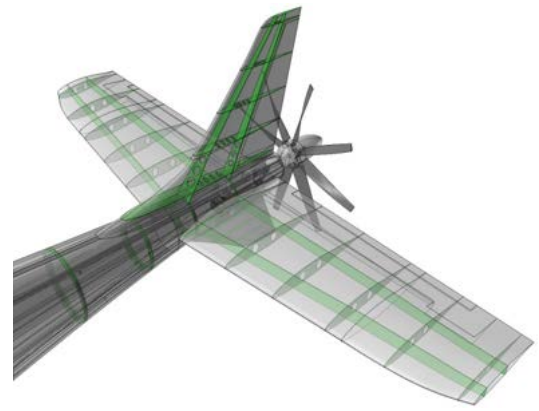


**Fig. 49 Empennage Structure**

## 7.7 Manufacturing Methods

Due to the utilization of carbon laminated composites, Pandion is able to be manufactured using modern automated composite laying methods. These methods allow for manufacturing of large, continuous pieces of structure rather than the conventional method that relies on manufactured sub structures to create larger assemblies. The fuselage structure of Pandion is to be manufactured in computer controlled, rotary matrix laying barrels that will be cured with heat and pressure to ensure obtaining the required mechanical properties. Wing skins are to be laid in large, continuous pieces, eliminating the possibility of small surface misalignments, then are polished to obtain an average geometric roughness of  $0.05 \mu\text{m}$ . If the wing surfaces of Pandion are manufactured using conventional methods, these common misalignments (present at manufacturing or created during the service life) can lead to the tripping of the boundary layer, therefore making the implemented NLF technology less effective. Compatibility of the structural design of Pandion with modern manufacturing methods allows for higher production rates and buy-to-fly ratios. Higher rates of production allows for substantial reduction in the overhead cost per plane and higher buy-to-fly ratios allow for significant reductions in the cost of raw materials used to build the aircraft. The exploded weight group foldout in Ch. 11 presents the material distribution and the structural breakdown for Pandion.

## 8.0 Propulsion

### 8.1 Electromotor Type Selection

In order to maintain a low overall weight figure and a high efficiency, various types of electric motors were studied to be used as a powerplant for Pandion. Given that available battery technologies only produce direct current (DC), a tradeoff was observed between using a lower weight AC motor in need of a separate power inverter unit (DC/AC converter) and using a heavier DC motor with no need of a converter. Performing a survey of existing types of electro-motors from various manufacturers, UACC concluded that a DC brushless motor is the best available electro-motor type for the configuration. DC brushless motors typically have higher efficiencies than other comparable DC motors and have a simpler mechanical construction with no need of complex control circuits to regulate RPM<sup>43</sup>. Table 7 presents a summary of the most promising choices of electric motors studied.

Table 7 Summary of Motor Selection Study

|                          |              | <b>Yuneec Power Drive 60</b> | <b>UQM Powerphase 75</b> | <b>AC Propulsion Drive</b> | <b>BRUSA ASM8.24.10</b> |
|--------------------------|--------------|------------------------------|--------------------------|----------------------------|-------------------------|
| Type                     | Brushless DC | Brushless DC                 | AC Induction             | AC Induction               |                         |
| Weight (lb.)             | 66           | 90                           | 110                      | 150                        |                         |
| Accessory Weight (lb.)   | 20           | 35                           | 66                       | 21                         |                         |
| Operational Weight (lb.) | 86           | 125                          | 176                      | 172                        |                         |
| Max Power (hp)           | 81           | 100                          | 268                      | 82                         |                         |
| Power Density (hp/lb)    | 1.23         | 1.11                         | 2.44                     | 0.55                       |                         |
| Max Torque (lb-ft)       | 410*         | 176                          | N/A                      | 400                        |                         |
| Max Efficiency           | 92           | 94                           | 90**                     | 93                         |                         |

\*Calculated; \*\* Approximate

### 8.2 Propeller

The propeller design for Pandion was based on the constraints defined by the overall geometry of the airplane, as well as by the motor selected. The location of the propeller aft of the airplane and the overall geometry of the fuselage and the landing gear limit the maximum diameter of the propeller. Taking into account the required ground clearance during takeoff rotation, a

maximum allowable propeller diameter of 4.6' resulted from the constraints. A higher diameter propeller is desirable since it reduces the RPM required to produce the same thrust compared to a smaller propeller. Therefore, a diameter of 4.6' was set as the design point for the propeller of Pandion.

*JavaProp*, a java-based propeller design applet created by *Dr. Martin Hepperle*, was used to design and evaluate several propellers taking into account the aforementioned constraints (motor performance and design diameter). Minimizing the noise produced by the propellers was also one of the design goals. As suggested by Hartzell Propeller Inc., UACC designed a propeller with a high number of blades to reduce propeller noise <sup>44</sup>. The effects of the number of blades on efficiency, weight, and thrust produced were evaluated, and it was determined that an 8-blade propeller would be implemented given its higher relative performance and the small effect the increased number of blades has on the propeller weight (around 16 *lb.* increase relative to 3-blade propeller, which is counteracted by the smaller battery required). Figure 50 shows the 8-bladed propeller designed.

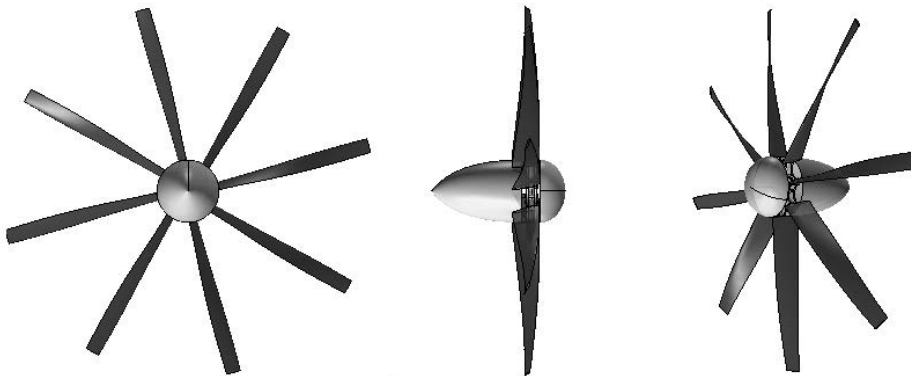


**Fig. 50 Pusher Propeller CAD Model**

The performance of the propellers was evaluated at all critical flight conditions, with the efficiency at cruise being the design-driving factor given its significant effect on total energy required. For each flight condition, the velocity and the required thrust were known from the detailed aerodynamic analysis, and after setting the number of blades, the rotational speed was the last main parameter to be determined. The maximum power output of the motor, 60 *kW*, is produced at 2,400 RPM. From *JavaProp*'s results, it was observed that the propellers optimal in a range of RPMs close to the optimal RPM of the motor would have a high efficiency. This made it

possible to use a gearless propulsion system, in which the propeller is directly driven and rotates at the same RPM as the motor.

A cruise value of 1,800 RPM was selected after evaluating propeller efficiencies corresponding to several RPMs. Four different airfoils designed by *Hepperle* and included in *JavaProp* were used along the radial direction of the propeller, for which the applet optimizes the propeller twist distribution. The result is a propeller with a cruise efficiency of 88%. The efficiency and thrust curves of the propeller at cruise are shown in Fig. 51. Additionally, the propeller presents high efficiencies in other flight conditions, with all the efficiency values being above 70%.

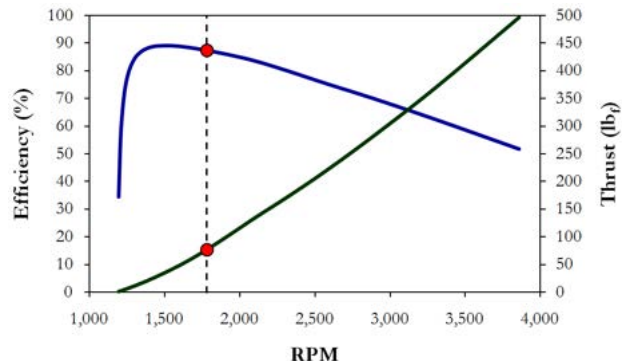


Fig. 51 Results of propeller efficiency analysis @ cruise

A tilting mechanism was designed to allow for the propeller to be tilted 10° downwards, as shown in Fig 52. For this purpose, the driveshaft is split into two parts connected by a U-joint. An electric linear actuator is attached to the aft shaft and produces the required force to tilt the aft shaft/propeller system. A close-up of the propeller tilting mechanism is presented in Fig. 53. Tilting the propeller downwards affects the dynamics of the aircraft in two ways: First, the resulting inclined thrust has a component directed upwards, which adds to the lift of the airplane. Second, the resulting thrust vector is not aligned with the CG of the airplane. This misalignment results in a moment arm which generates a negative pitching moment (nose-down) over the airplane. The latter effect can be used in deep stall situations in which flow separation prevents the elevator surfaces from being effective.

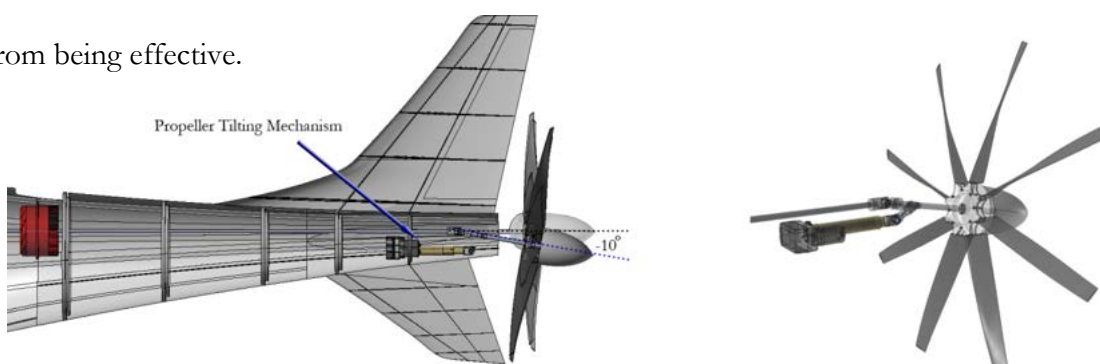


Fig. 52 Propeller tilting mechanism with -10° propeller deflection

Fig. 53 Propeller Tilting mechanism close-up

## 9.0 Electrical Systems

### 9.1 Electrical Storage

As it was previously stated in Sec. 2.2, lithium-air batteries possess sufficient energy while having the lowest weight and development risk of all comparable battery types. A survey of developers of modern battery technologies indicated that at present there are two main entities that are working towards commercialization of lithium-air battery technology, namely *PolyPlus* of Berkeley, CA and the University of Dayton Research Institute in Dayton, OH. Contact was made with the published researchers<sup>45</sup> in these organizations and, as a result of their cooperation, information was obtained regarding the performance and viability of using a lithium-air battery as the primary energy source for aerospace applications in the near future.

It was determined that, given their solid-state nature, there are no special safety concerns regarding lithium-air batteries, such as explosions or catastrophic failures. From the correspondence, it was also determined that lithium-air batteries possess an efficiency of 70% at high drain rates and an estimated energy density of 1,000  $Whr/kg$ . The lithium-air electro-chemical process is determined to be highly exothermic, which requires a dedicated high-performance cooling system integrated with the battery pack. It was also established that, by 2016, such batteries will be made available commercially. An estimated minimum five-year shelf life and over 500 charge cycles are projected for a commercialized lithium-air battery unit. It was also confirmed that the lithium-air battery unit has to be operated at relatively high temperatures, generally greater than 120 °F. Given this information and the most accurate estimation of the required amount of energy to fly the mission specified by the RFP (presented in Sec. 2.3), a battery pack was designed taking into account its integration with the dorsal fuselage section. Figure 54 presents a view of the battery pack design. Considering that the battery pack is made up of hundreds of small cells<sup>46</sup>, the outer geometry of the pack can be tailored to fit in otherwise unused spaces in the aircraft. The battery pack was designed to utilize some of the unused space in the lower

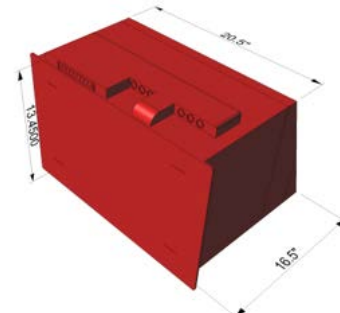


**Fig. 54 Battery pack**

fuselage section. An onboard battery charger/monitor rectifies alternating current from a conventional electrical outlet to direct current required to charge the battery. The performance of the charger will be discussed further in Sec. 14.2.

## 9.2 Electric Distribution Architecture

The presence of a high-voltage motor as well as low-voltage components dictates that the electric architecture of Pandion must feature two voltages of  $166\text{ V}$  and  $28\text{ V}$ , respectively. This requires the implementation of a DC-DC converter to extract the  $28\text{ V}$  electric current from the high-voltage ( $161\text{-}190\text{ V}$ ) battery. The high current demand of the motor ( $342\text{ A}$  max.) requires two wires to carry each of the three phases to minimize voltage loss and eliminate the need for a complex, heavy, and expensive circuit breaker. The architecture was fully simulated in the *Simulink* environment to verify the behavior of the system via validating steady-state currents, motor speed, and mechanical torque produced by the motor in various flight conditions. A sample signal reading is presented after the electrical system foldout.

The requirement of specific voltages and currents for the motor to operate as desired at every flight condition makes it necessary to implement an advanced power management system. This system acts as a controller, determining the optimal current and voltage levels that must be supplied by the battery to the motor. The unit creates the desired three-phase output for the motor from a DC current provided by the battery. Another smaller control system is used to regulate the low-voltage ( $28\text{ V}$ ) electric circuit, comprised of the prop-tilting actuator, cockpit lighting, and instrumentation.

## 9.3 Avionics and Secondary Electrical Components

A number of secondary electrical components are present in Pandion, including the avionics system, the lighting system, and the prop-tilting actuator. The avionics package consists of a combination of multi-function displays (MFDs) and backup analog instruments. The main element is the *Garmin GTN™ 750*, a  $7''$  digital MFD that has all of the relevant flight indicators, e.g. artificial horizon, altitude, rate of climb, airspeed, horizontal situation indicator, and G-meter. Additional

units display the motor parameters, e.g. power and RPM, and navigational maps. On the co-pilot side of the cockpit, flight-test instruments are installed to obtain measurements and relevant information in the prototype aircraft. Figure 55 shows the cockpit layout of a flight test airplane model.

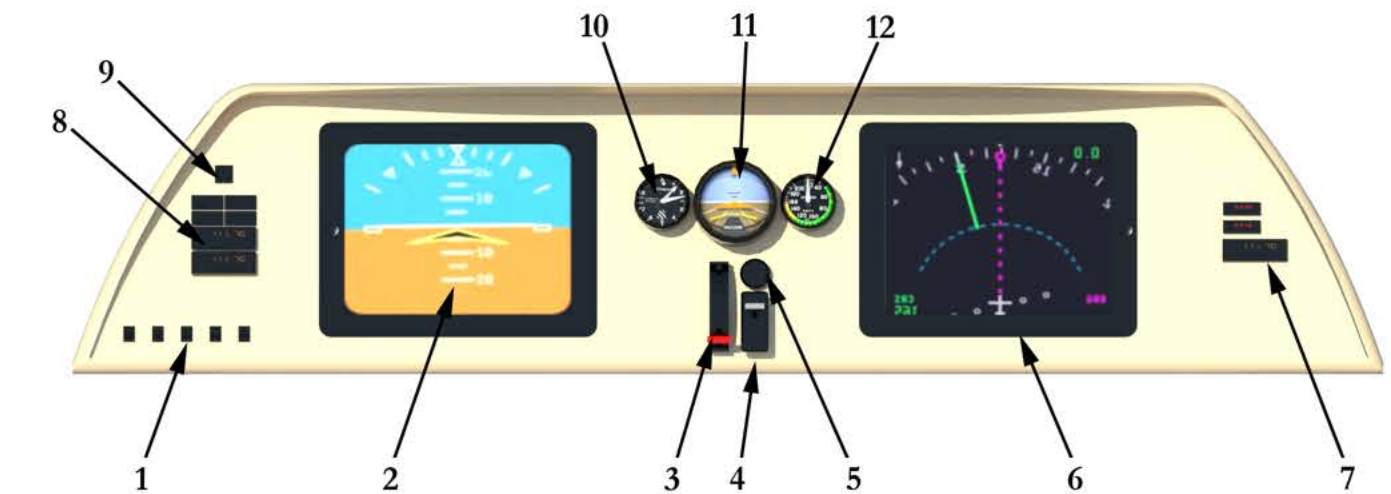
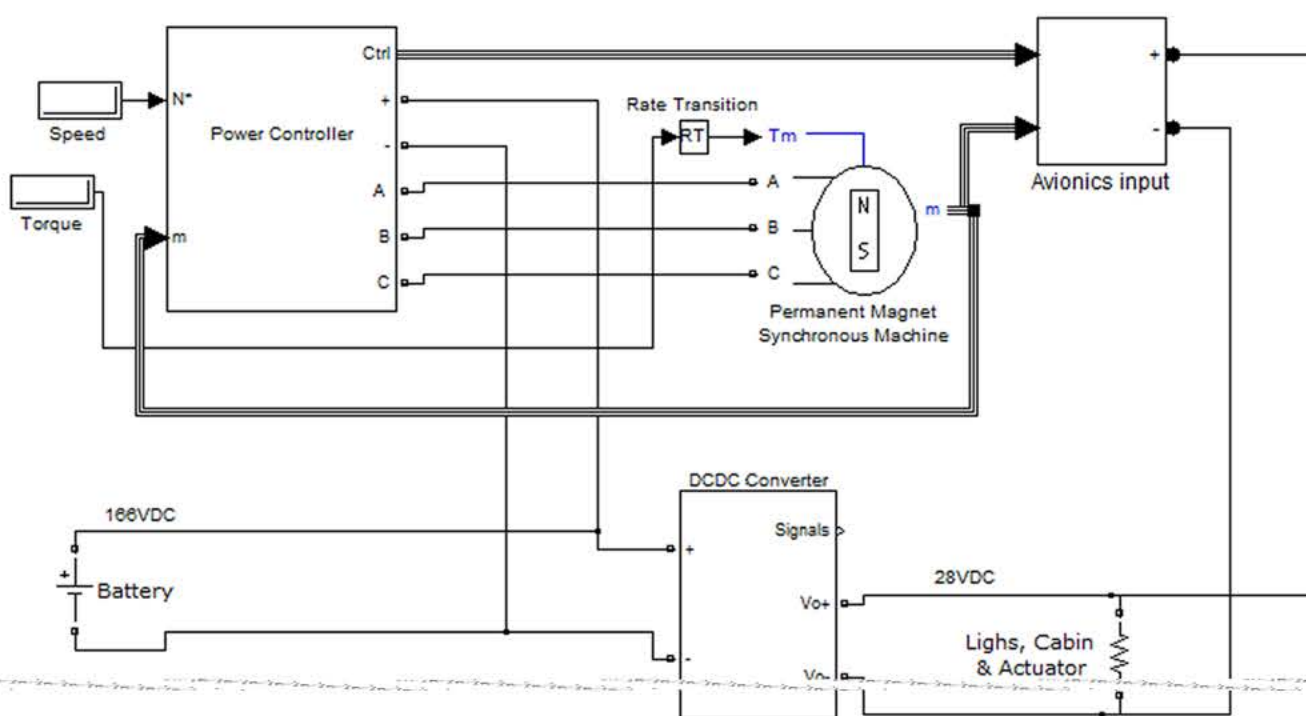
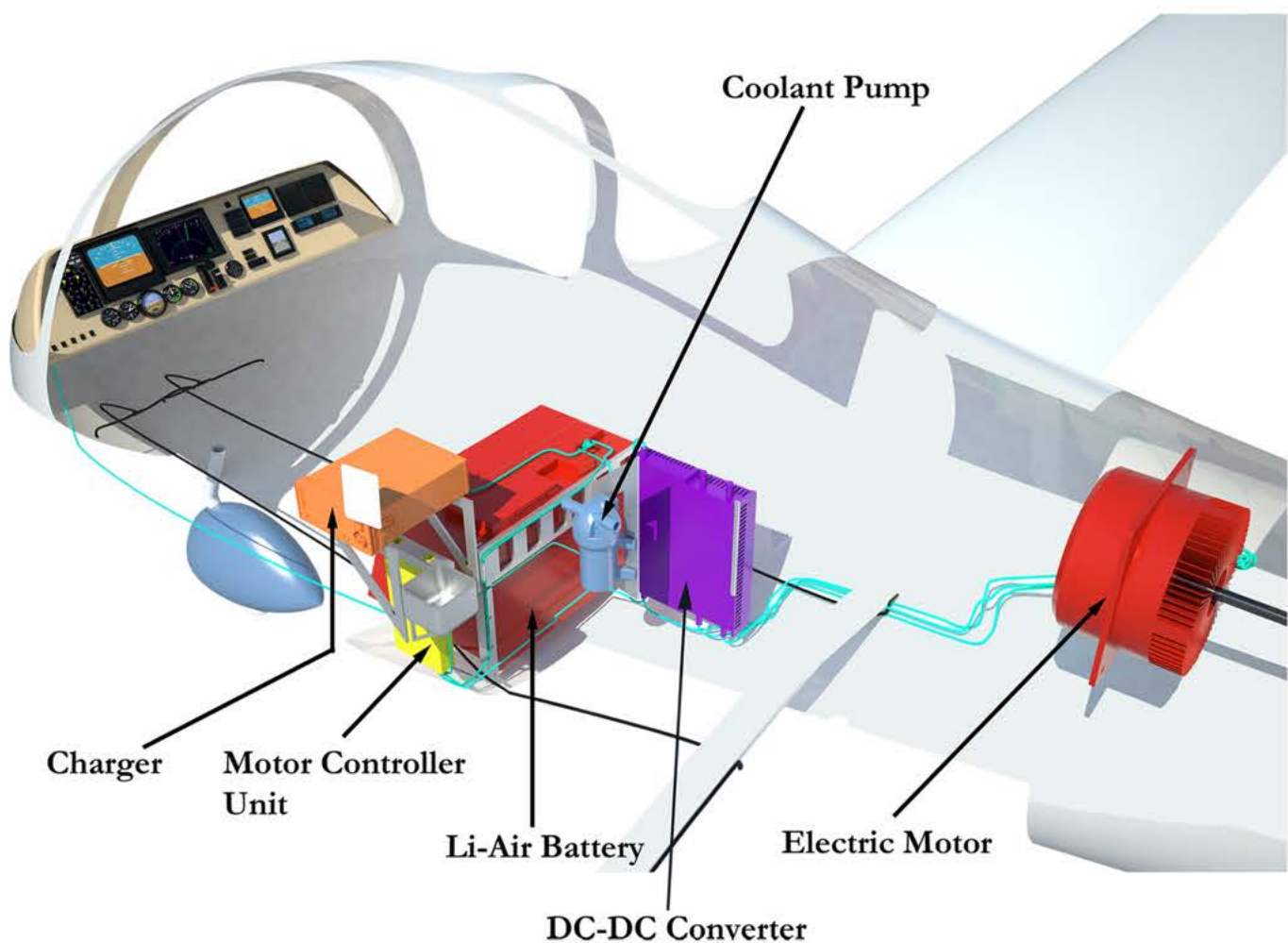


Fig. 55 Cockpit layout in a prototype airplane

The commercial version of Pandion will be available with a variety of options for instrumentation ranging from an iPad-based system developed by *Amapola Flyg*<sup>47</sup> to an all-in-one GPS/Nav/Comm *Garmin* system. The iPad-based instrumentation will require an external GPS signal antenna to increase the accuracy of the GPS processors installed. The antenna would be located on the tip of the vertical tail. All the configurations include a battery energy level indicator.

The propeller-tilting mechanism is activated autonomously when a deep stall is detected by the air data computer of the aircraft. The *Nook CC* 4"-travel 24 VDC electrical linear actuator was selected given its low weight and high static capacity (3,000 lb.). The electrical system foldout shows the main components of the electric system, including the avionics layout and the electric architecture.

# Pandion



Production model instruments panel



Test flight instruments panel

1. Electric switches
2. ipad unit with instrumentation software
3. Flap position heaver
4. Throttle
5. Battery charge indicator
6. Secondary passenger ipad unit (optional)
7. Secondary radio panel (optional)
8. Primary radio panel
9. Radio unit power switch
10. Analog altimeter (optional back-up)
11. Analog attitude indicator (optional back-up)
12. Analog air speed indicator (optional back-up)
13. Analog rate of climb indicator (optional back-up)
14. Propeller RPM indicator
15. Prototype test radio compass
16. Video camera display
17. Prototype test telemetry display
18. Electric/thermal systems display
19. Bank/turn indicator
20. Flight engineer attitude indicator
21. Data recorder multi-function panel

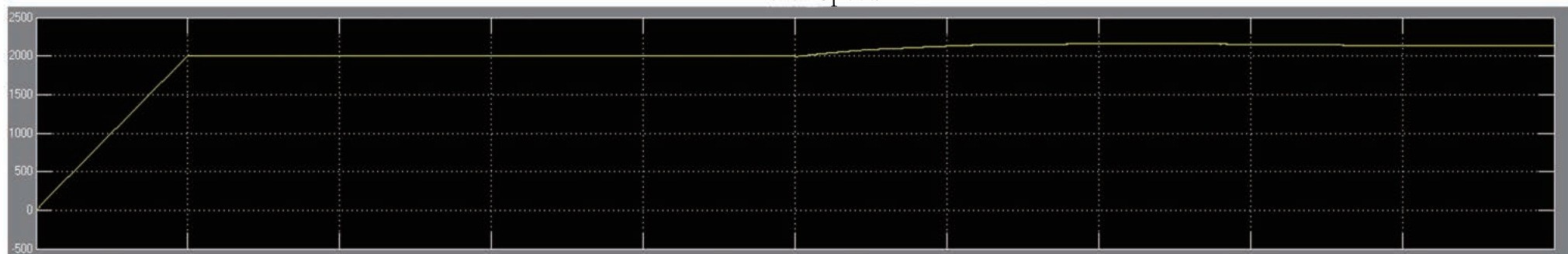
Input 1, Take offh  
Speed 2000 rpm  
Torque 46 N\*m

Input 2, Climbing  
Speed 2200 rpm  
Torque 170 N\*m

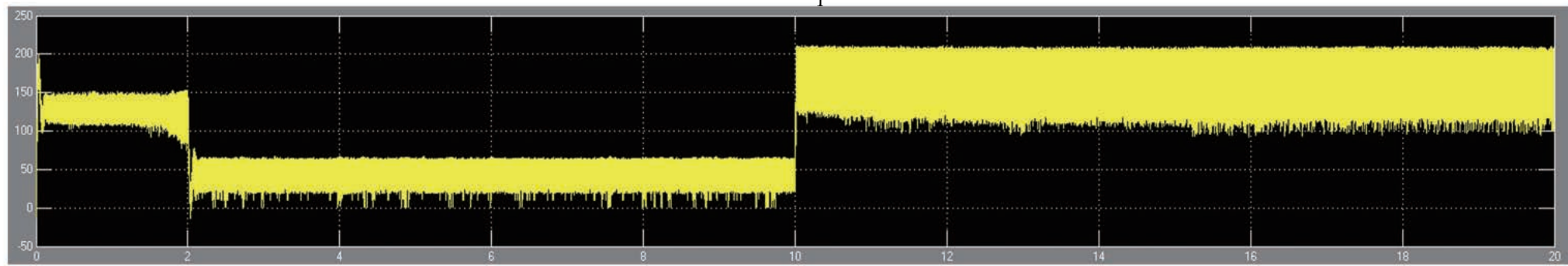
Stator Current



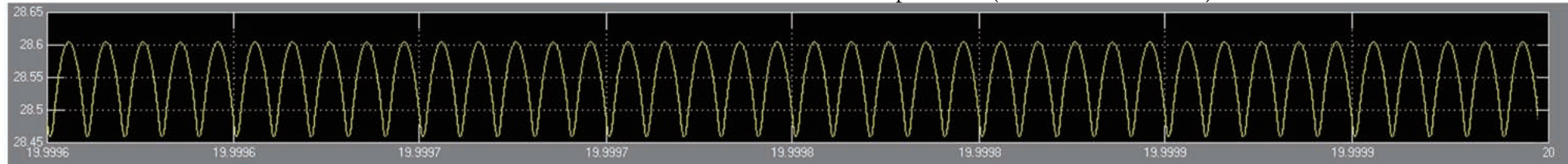
Rotor Speed



Torque



DC-DC Converter Output Volt (Perturbation <0.5%)



## 10.0 Systems Integration

### 10.1 Heat Management

The use of high-powered electric and electronic systems results in a large quantity of heat that must be dissipated to maintain optimum operating conditions. An advanced heat management system was designed combining liquid-cooled and air-cooled systems to dispose large amounts of excess heat. As suggested by Tesla Motors<sup>48</sup>, a liquid-air plate-fin heat exchanger was used for cooling the battery pack due to its low weight and high volume-to-surface area ratio<sup>49</sup>. The heat exchanger for the system was sized using methods outlined by *Hesselgreaves*<sup>50</sup> to determine its overall volume and weight as well as the required mass flow of the cooling liquid and air. The heat generated by the battery, summarized in Table 8, was

**Table 8 Power used and heat generated at critical flight conditions.**

calculated in order to size the heat exchanger. The heat was calculated by assuming that the battery power inefficiency was dissipated in the form of heat.

| Flight Condition | Power (kW) | Heat (kW) |
|------------------|------------|-----------|
| Takeoff          | 37.7       | 17.0      |
| Climb            | 12.2       | 5.2       |
| Cruise           | 12.3       | 5.3       |
| Descend          | 92.7       | 4.0       |
| Landing          | 10.0       | 4.3       |

The heat exchanger was designed to dissipate a maximum of 17 kW of heat as dictated by the battery heat generation during takeoff. It was determined that a maximum water flow rate required to remove the heat generated to be 3.0 gal./min. The maximum airflow at standard conditions is 195 *cfm*. To circulate the cooling fluid, the *Flojet* Quad Pump 4000 Series, an electrically-driven water pump capable of inducing 5.0 gal./min., was selected because it satisfied the required flow rate while having the lowest weight. Figure 56 shows the location of the battery cooling system in the fuselage.

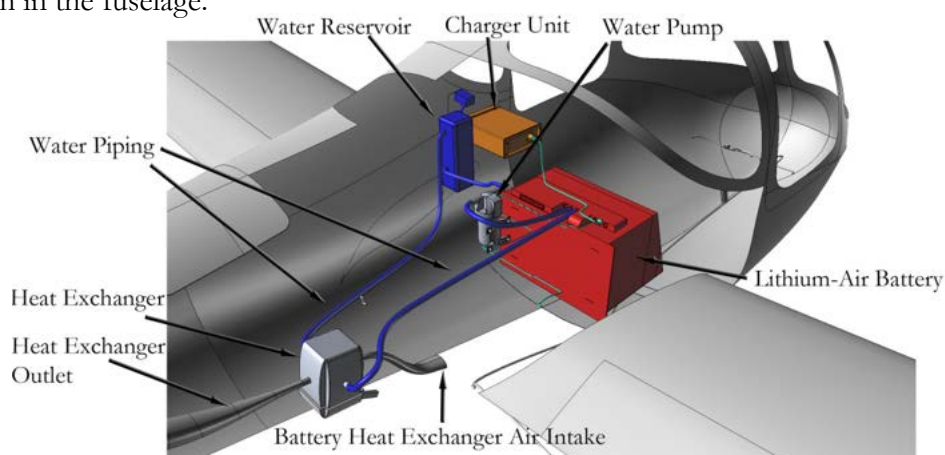


**Fig. 56 Battery cooling system**

The cooling air needed for the operation of the heat exchanger is obtained via a scoop installed on the lower fuselage with a frontal area of  $8.9 \text{ in.}^2$ . The scoop is offset by  $1.5 \text{ in.}$  from the lower fuselage surface into the airstream, to avoid ingesting the low-energy fuselage boundary layer. To ensure that no interference arises from the ingestion of the tire spray during wet runway ground operations, a tire spray pattern analysis was performed using methods outlined in ESDU Data Item 83042<sup>51</sup> to determine the maximum depth of water allowable. The maximum depth of contaminates on the surface of the runway, at which the operations of the cooling system of the aircraft may be impacted by the impinging tire spray released from the nose landing gear, was determined to be  $3/8''$ , corresponding to a side spray elevation angle and a plan view angle of  $18^\circ$  each. Figure 57 presents the tire spray pattern at the maximum contaminate depth.

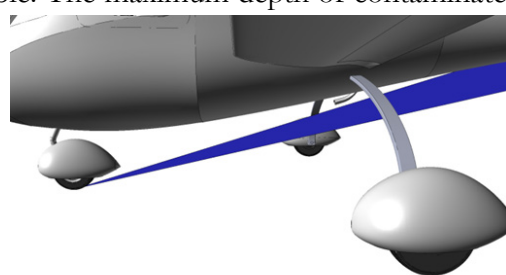
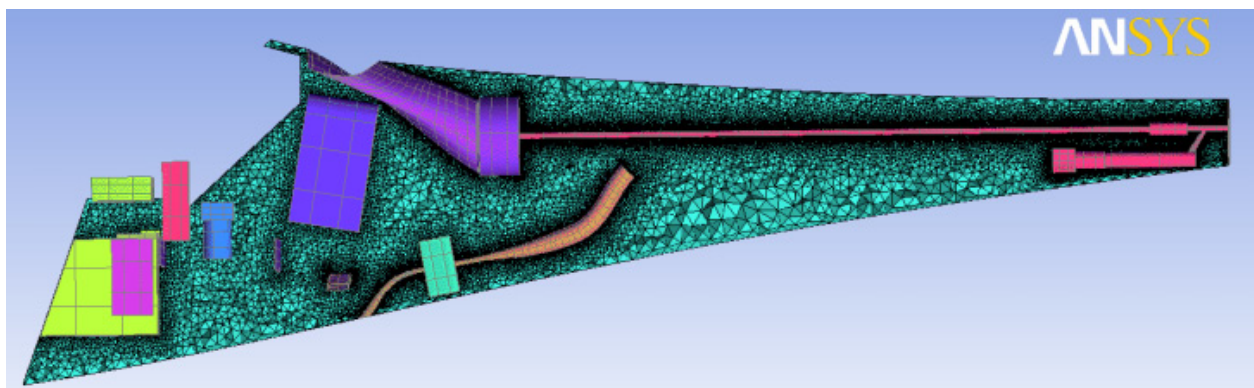


**Fig. 57 Tire spray**

The motor is cooled by air that is obtained via a large S-duct routed from the upper fuselage. The heated air flows from the motor through the tail cone, exiting the aircraft at the base of the fuselage assisted by the operation of the propeller.

### 10.2 CFD Verifications

Given the complexity of the arrangement of the heat-producing systems inside the fuselage, a numerical simulation was required in order to obtain accurate predictions of temperature at various locations of the fuselage. To achieve this, the geometry of the aft fuselage, including all of the systems, mid wingbox, and the cargo area was used to create an unstructured volume mesh in *ANSYS ICEM* environment. Figure 58 presents a view of the analysis domain.



Basic thermal loads were applied to the model by either determining the heat generation through boundary conditions or, in rare cases, steady-state temperature and thermal conductivity. Mass flows were applied through the air inlets and an operating pressure was defined for the fuselage tail cone outlet, which was obtained from the propeller analysis presented previously in Sec.

## 8.2. Table 9 presents a summary of the assumptions applied to the thermal model.

The analysis was repeated for two thermal cases; one during cruise at ISA conditions at 10,000' and the other at 500' at ISA+23.5°C (100 °F) while all systems are performing at their maximum allowable temperature. Results were post-processed to ensure that at no place in the fuselage the temperature exceeds the maximum allowable operating temperature of any of the components and the airframe. A summary of the results of the numerical thermal simulation is presented on the mechanical systems foldout.

**Table 9 CFD assumptions applied to the thermal model to numerically analyze the heat generated by exothermic systems inside the fuselage**

| Hot Day Approach: ISA +23.5 °C @ 500 ft |                           |       |                       |
|---|---------------------------|-------|-----------------------|
| Component                               | Boundary Condition        | Value | Units                 |
| Battery                                 | Static Temperature        | 75.0  | °C                    |
| Cargo Area                              | Adiabatic                 | ----  | ----                  |
| Charger                                 | Adiabatic                 | ----  | ----                  |
| DC/DC Converter                         | Heat Flux                 | 492.7 | W/m <sup>2</sup>      |
|   |                           | 150.0 | W                     |
| Fuselage                                | Heat Transfer Coefficient | 5.9   | W/(m <sup>2</sup> ·K) |
|   |                           | 37.9  | °C                    |
| Heat Exchanger                          | Static Temperature        | 47.1  | °C                    |
| Heat Exchanger Exhaust                  | Heat Transfer Coefficient | 13.0  | W/(m <sup>2</sup> ·K) |
|   |                           | 56.4  | °C                    |
| Heat Exchanger Inlet                    | Mass Flow                 | 0.2   | kg/s                  |
|   |                           | 56.4  | °C                    |
| Heat Exchanger Intake                   | Heat Transfer Coefficient | 5.9   | W/(m <sup>2</sup> ·K) |
|   |                           | 37.9  | °C                    |
| Landing Gear Beam                       | Adiabatic                 | ----  | ----                  |
| Motor                                   | Heat Transfer Coefficient | 15.5  | W/(m <sup>2</sup> ·K) |
|   |                           | 38.9  | °C                    |
| Motor Inlet                             | Mass Flow                 | 1.1   | kg/s                  |
|   |                           | 38.9  | °C                    |
| Outlet                                  | Relative Static Pressure  | -32.4 | Pa                    |
| Parachute Pack                          | Adiabatic                 | ----  | ----                  |
| Power Controller                        | Heat Flux                 | 109.4 | W/m <sup>2</sup>      |
|   |                           | 246.0 | W                     |
| Coolant Pump                            | Heat Flux                 | 570.4 | W/m <sup>2</sup>      |
|   |                           | 51.8  | W                     |
| Coolant Reservoir                       | Adiabatic                 | ----  | ----                  |
| Propeller Shaft                         | Adiabatic                 | ----  | ----                  |
| Spars                                   | Adiabatic                 | ----  | ----                  |

| Cruise @ 10,000 ft     |                           |       |                       |
|------------------------|---------------------------|-------|-----------------------|
| Component              | Boundary Condition        | Value | Units                 |
| Battery                | Static Temperature        | 50.0  | °C                    |
| Cargo Area             | Adiabatic                 | ----  | ----                  |
| Charger                | Adiabatic                 | ----  | ----                  |
| DC/DC Converter        | Heat Flux                 | 492.7 | W/m <sup>2</sup>      |
|                        |                           | 150.0 | W                     |
| Fuselage               | Heat Transfer Coefficient | 7.5   | W/(m <sup>2</sup> ·K) |
|                        |                           | -2.3  | °C                    |
| Heat Exchanger         | Static Temperature        | 4.2   | °C                    |
| Heat Exchanger Exhaust | Heat Transfer Coefficient | 13.2  | W/(m <sup>2</sup> ·K) |
|                        |                           | 10.6  | °C                    |
| Heat Exchanger Inlet   | Mass Flow                 | 0.3   | kg/s                  |
|                        |                           | 10.6  | °C                    |
| Heat Exchanger Intake  | Heat Transfer Coefficient | 7.5   | W/(m <sup>2</sup> ·K) |
|                        |                           | -2.3  | °C                    |
| Landing Gear Beam      | Adiabatic                 | ----  | ----                  |
| Motor                  | Heat Transfer Coefficient | 16.2  | W/(m <sup>2</sup> ·K) |
|                        |                           | -1.5  | °C                    |
| Motor Inlet            | Mass Flow                 | 1.6   | kg/s                  |
|                        |                           | -1.5  | °C                    |
| Outlet                 | Relative Static Pressure  | -83.2 | Pa                    |
| Parachute Pack         | Adiabatic                 | ----  | ----                  |
| Power Controller       | Heat Flux                 | 109.4 | W/m <sup>2</sup>      |
|                        |                           | 246.0 | W                     |
| Coolant Pump           | Heat Flux                 | 570.4 | W/m <sup>2</sup>      |
|                        |                           | 51.8  | W                     |
| Coolant Reservoir      | Adiabatic                 | ----  | ----                  |
| Propeller Shaft        | Adiabatic                 | ----  | ----                  |
| Spars                  | Adiabatic                 | ----  | ----                  |

### 10.3 Flight Control System

A mechanical reversible control system was implemented in Pandion given its simplicity and light weight compared to irreversible systems, e.g. fly-by-wire systems. The small hinge moments required to actuate the control surfaces, presented in Ch 12, make it possible to use a direct system in which no heavy hydraulic assistance is necessary. This reflects the trend experienced in LSAs of using reversible mechanical control systems. The pilot controls the aircraft in a conventional manner using a stick to control pitch and roll via elevators and ailerons, respectively. Pedals are used to provide yaw control through a fin rudder. A pulley mechanism transfers the control stick and pedal motions to the control surfaces as shown in Fig. 59. The mid-motor pusher configuration dictates the use of a driveshaft that can interfere with the routing of control cables to the empennage surfaces. As a result, a novel ring-shaped mechanism was used to generate the desired movement of the control surfaces while avoiding the driveshaft, as depicted in Fig. 60.

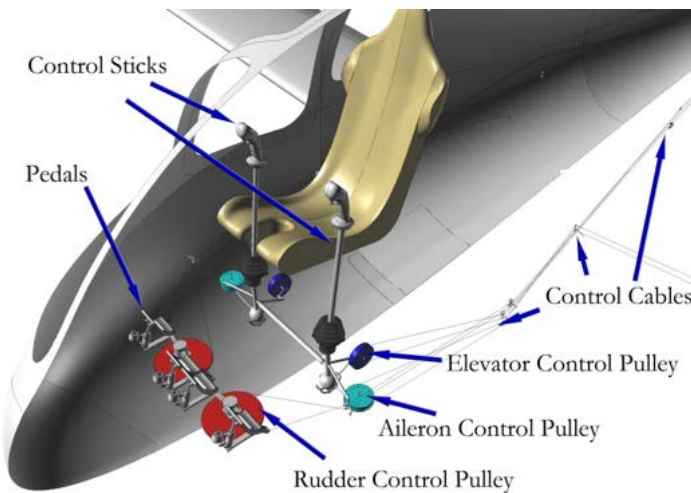


Fig. 59 Flight control system

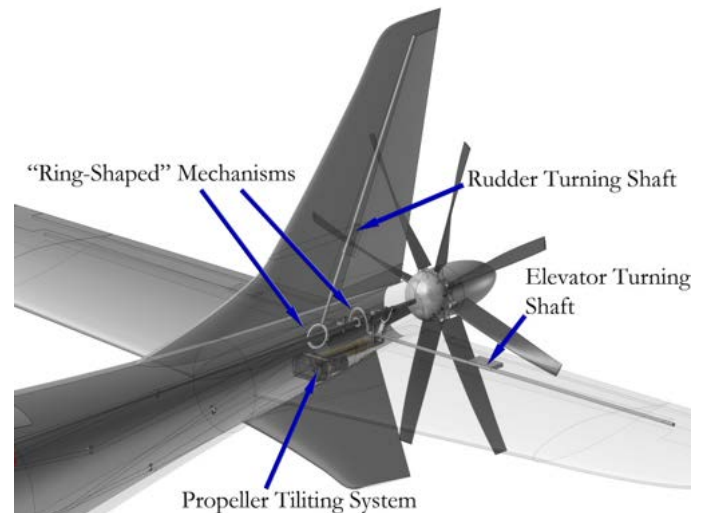


Fig. 60 Control cables and driveshaft

#### 10.4 Steering and Brakes

As mentioned in Sec. 5.9, pedals are used in Pandion to control steering and braking while on the ground. The steering system consists of a gear mechanism that transfers pedal rotational motion into the nose landing gear, allowing the aircraft to turn easily on the ground. The mechanism is designed so that the torque required from the pilot is smaller than the torque produced on the nose wheel, alleviating the required pedal force exerted by the pilot.

Pandion uses a closed circuit hydraulic differential braking system. This increases maneuverability on the ground by allowing the pilot to brake each wheel separately, providing a pivot point around which to rotate. This results in a minimum turn radius of 5.3', measured from the pivot point to the centerline of the airplane. The brakes are controlled by a hydraulic system that is activated by pressing on either the pilot or copilot pedals. A maximum hydraulic pressure of 500 *psi* was calculated to provide enough braking force to stop in 380'. A disc braking system with 4"-diameter rotors is installed in each main wheel assembly, providing braking power for the wheels. Figure 61 presents a view of the turn radius of Pandion. Figure 62 details the steering system and braking cylinders.

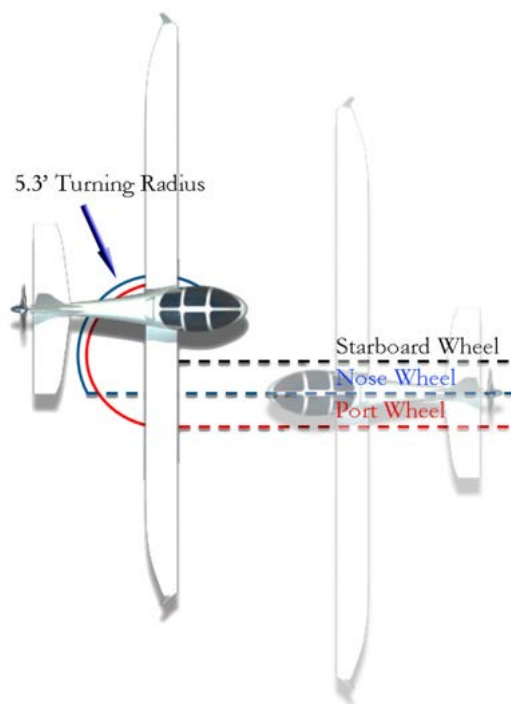


Fig. 61 Top View of turning radius

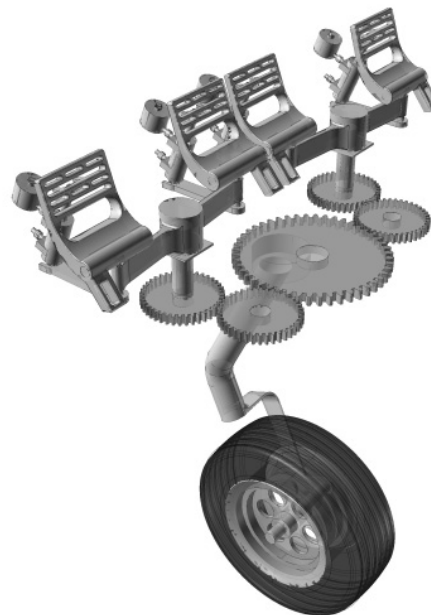
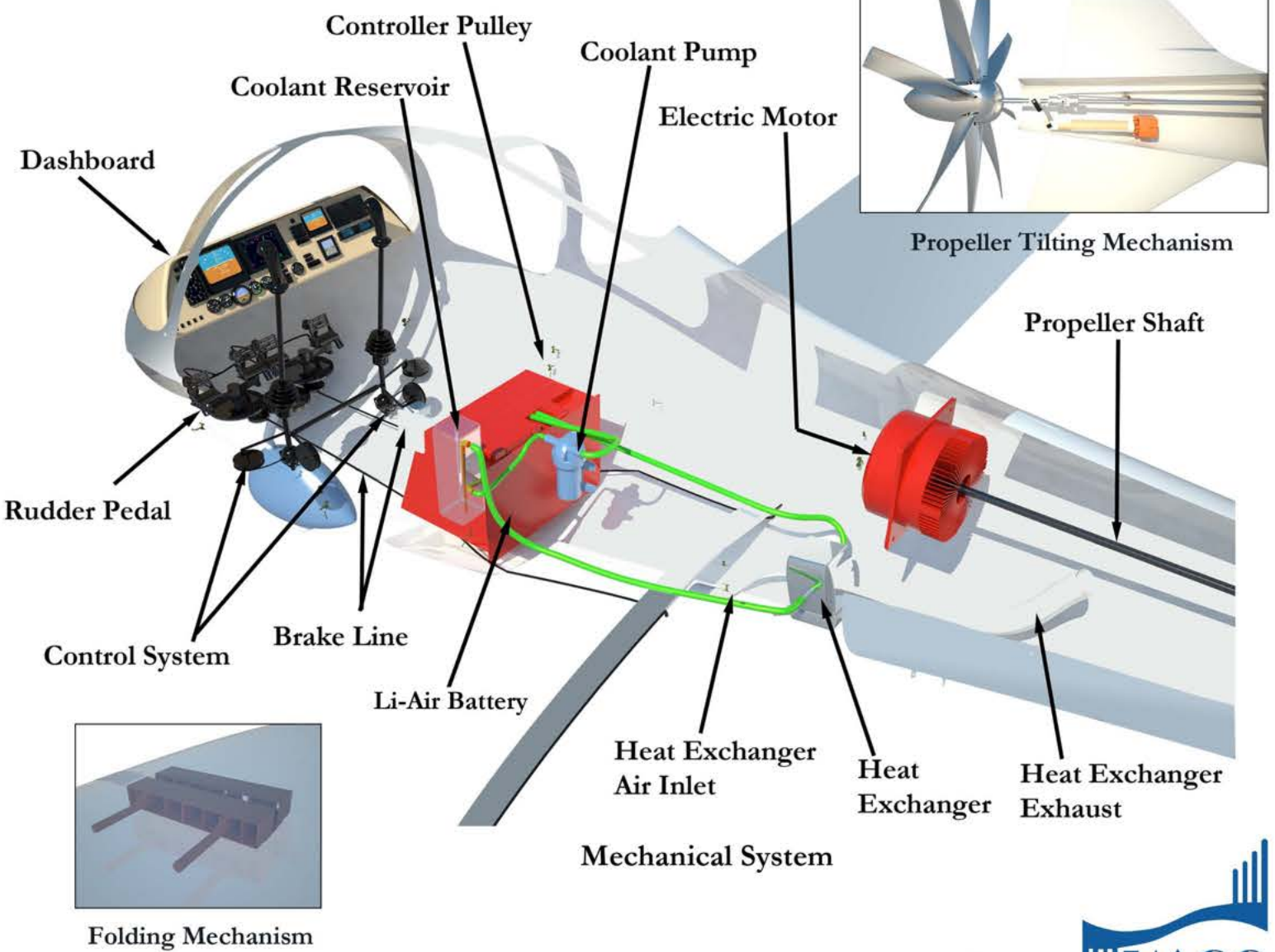
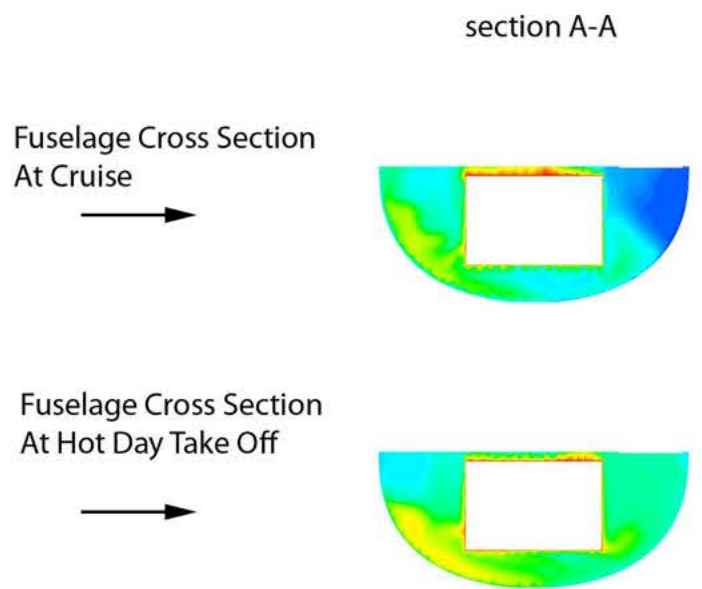
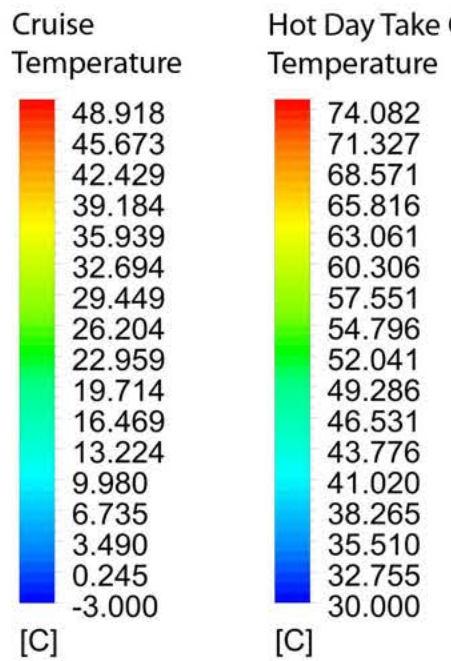
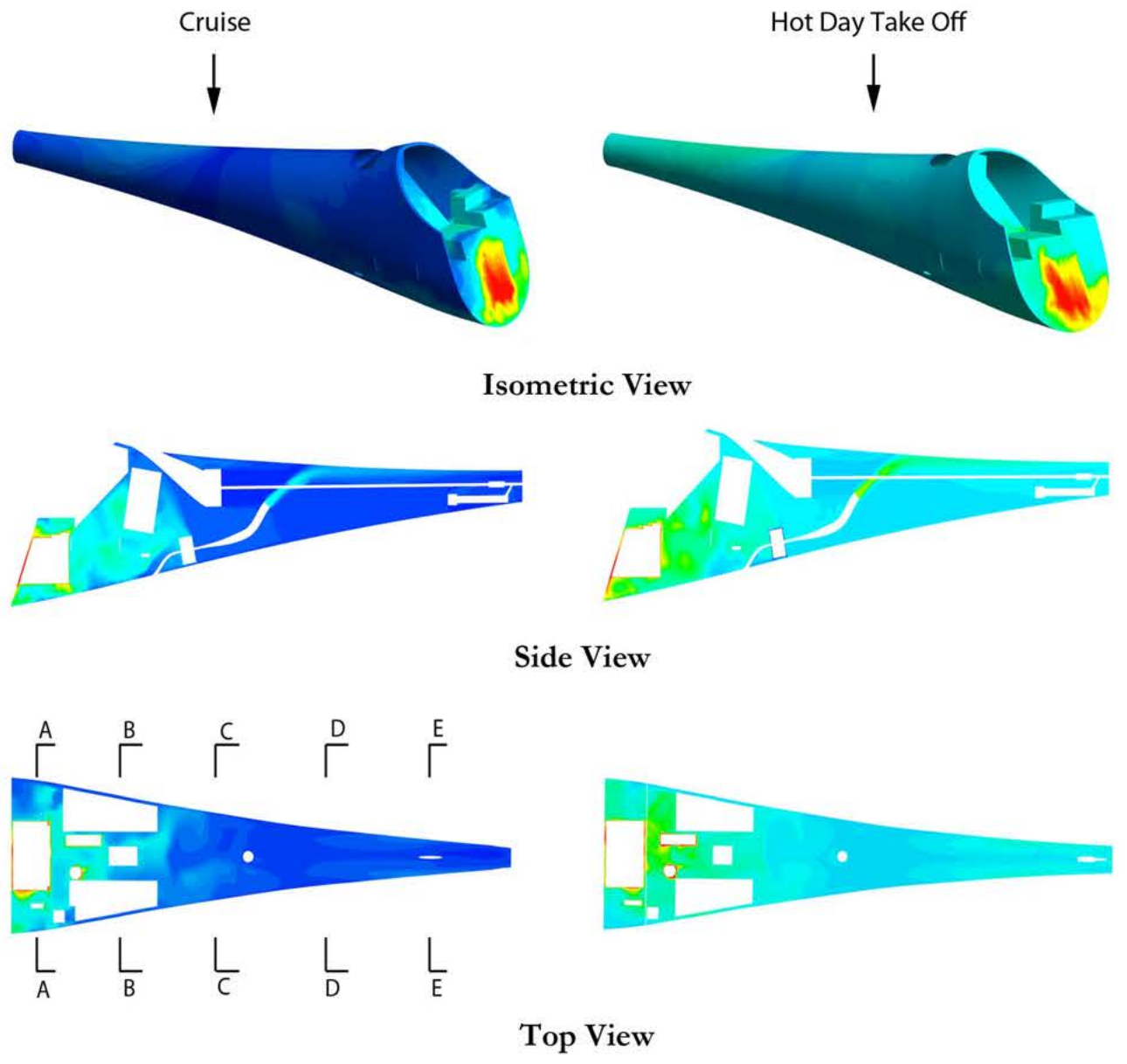


Fig. 62 Steering system



Pandion

## 11.0 Weight Justification & Analysis

### 11.1 Detailed Weight Analysis

A detailed weight analysis (Class II<sup>52</sup>) collaborates the methods established by *Cessna*<sup>53</sup>, the United States Air Force, *General Dynamics*, and *Torenbeek*<sup>54</sup> to accurately project the weight of the aircraft by verified methods based on geometry of the airplane<sup>55</sup>. However, the versatility and utility of these methods are not without faults. Specifically, these methods are overly general and are best applied to standard aircraft configurations and fall short when applied to aircraft with unconventional characteristics like Pandion, e.g. high aspect ratios, wing folding mechanisms, and heavy use of composite materials. For example, the *Cessna* weight methods predicted an overly large value for the wing weight that contradicted common sense. Due to this deficiency, UACC later pursued a Class III part-by-part weight estimation that broke down the design of Pandion into an appropriate custom weight estimation. Table 10 presents the results of the Class II weight estimation.

**Table 10 Summary of Class II weight estimation**

| Weight Component                 | Cessna Method<br>(lb.) | USAF<br>Method (lb.) | GD Method<br>(lb.) | Torenbeek<br>Method (lb.) | Average<br>Values (lb.) |
|----------------------------------|------------------------|----------------------|--------------------|---------------------------|-------------------------|
| Wing                             | 130                    | 123                  | -----              | 125                       | 126                     |
| Horizontal Tail                  | 28                     | 28                   | -----              | -----                     | 26                      |
| Vertical Tail                    | 10                     | 8                    | -----              | -----                     | 8                       |
| Fuselage                         | 122                    | 87                   | -----              | -----                     | 104                     |
| Nose Landing Gear                | 8                      | 1                    | -----              | 28                        | 14                      |
| Main Landing Gear                | 35                     | 2                    | -----              | 73                        | 43                      |
| <i>Structure</i>                 | <i>332</i>             | <i>249</i>           | -----              | <i>226</i>                | <i>323</i>              |
| Propeller                        | -----                  | -----                | 33                 | 33                        | 31                      |
| Propeller Motor                  | 136                    | -----                | -----              | 130                       | 66                      |
| Actuator                         | -----                  | -----                | -----              | -----                     | 14                      |
| Battery                          | -----                  | -----                | -----              | -----                     | 160                     |
| <i>Power Plant</i>               | <i>136</i>             | -----                | -----              | <i>163</i>                | <i>271</i>              |
| Air Induction System             | -----                  | -----                | -----              | 1                         | 1                       |
| Propulsion System                | -----                  | -----                | 25                 | 23                        | 23                      |
| Flight Control System            | 27                     | 108                  | -----              | 32                        | 47                      |
| Instruments/Avionics/Electronics | -----                  | -----                | -----              | 66                        | 43                      |
| Electrical System                | 43                     | 85                   | -----              | 39                        | 47                      |
| Air Cond./Press./Icing System    | -----                  | 33                   | -----              | 5                         | 15                      |
| Furnishings                      | 34                     | -----                | -----              | 31                        | 25                      |
| Cargo Handling Equipment         | -----                  | -----                | -----              | 0                         | 0                       |
| Other Items                      | -----                  | -----                | -----              | 5                         | 3                       |
| Parachute                        | -----                  | -----                | -----              | -----                     | 33                      |
| <i>Fixed Equipment</i>           | <i>103</i>             | <i>226</i>           | <i>25</i>          | <i>201</i>                | <i>236</i>              |
| Empty Weight                     | -----                  | -----                | -----              | -----                     | 829                     |
| <b>Maximum Takeoff Weight</b>    | -----                  | -----                | -----              | -----                     | <b>1,229</b>            |

## 11.2 Class III Weight Estimation

The UACC component-by-component weight analysis was done following the Class II weight analysis to ensure the integrity of the estimated weight of Pandion. UACC verified the structural integrity of major load-bearing structure using the methods discussed in Ch. 7 as well as FEA performed using *SolidWorks*. The verified geometry's weight was analyzed part-by-part considering the materials selected based on cost and structural needs. These methods recognize properties of advanced materials that otherwise are neglected in standard weight analysis. For instance, CFRP offers twice the strength at half the weight of 7075 T6 Aluminum. Furthermore, part-by-part analysis is not based on statistical data typically incorporated in empirical weight methods based off statistical data of aircraft over the last 40 years. Hence, the unique design aspects of Pandion including the 18.35 aspect ratio, folding wing mechanism, heat management system, and full electrical architecture must be accounted for individually. Figure 63 highlights the aforementioned heat management system, folding wing mechanism, and propeller tilting components analyzed separately as part-by-part weight estimation. The following foldout presents the results of the Class III weight estimations as illustrated, exploded weight groups

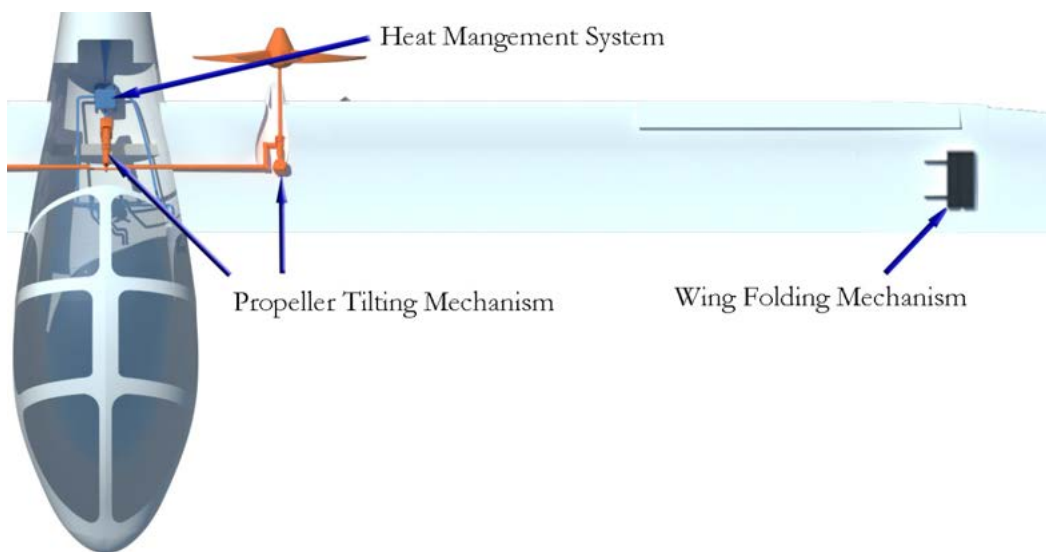


**Fig. 63 Highlights of the heat management system, folding wing mechanism, and propeller tilting components**



Pandion

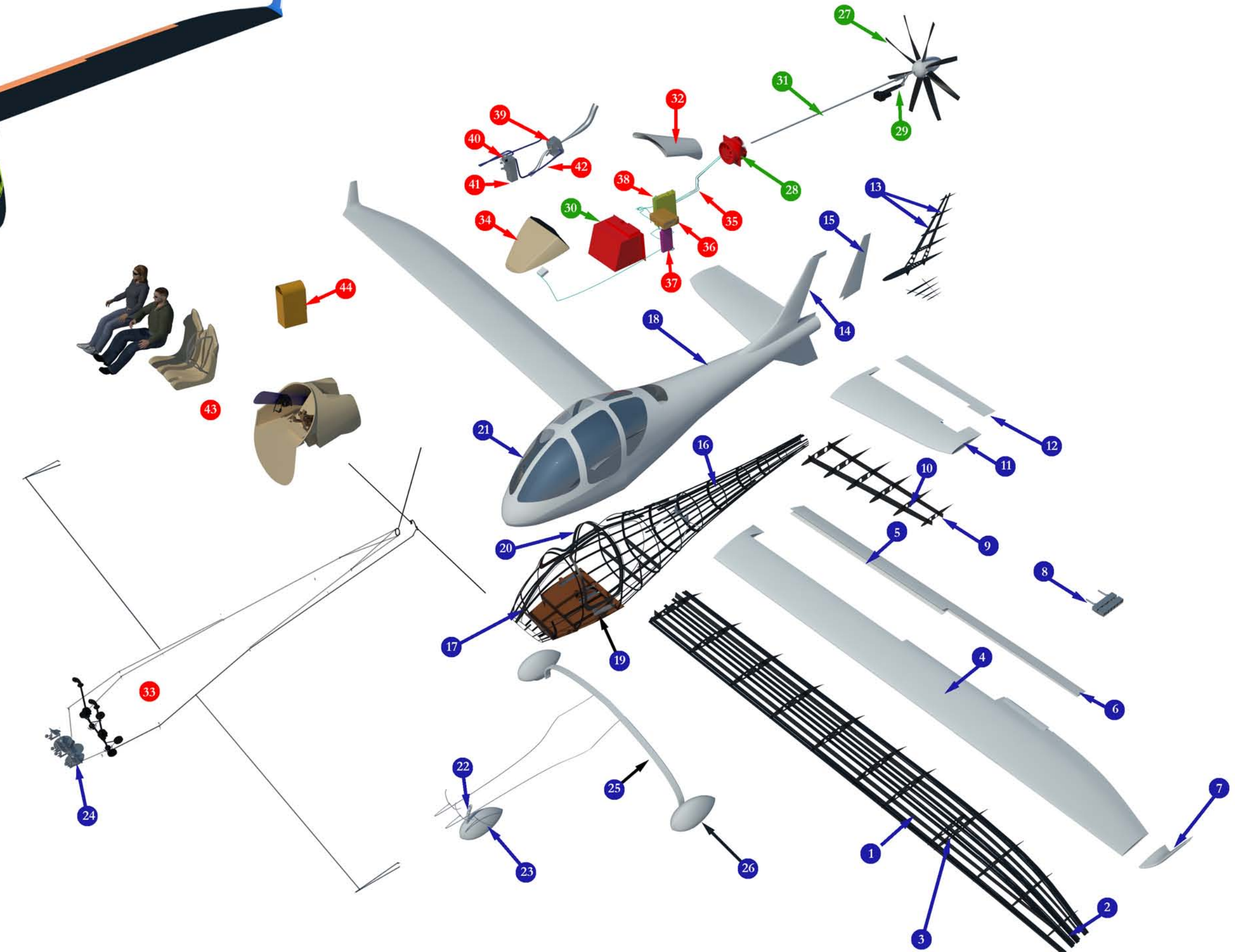
Material Distribution (top) and Exploded Weight Group Breakdown (bottom).  
The materials are shown part-by-part classified by their respective weight groups.  
For more detailed information, Please refer to the attached weight analysis tool.



32% ■ CFRP  
9% ■ CFRP Sandwich Panel  
6% ■ CFRP Honeycomb Panel  
33% ■ Aluminum  
16% ■ Steel  
2% ■ Fiberglass  
4% ■ Titanium

|                               |         |
|-------------------------------|---------|
| ① Wing Spars                  | 43 lb.  |
| ② Wing Longerons              | 19 lb.  |
| ③ Wing Ribs                   | 23 lb.  |
| ④ Wing Skin                   | 22 lb.  |
| ⑤ Flaps                       | 19 lb.  |
| ⑥ Aileron                     | 5 lb.   |
| ⑦ Winglets                    | 3 lb.   |
| ⑧ Wing Folding Mechanisms     | 12 lb.  |
| ⑨ Horizontal Tail Spars       | 14 lb.  |
| ⑩ Horizontal Tail Ribs        | 6 lb.   |
| ⑪ Horizontal Tail Skin        | 5 lb.   |
| ⑫ Elevator Surfaces           | 5 lb.   |
| ⑬ Vertical Tail Spars & Ribs  | 4 lb.   |
| ⑭ Vertical Tail Skin          | 2 lb.   |
| ⑮ Rudder                      | 1 lb.   |
| ⑯ Fuselage Frames             | 23 lb.  |
| ⑰ Fuselage Longerons          | 15 lb.  |
| ⑱ Fuselage Skin               | 15 lb.  |
| ⑲ Seat Railings               | 7 lb.   |
| ⑳ Cockpit Reinforcements      | 38 lb.  |
| ㉑ Transparencies              | 19 lb.  |
| ㉒ Landing Gear Strut          | 3 lb.   |
| ㉓ Tires & Rims                | 30 lb.  |
| ㉔ Steering Mechanism          | 5 lb.   |
| ㉕ Leaf Spring                 | 52 lb.  |
| ㉖ Landing Gear Fairings       | 9 lb.   |
| ㉗ Propeller                   | 23 lb.  |
| ㉘ Propeller Motor             | 66 lb.  |
| ㉙ Propeller Tilting Mechanism | 15 lb.  |
| ㉚ Li-Air Battery              | 160 lb. |
| ㉛ Propeller Shaft             | 18 lb.  |
| ㉜ Air Induction System        | 1 lb.   |
| ㉝ Control System              | 11 lb.  |
| ㉞ Avionics                    | 7 lb.   |
| ㉟ Wiring                      | 5 lb.   |
| ㉟ Charger                     | 4 lb.   |
| ㉟ DC-DC Converter             | 5 lb.   |
| ㉟ Motor Controller Unit       | 22 lb.  |
| ㉟ Heat Exchanger              | 6 lb.   |
| ㉟ Coolant Pump                | 4 lb.   |
| ㉟ Coolant                     | 10 lb.  |
| ㉟ Piping                      | 9 lb.   |
| ㉟ Furnishings                 | 25 lb.  |
| ㉟ Parachute Pack              | 33 lb.  |

● Structure  
■ Powerplant  
● Fixed Weight



#### 11.4 Center of Gravity Analysis

The center of gravity location was estimated based on the results of the Class III weight analysis and the locations of individual components. The defined location of the airplane empty weight is shown in Table 11, and the airplane's component CG's are located in the component CG side profile in Fig. 64. Tables 10 and 12 show a detailed summary of takeoff weight figures and moments of inertia, respectively.

Table 10 Detailed Takeoff Weight

|                   |           |
|-------------------|-----------|
| $W_{fix}$         | 164 lb.   |
| $W_{Structure}$   | 429 lb.   |
| $W_{PP}$          | 263 lb.   |
| $W_{PL}$          | 400 lb.   |
| $W_E$             | 851 lb.   |
| $W_{TO}$          | 1,229 lb. |
| $W_{TO,Extended}$ | 1,221 lb. |
| $W_{TO,Light}$    | 1,001     |

Table 11 Empty Weight CG

|          | Empty Weight | MTOW  | Extended | Light |
|----------|--------------|-------|----------|-------|
| $X_{CG}$ | 7.98'        | 7.07' | 7.08'    | 7.61' |
| $Y_{CG}$ | 0'           | 0'    | 0'       | 0'    |
| $Z_{CG}$ | 4.78'        | 4.85' | 4.81'    | 4.78' |

Table 12 Moment of Inertia

|            |     |                      |
|------------|-----|----------------------|
| $I_{xx_B}$ | 29  | slug-ft <sup>2</sup> |
| $I_{yy_B}$ | 498 | slug-ft <sup>2</sup> |
| $I_{zz_B}$ | 469 | slug-ft <sup>2</sup> |
| $I_{xz_B}$ | 52  | slug-ft <sup>2</sup> |

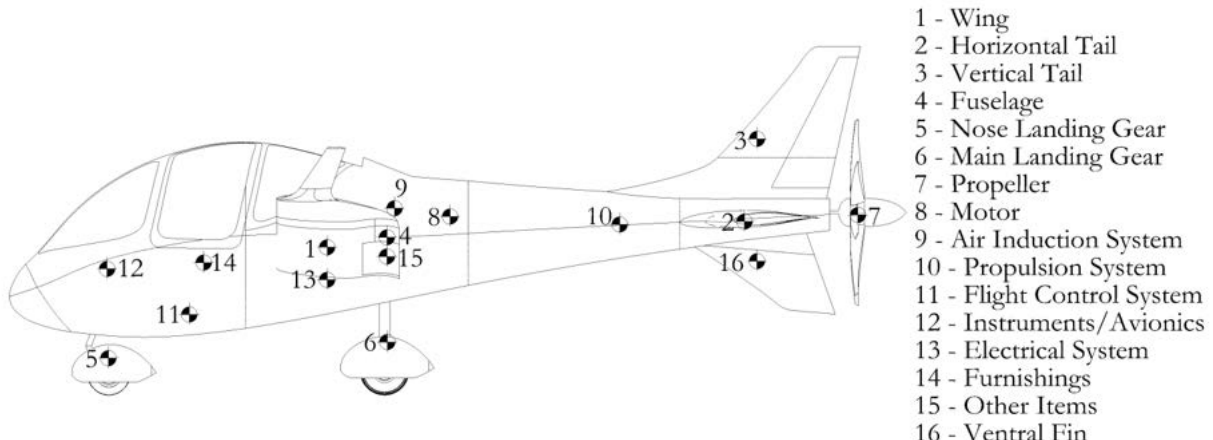


Figure 64 CG locations, side profile

## 12.0 Stability and Control

### 12.1 Loading Cases

As suggested by the RFP, the alternative loadings of the airplane were investigated by determining the CG location for three critical cases; a single light passenger (120 *lb.*) with no luggage, two light-heavy passengers (170 *lb.*) with luggage (60 *lb.*), and two heavy passengers (200 *lb.*) without luggage. Additionally, the option for trading one passenger for an additional battery was accommodated for. It was concluded after the analysis (as will be presented in following sections) that Pandion is capable of accommodating all loading cases required by the RFP with sufficient longitudinal static margin and negligible degrading of handling performance.

### 12.2 Balance, CG Travel, and Wing Location

Static stability of the configuration was achieved by performing a parametric study of the impact of the longitudinal location of the wing on the magnitude of static margin using the methods presented by *Roskam*<sup>56</sup>. Mass properties analysis of Pandion indicated that a CG travel range equivalent to 19.8% of mean aerodynamic chord of the aircraft is possible among all different loading cases dictated by the RFP. A minimum target positive stick free static margin of at least 20%<sup>57</sup> was selected for the mid-cruise segment of the flight to ensure the inherent static stability of the aircraft. The result of this parametric study can be seen in Fig. 65.

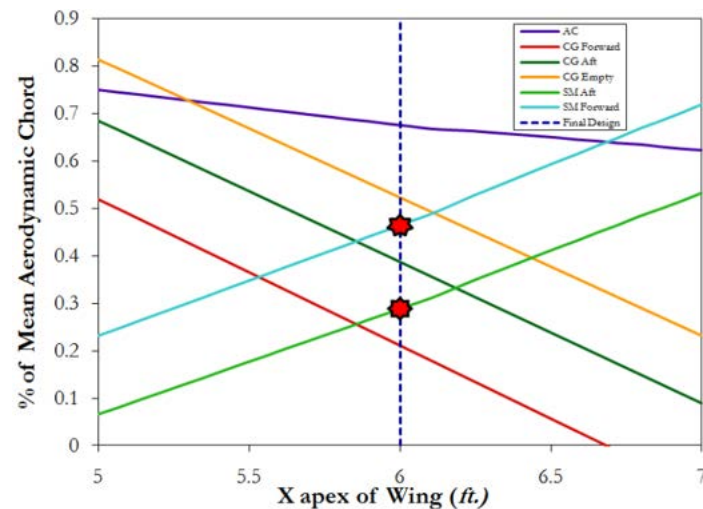


Fig. 65 Wing location trade study

UACC concluded that a longitudinal wing apex of 72" will provide sufficient positive static margin at forward and aft locations of the CG, therefore ensuring the maintenance of the static stability of the aircraft under all loading conditions.

### 12.3 Tail Sizing and Trim Diagram

The empennage of Pandion was sized to satisfy basic stability and control requirements set by MIL-F-8785<sup>58</sup> and recommended by Roskam<sup>59</sup> as well as being able to initiate the takeoff rotation. MIL-F-8785 recommends that in order to maintain static longitudinal stability, the air vehicle must possess negative values of  $C_{m_x}$  and  $C_{m_z}$  at all flight conditions. A horizontal tail area of  $42.2 \text{ ft}^2$ , capable of maintaining a  $C_{m_x}$  and  $C_{m_z}$  of at least  $-0.2 \text{ rad}^l$ , was selected by performing a parametric study that varied the area of a generic horizontal tail planform and then computed the corresponding  $C_{m_x}$  and  $C_{m_z}$  using methods presented by Roskam<sup>60</sup>. A trim diagram was generated assuming it is equipped with an elevator capable of deflecting  $\pm 20^\circ$  in order to verify the capacity of the airplane to maintain trim at all loading conditions. This trim diagram can be seen in Fig. 66.

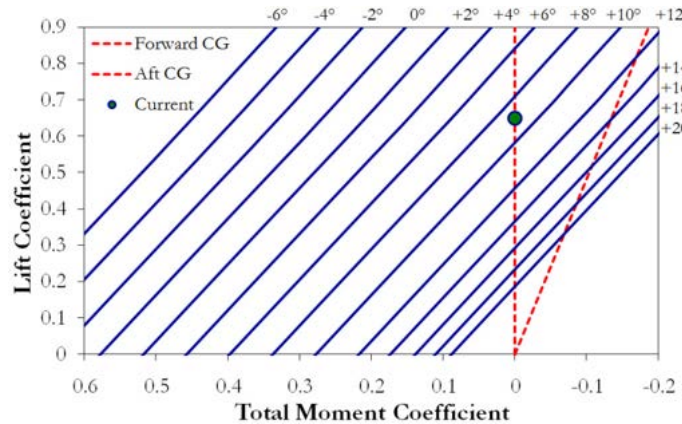


Fig. 66 Trim diagram with current cruise condition

### 12.4 Stability & Control Derivatives

MIL-F-8785<sup>61</sup> requires that every aircraft should have a neutral point located behind the most aft center of gravity in order to maintain static longitudinal stability in all flight conditions. The location of the aircraft's neutral point was determined using the method presented by Roskam<sup>62</sup>. A selection of the results with the load case of two 170 lb. passengers and 60 lb. of cargo is presented in Table 13. As it can be seen from this table, the magnitude of the static margin is always positive

indicating that the location of the center of gravity is always ahead of the aerodynamic center of the aircraft in all critical flight segments.

**Table 13. Location of CG, aerodynamic center, and corresponding free stick static margin at takeoff, cruise, and landing conditions**

| Segment        | Takeoff | Cruise | Landing |
|----------------|---------|--------|---------|
| $\bar{x}_{cg}$ | 0.2165  | 0.2165 | 0.2165  |
| $\bar{x}_{ac}$ | 0.7002  | 0.6603 | 0.71    |
| $SM_{free}$    | 49.74%  | 38%    | 51.03%  |

In order for the aircraft to remain statically stable, the pitching moment coefficient due to the angle of attack ( $C_{m_a}$ ), and pitching moment coefficient due to angle of attack rate derivative ( $C_{m_{\dot{a}}}$ ) both should be negative. In order to verify the lateral and directional static stability of the aircraft, yawing-moment coefficient-due-to-sideslip derivatives ( $C_{n_{\beta}}$ ), and rolling-moment-coefficient-due-to-sideslip derivatives ( $C_{l_{\beta}}$ ) were computed. As *Roskam* suggests, to maintain lateral and direction static stability,  $C_{n_{\beta}}$ , should be positive while  $C_{l_{\beta}}$  should have a negative value. These derivatives were computed using methods presented by *Roskam*<sup>76</sup> and can be seen in Table 14.

**Table 14. Important longitudinal and lateral-directional static stability derivatives**

| Segment                   | Takeoff | Cruise  | Landing |
|---------------------------|---------|---------|---------|
| $C_{m_a} [rad^l]$         | -3.80   | -3.09   | -3.80   |
| $C_{m_{\dot{a}}} [rad^l]$ | -8.42   | -7.08   | -8.48   |
| $C_{n_{\beta}} [rad^l]$   | 0.0264  | 0.0238  | 0.0255  |
| $C_{l_{\beta}} [rad^l]$   | -0.0434 | -0.0554 | -0.0362 |

## 12.5 Aileron Sizing

Due to the acceptability and availability of FAR-23 standards for light general aviation aircraft, guidelines suggested by this code are used to estimate the required size of the ailerons for the aircraft. To perform this estimation, a theoretical approach presented by *Roskam*<sup>63</sup> was used. In the interests of brevity, this method is not presented in this proposal. The goal of achieving “level I” rolling qualities in the takeoff flight condition was pursued using the rolling time constants suggested by FAR-23. Assuming an individual aileron has a  $C_a/C_w$  equal to 20% starting at 47% of the half-span (following the flap), the outboard station of the aileron was calculated to be located at 76% of the half span. This aileron geometry was validated later during the analysis of the lateral directional flying qualities by fulfilling the rolling requirements defined in FAR-23.

## 12.6 Dynamic Stability

The dynamic stability analysis for Pandion were performed using *AAA*’s flight dynamics modules and the results for the most important flight segments, specifically takeoff, cruise, and landing, are presented herein. Handling quality analyses performed using the *AAA* package indicates that Pandion is capable of achieving Level I and Level II flight handling characteristics in all segments of flight. Results are confirming the satisfaction of the regulations presented by FAR-23 and MIL- F-8785 for light airplanes with regard to the time constants and damping ratios, in particular those pertaining to phugoid and short period oscillation modes.

In order to verify longitudinal dynamic stability, dynamic stability derivatives were evaluated along the  $x$ ,  $y$  and  $z$  axes to determine the transfer functions and characteristic equations for Pandion. The methods applied were obtained from USAF Stability and Control DATCOM<sup>64</sup>. Natural frequencies and damping ratios for short period oscillations, and phugoid modes, were calculated based on the methods presented by *Roskam*<sup>65</sup>. Values of short period and long period natural frequencies and damping ratios can be seen in Table 15 for takeoff, cruise, and landing conditions.

**Table 15. Dynamic longitudinal stability characteristics for various flight conditions**

| Flight segment:                                | Takeoff | Cruise | Landing |
|--|---------|--------|---------|
| $T_{\frac{1}{2}p}$ sec.                        | 19.6    | 65.4   | 22.8    |
| $Level_p$                                      | I       | II     | I       |
| $Level_{\xi_{SP}}$                             | II      | II     | II      |
| $\omega_{n,S.P}$ (rad/sec <sup>-1</sup> )      | 5.61    | 7.37   | 4.98    |
| $\omega_{n_{P,long}}$ (rad/sec <sup>-1</sup> ) | 0.75    | 0.34   | 0.75    |
| $\zeta_{SP}$                                   | 0.64    | 0.57   | 0.65    |
| $\zeta_{P,long}$                               | 0.05    | 0.03   | 0.04    |

## 12.7 Propeller Tilting

Analysis was performed to quantify the effects of the propeller tilting system on the pitch down moment of the airplane using methods presented by Roskam<sup>66</sup>. The moment coefficient due to thrust ( $C_{m_T}$ ) was computed for various flight conditions and can be seen in Table 16.

**Table 16 Moment coefficient due to prop-tilting at all flight segments.**

| Flight segment: | Takeoff | Climb   | Cruise  | Descent | Loiter  | Descent 2 | Landing |
|-----------------|---------|---------|---------|---------|---------|-----------|---------|
| $C_{m_T(PT)}$   | -0.204  | -0.1857 | -0.0511 | -0.0215 | -0.0670 | -0.0338   | -0.2374 |

It was concluded that an additional pitch down moment of 411 *lb.-ft.* and 327 *lb.-ft.* can be generated during takeoff and landing, respectively, which is equivalent to an average increase in horizontal tail area of 4 *ft.<sup>2</sup>*. A flight simulation was performed using *X-Plane 9* to validate the capacity of the prop-tilting mechanism to help recovery from low-altitude deep stall situations.

## 13.0 Performance

### 13.1 Performance of Installed Powerplant

Based on the methods presented by *Roskam*<sup>67</sup>, the installed power characteristics of the propulsion system were modeled for the purposes of determining the performance of the aircraft. The properties of the custom-designed propeller, presented in Sec. 8.2, were used in this analysis. The results of the analysis can be seen in Table 17.

**Table 17 Installed power characteristics of propulsion system**

| Flight segment:                              | Takeoff | Climb  | Cruise | Descent | Loiter | Descent 2 | Landing |
|--|---------|--------|--------|---------|--------|-----------|---------|
| P <sub>avail, shaft</sub> ( $b\dot{p}$ )     | 14.2    | 55.0   | 28.3   | 4.0     | 15.6   | 4.0       | 17.6    |
| P <sub>avail, propeller</sub> ( $b\dot{p}$ ) | 10.5    | 38.6   | 24.9   | 3.4     | 12.6   | 3.4       | 13.3    |
| Advance Ratio                                | 0.4     | 0.55   | 1      | 0.55    | 0.55   | 0.55      | 0.45    |
| $C_p$  | 0.0229  | 0.0942 | 0.0522 | 0.0069  | 0.0267 | 0.0069    | 0.029   |
| $\eta_p$                                     | 0.74    | 0.70   | 0.88   | 0.86    | 0.81   | 0.86      | 0.75    |

### 13.2 Takeoff Performance

The required takeoff field length for Pandion is determined by applying relations presented by ESDU Data Item 85029<sup>68</sup> and considering the ground effect on generated lift and drag<sup>69</sup>. It is assumed that the aircraft uses the previously sized flaps during takeoff without assistance from leading edge high lift devices, making the maximum lift coefficient ( $C_{L_{max}} = 2.2$ ) attainable. The average kinetic friction coefficient was computed using the data presented by *Roskam*<sup>70</sup> to be 0.02, assuming a conventional tarmac mix, as used in the United States.

The takeoff trajectory was computed for normal takeoff and can be seen in Fig. 67. Assumptions regarding takeoff performance computations and the results of this analysis are presented in Tables 17 and 18.

**Table 17 Takeoff Condition**

|                  |        |
|------------------|--------|
| $C_{L_{max,TO}}$ | 2.2    |
| $C_{DO,TO}$      | 0.1791 |
| $L/D_{TO}$       | 12     |
| $\Pi_{TO}$       | 0.95   |

**Table 18 Takeoff Performance**

|            |         |
|------------|---------|
| $V_{LOF}$  | 41 kts. |
| $S_{TO}$   | 1500'   |
| $S_{TO,G}$ | 612'    |

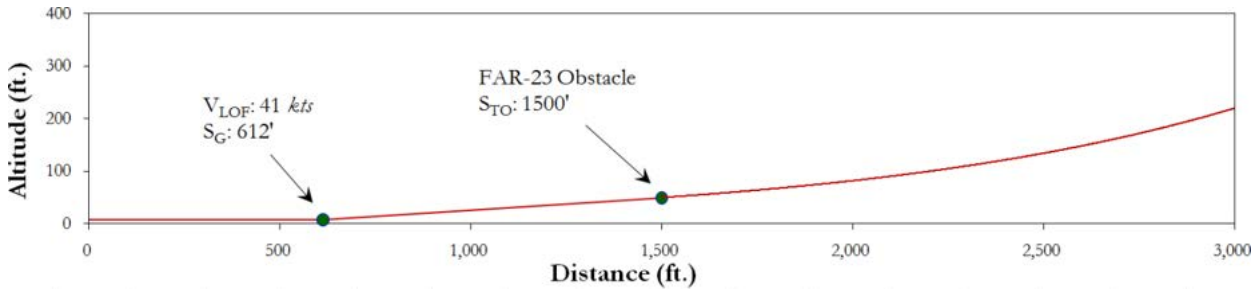
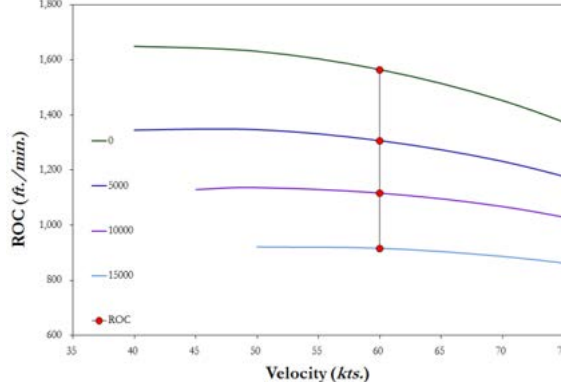


**Fig. 67 Takeoff trajectory**

### 13.3 Climb Performance

In order to calculate the maximum rate of climb for Pandion, and in general, the climb performance of the aircraft relations presented by *Roskam*<sup>71</sup> were used. The rate of climb was plotted versus velocity to capture the performance of the aircraft in climb at various altitudes. This graph is shown in Fig. 68. Analyses were performed in order to determine the time required to climb from sea level to 9,500' based on the mission profile presented by the RFP. The results and assumptions for this analysis are presented in Table 17.

**Table 17 Results of climb performance**



|                      |           |
|----------------------|-----------|
| $\Delta_h$           | 9,500'    |
| $\alpha$             | 0.56°     |
| R/C                  | 625 fpm   |
| CGR                  | 0.1       |
| $P_{SpExPwr}$        | 743 fpm   |
| $t(1 \rightarrow 3)$ | 15.2 min. |

**Fig. 68 Climb performance**

### 13.4 Maximum Cruise Speed

An analysis was performed of the required and available power at cruise for Pandion. From this analysis it was determined that the maximum possible cruise speed at 9,500' is 161 *kts*. At this velocity, the required power to overcome drag equals the maximum power of the motor. However, the flutter characteristics, presented in Sec. 7.5, and the structural design of Pandion dictate that the aircraft may not exceed 147 *kts*. This requires an electronic de-rating system to be installed on Pandion, which would impose a nominal rating of 75% on the maximum power available of the electric motor, at cruise.

### 13.5 Maneuvering Performance

The airplane's instantaneous and sustained pull-up/push-over performance are calculated based on the methods presented by *Roskam*<sup>72</sup>. The analysis was performed to calculate the minimum turn radius, maximum pull-up load factor, and turn rate by plotting the power available, power required, and load factors versus speed. Maximum maneuver capabilities are reached when the amount of excess power is maximized at an airspeed of 117 *kts*. Results of the maneuverability analysis at cruise condition are summarized in Table 17.

**Table. 17 Pull-up and Instantaneous turn performance**

|                      |                        |
|----------------------|------------------------|
| V <sub>m</sub>       | 80 <i>kts.</i>         |
| Q <sub>1</sub>       | 0.2727 <i>rad./sec</i> |
| n <sub>pull-up</sub> | 2.15 <i>g</i>          |
| φ                    | 62.3°                  |
| Turn Rate            | 0.45 <i>rad./sec.</i>  |
| R <sub>turn</sub>    | 300'                   |
| n <sub>turn</sub>    | 2.15 <i>g</i>          |

### 13.6 Endurance

The endurance of the aircraft was computed by estimating the amount of energy required to perform the mission profile presented in Sec. 2.3. A similar method to that presented in Sec. 2.3 was utilized to estimate the endurance of the aircraft. However, the most accurate available drag coefficients, obtained from detailed aerodynamic analysis presented in Sec. 6.6, were substituted in place of the preliminary drag coefficients. A summary of this updated energy budget can be seen in Table 18.

**Table 18 Finalized energy budget, updated from detailed aerodynamic analysis**

| Flight Condition | Altitude<br>( <i>ft</i> ) | Speed<br>( <i>kts.</i> ) | Detailed C <sub>D</sub> | Duration<br>( <i>min</i> ) | Distance<br>Travelled<br>( <i>nmi</i> ) | Mechanical<br>Work<br>Performed<br>( <i>Whr</i> ) | Energy<br>Fraction |
|------------------|---------------------------|--------------------------|-------------------------|----------------------------|---|---|--------------------|
| 1. Takeoff       | 0                         | 45                       | 0.1491                  | 10                         | 8                                       | 2,300   | 8 %                |
| 2. Typical Climb | 4,750                     | 60                       | 0.0658                  | 15                         | 15                                      | 8,000   | 27 %               |
| 3. Cruise        | 9,500                     | 80                       | 0.0219                  | 100                        | 135                                     | 14,535  | 48 %               |
| 4. Descent       | 6,000                     | 60                       | 0.0373                  | 7                          | 7                                       | 280   | 1 %                |
| 5. Loiter        | 2,500                     | 60                       | 0.0359                  | 30                         | 30                                      | 3,700   | 12 %               |
| 6. Descent       | 1,250                     | 60                       | 0.0333                  | 3                          | 3                                       | 145   | <1 %               |
| 7. Landing       | 0                         | 40                       | 0.2030                  | 3                          | 2                                       | 1,040   | 3 %                |
| <b>TOTAL</b>     | ----                      | ----                     | ----                    | <b>168</b>                 | <b>235</b>                              | <b>30,000</b>                                     | <b>100 %</b>       |

It was observed that an endurance of 2.8 *hrs.*, corresponding to a 235 *nmi.* range, can be achieved with a 67 *kW-br* battery onboard. This endurance is extendable to 6.2 *hrs.* with the use of an extended range battery pack (ERP) that may be installed in place of the passenger, as requested by the RFP and discussed in Sec. 14.4.

### 13.7 Landing Trajectory

The method presented by ESDU Data Items 91032<sup>73</sup>, 92020<sup>74</sup>, and EG6/4<sup>75</sup> was used to estimate the landing distance for the aircraft assuming a Maximum Landing Weight (MLW) of 1,221 *lb.* MLW is defined as the empty weight of the aircraft plus two 170-*lb.* passengers and 60 *lb.* of luggage onboard. The ground effects are taken into account in this analysis, for which the results are presented in detail in Table 19. Figure 69 presents the results of the simulation of the landing trajectory of the aircraft.

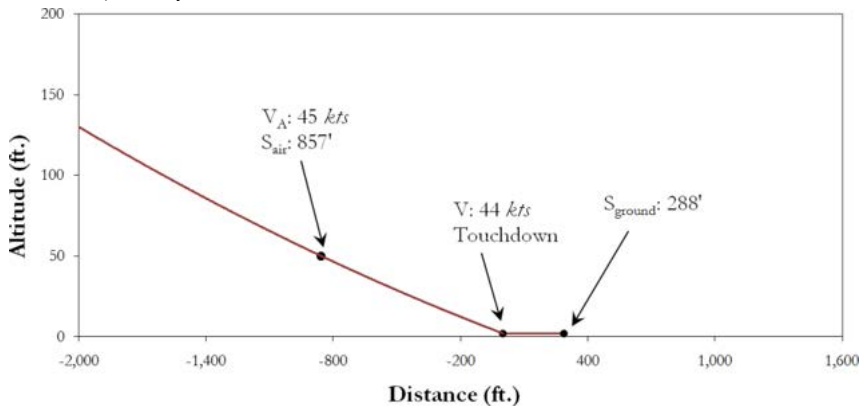


Fig. 69 Landing Trajectory

Table 19 Landing performance

|                |                |
|----------------|----------------|
| $\Delta_n$     | 0.1            |
| $\bar{\gamma}$ | 3.43°          |
| $V_{S_L}$      | 35 <i>kts.</i> |
| $V_A$          | 45 <i>kts.</i> |
| $S_{air}$      | 857'           |
| $S_{LG}$       | 288'           |
| $S_L$          | 1145'          |

13.8 Stall Speed  
The stall speed is evaluated using the equations presented by Roskam<sup>76</sup>. From these equations, the maximum lift coefficient (including flap effects) of the aircraft was calculated as high as 2.2, to be achieved at 7° angle of attack. Additionally, the maximum clean lift coefficient in flight conditions not using flaps was determined as 1.5. From the  $C_{L_{max}}$ 's, the stall speeds at all flight conditions were able to be calculated. Table 20 presents a summary of the stall speed performance of the aircraft. Pandion is equipped with a prop-tilting mechanism that allows production of enormous amounts of nose down pitching moment, suitable for recovery from deep stalls.

**Table 20. Stall speeds**

| Flight segment:       | Takeoff | Climb | Cruise | Descent | Loiter | Descent | Landing |
|-----------------------|---------|-------|--------|---------|--------|---------|---------|
| V <sub>s</sub> [kts.] | 35      | 38    | 54     | 51      | 48     | 47      | 35      |

### 13.9 Noise Assessment

Cabin noise is of crucial interest in determining user comfort level. Post analysis evaluation of readily calculable factors contributing to overall cabin noise level yields the conclusion that the most significant factor in the noise level is the propeller noise. All other noise is at least an order of magnitude smaller by comparison, and under logarithmic addition, will give a small increase on top of the noise level given by the propeller.

We therefore look to compute the noise level of the propeller measured in-cabin. Using a purely empirical method developed by *Marte et al.*<sup>77</sup>, the noise due to the propeller (without intervening material such as a windshield) at cruise is computed to be approximately 118 dB.

Constructing the windshield with a sound attenuating glass epoxy of approximately 6mm thickness results in an average of 31 dB attenuation across most of the audible frequency range. This results in an effective sound level of approximately 87 dB. This estimate is said to be accurate to -5 to +9 dB and is substantially quieter than present day SLSA's, very similar to the noise levels experienced by commercial jetliner passengers.

Using a far-field method developed by *Marte et al.*, the following plots of far field noise were created. Each is relevant to a specific noise requirement specifying a location of measurement for take-off, approach, and sideline noise. Based on a set of simulated measurements taken at these locations (taking both distance and angle of inclination with respect to prop axis during the three critical regimes), the maximum relevant dB levels were calculated at takeoff, approach, and sideline, as presented in Table 21

**Table 21. Summary of Noise results**

|              | Takeoff | Approach | Sideline |
|--------------|---------|----------|----------|
| Max dB level | 29 dB   | 44 dB    | 33 dB    |

## 14.0 Maintenance & Operations

### 14.1 T-Hangar & Storage

As requested by the RFP, Pandion was designed to be stored in a T-hangar. Such storage imposed limitations on the span of the wings, the horizontal tail, and the maximum height of the aircraft. As the design space analysis presented in Sec. 6.2 demanded a relatively high wing span of 50', wing folding was required in order to fit inside a 40' wide T-hanger. This was accomplished through a multi-lug folding mechanism, separating the outboard wingbox from the inboard wingbox, and secured on the surfaces of the front and rear spars of the wingboxes, as well as the upper and lower skin panels. The folding is operated using electro-motors equipped with a worm-gearred mechanism that directs the folding between the direction of the dihedral of the wing and the direction perpendicular to the ground. The folding mechanism is secured before taxi and takeoff by electrically operated latch pins that are inserted into the connector plate installed on both sides of the folding mechanism. Figure 70 presents a structural view of the locking mechanism.

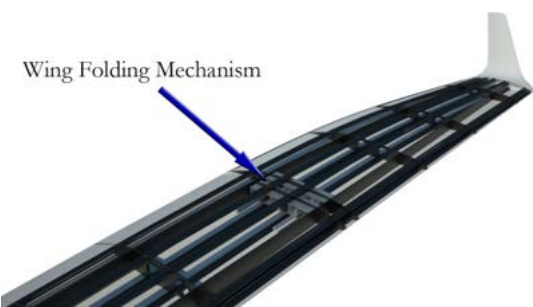


Fig. 70 Wing folding mechanism structure close-up

It was noted that the geometry of the T-hangar is not fully regulated, especially with regards to the height of the hangar. It was observed that T-hangars with minimum heights of 10'-6" are widely available and many T-hangars have door heights exceeding 12'. This geometry ultimately defined the location of the fold line for the wing given a door span of 40', as dictated by the RFP. Figures 71 and 72 present Pandion stored in a T-hangar.

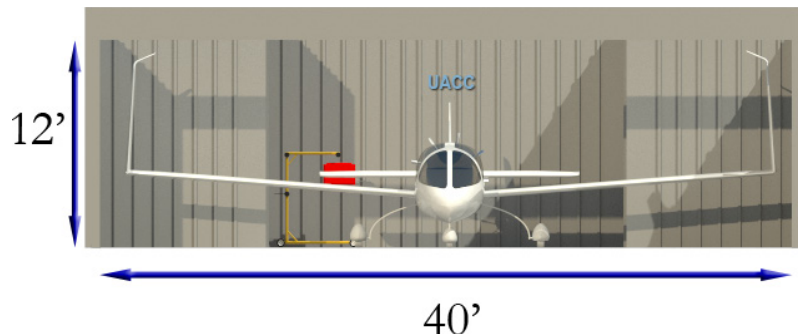


Fig. 71 Front view of T-hangar storage

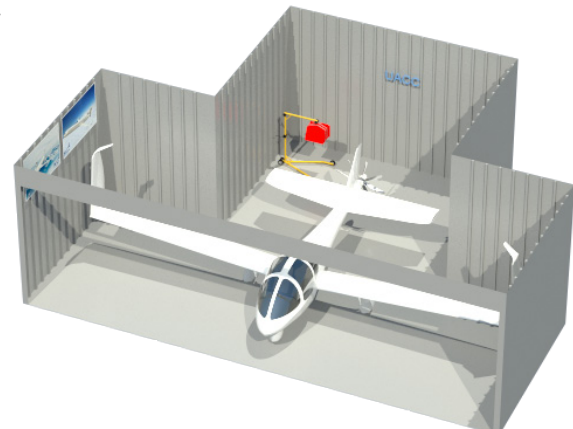


Fig. 72 Isometric view of T-hangar storage

## 14.2 Battery Recharging Performance

As mentioned in Sec. 9.1, Pandion has an onboard battery charger for use during ground operations. In order to minimize the charging time while maximizing the compatibility with the current electrical grid, the SAE J1772 electrical connector standard<sup>78</sup> was adopted in Pandion. This standard allows for a maximum charging power 19.2  $kW$  when connected to a 240  $VAC$  socket, which is standard and widely available. This will result in a full charge in 3.8 hrs. Figure 73 shows the onboard charger located in the mid fuselage.

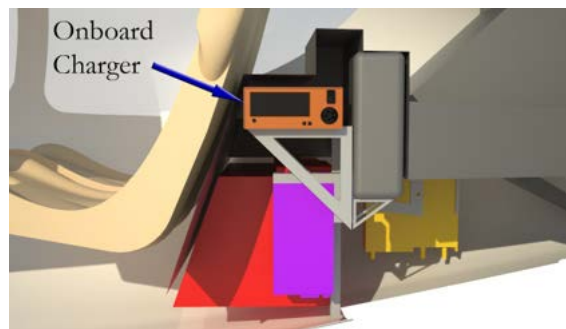


Fig. 73 Location of the onboard charger

## 14.3 Battery Lifecycle & Replacement

As part of the product lifecycle evaluation of Pandion, an estimation of the durability of the battery was performed. For this purpose, UACC contacted a leading expert in the field of advanced Li-air battery technology, *Dr. Binod Kumar*, regarding the maximum charge-discharge cycles and shelf life of Li-air batteries. In private correspondence with *Dr. Kumar*, an estimated 500 charge cycles and five year shelf life was determined to be achievable with this battery technology.

Even though lithium is corrosive and may be hazardous for the environment, the manufacture and operation of Li-air batteries have proven to be both environmentally conscious and safe for human use in a wide range of applications. Furthermore, the solid-state nature of Li-air batteries makes them safe even when subject to punctures or other mechanical failures<sup>79</sup>. A means for disposing the battery is necessary due to the use of lithium as the anode material of the battery. However, given the wide use of lithium-ion and other types of lithium-based batteries, there is an established infrastructure to take care of the batteries once their end-of-life is reached. It should be noted that apart from regular verification of the correct functioning of the battery and its charge level indicator, the Li-air battery does not required any scheduled maintenance throughout its lifecycle.

#### 14.4 Extended Endurance Battery Package

As required by the RFP, Pandion has the option of installing an additional battery pack in place of a passenger in order to increase range for single-pilot operations. In order to utilize economies of scale and reduce the overall cost of producing the batteries, UACC decided that the ERP would be identical to the main battery pack. As a result, the battery accessories will be common, which simplifies maintenance by reducing the number of spare parts required. This feature also allows the ERP to be used as a replacement for the main battery when it has reached its end-of-life.

When installed, the additional battery provides energy for an extended range of 510 *nmi*, 275 *nmi* longer than the standard 235 *nmi* block range. In order to install the extended range pack (ERP), the passenger-side seat and stick must be removed so that space can be made available for safe operation. Given that the ERP is used to increase energy capacity, but not the overall power of the aircraft, the use of dedicated cooling and control systems for each battery is not required. Instead, the installation of the ERP only requires use of two connections for power and coolant, without the need to install additional cooling or control systems.

To aid the installation of the ERP, a small, light-weight personal-use crane is available, which can be used to lift and transport the battery from storage to its final location in the plane, and vice versa. Once the battery has been positioned, it is fastened in place to guarantee safe operation during flight. The final phase of installing the ERP is securing the electric and coolant connections. Figures 74 and 75 show the ERP installation process and the cockpit with the ERP installed.



Fig. 74 ERP installation process with a light-weight, 81 personal use crane

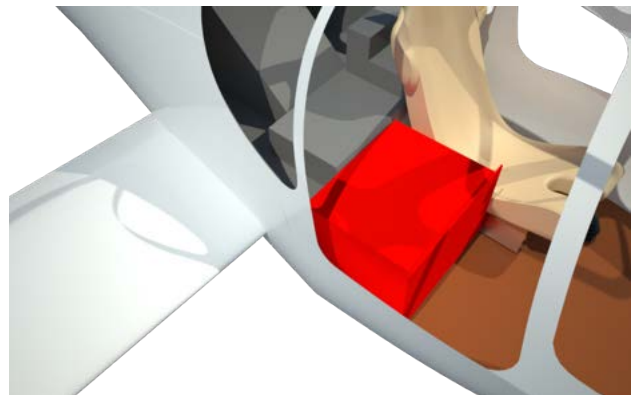


Fig. 75 Cockpit with ERP installed

## 14.5 Regular Inspections

One of the advantages of electric over conventional aircraft is the reduction in the number of components and systems that require regular inspections and service, such as fuel and lubricating systems. Furthermore, the inspection of electric and electronic components is usually simpler than that of equivalent mechanical systems<sup>80</sup>. Such is the case of the electric motor and battery for which computerized tests can be performed to assess airworthiness. A preflight automatic test is used in Pandion to ensure the correct functioning of the electric and electronic components. The airplane also has access panels that allow for inspection of electrical and mechanical components, including the propeller tilting mechanism, the electric motor, the battery, the charging system, the wing folding mechanism, and the cooling system. Figure 76 shows the location of the access panels.

### Access Panels

- |                      |                           |
|----------------------|---------------------------|
| 1: Battery           | 4: Wing Folding Mechanism |
| 2: Charger & Coolant | 5: Prop Tilting Mechanism |
| 3: Motor             |                           |

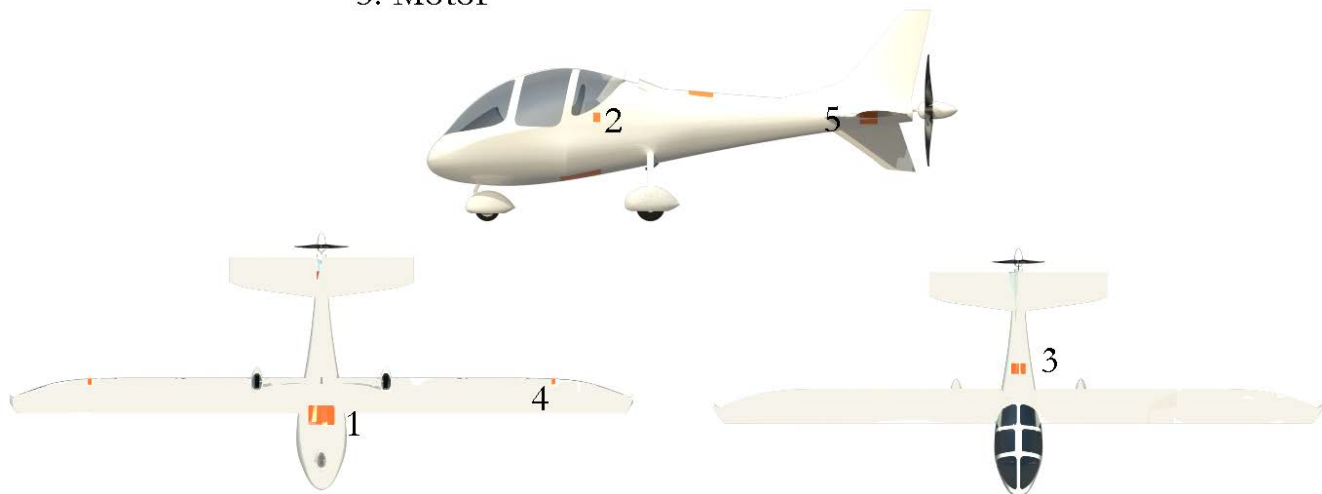
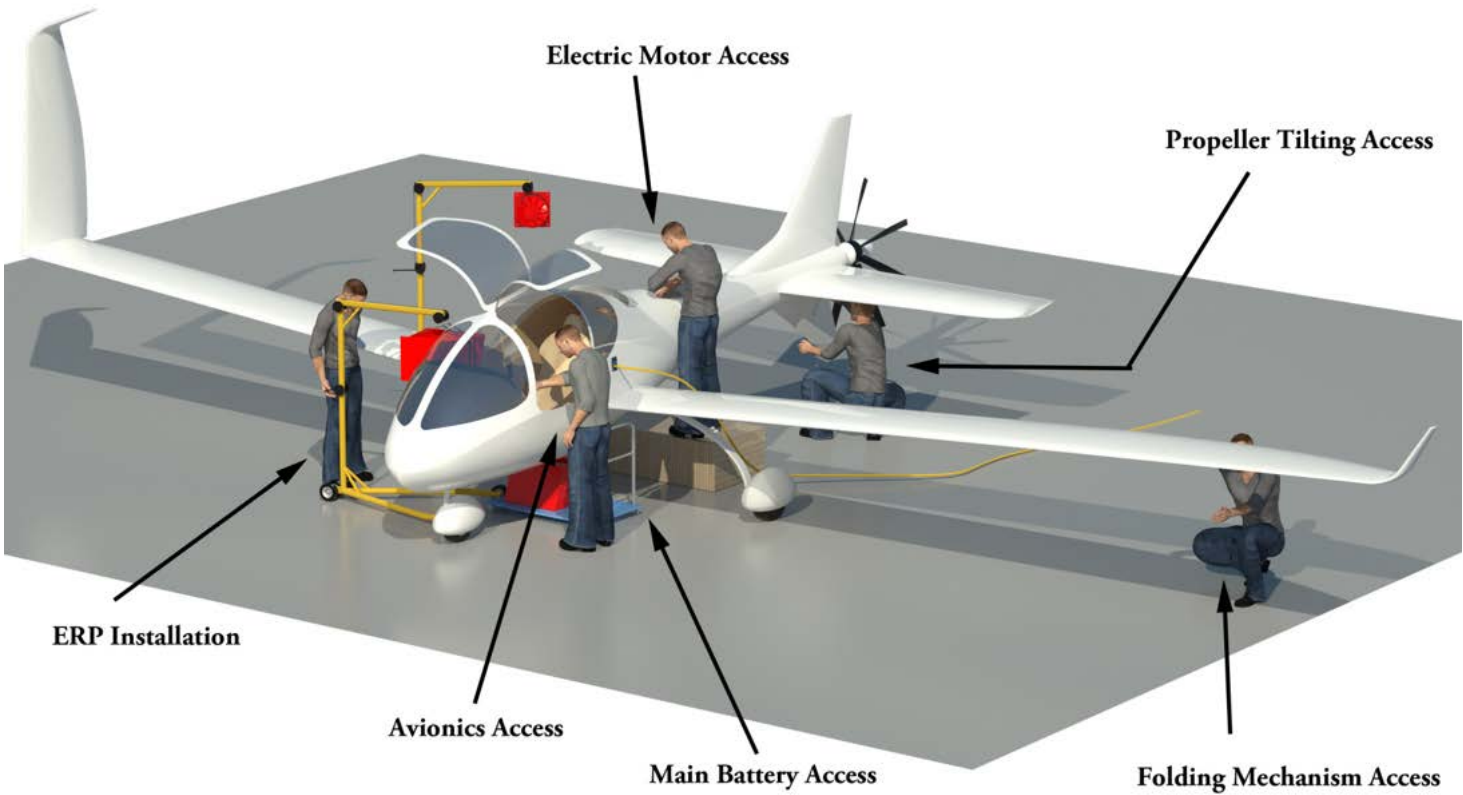


Fig. 76 Access Panels

## 14.6 Accessibility Picture



## 15.0 Safety Features and Analysis

### 15.1 Deep Stalls and Propeller Tilting

Reviewing the information regarding general aviation accidents published by the NTSB, it was observed that approximately 50% of the accidents of personal general aviation aircraft occur during takeoff and landing phases of flight<sup>81</sup>. Seeing as these flight phases involve lower speeds, higher angles of attack, and lower altitudes, deep stall may be one of the primary causes. Therefore, an innovative system that can assist the pilot from recovering excessive angles of attack at low speed and altitude may improve the safety of the aircraft. UACC introduced a novel propeller tilting system that accomplishes this task, as explained in Sec. 5.4. This system autonomously detects deep stalls and increases the propeller inclination angle to produce a nose-down moment (depending on the airplane attitude) to assist stall recovery.

### 15.2 Parachute Deployment

In order to improve the overall crash survivability, a parachute airframe recovery system was designed and implemented following the methodology presented by *Knacke*<sup>82</sup>. A 14.3% extended skirt canopy was selected given its performance for the sport aircraft application, i.e. high drag coefficient and low angle of oscillation (less than 15°). A descent rate of 25 ft./sec. was chosen following *Knacke's* recommendation for the design of the parachute. The designed parachute has a nominal diameter of 42' and is constructed of rip-stop nylon sized to recover the aircraft at dive speed and maximum weight. The parachute package is located in the central fuselage from where the parachute canopy is deployed by a *Cesaroni* Pro 29<sup>83</sup> solid rocket motor that pulls the canopy through the intake located on the upper fuselage. The parachute is attached to the airframe at three points, two of which are attached to the rear wing spar near the wing roots. A third riser is attached to the foremost fuselage frame and breaks through the skin of the aircraft along the fuselage centerline when the parachute is deployed. Figures 77 and 78 on the following page show the geometry of the deployed canopy and the parachute package in the fuselage. The design was validated by comparing

the resulting dimensions and characteristics with those of commercially available parachute recovery systems manufactured by *BRS Aerospace*<sup>84</sup>.



Fig. 77 Deployed canopy

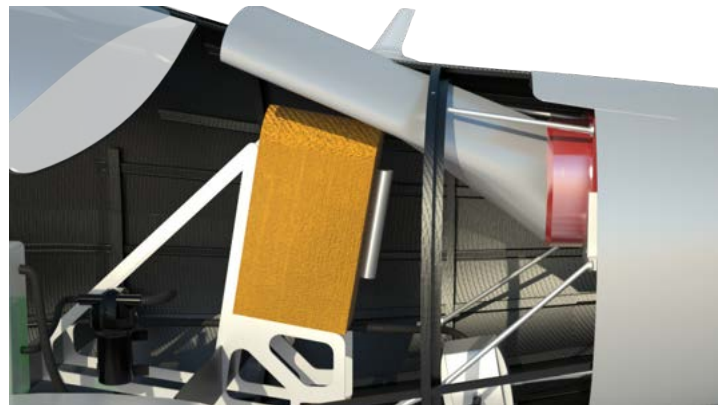


Fig. 78 Parachute package inside the mid fuselage. To facilitate deployment of the parachute, the intake is especially designed with weakened regions.

### 15.3 G Seats, Seatbelts, and Airbags

The cockpit is outfitted with high-G, ergonomic, lumbar-supported seats based on the *Oregon Aero* High-G Seat, which passes the 19-G lumbar load survivability test required for certified general aviation aircraft<sup>85</sup>. This seat increases the crash survivability and passenger safety by protecting the occupants from severe injury and from becoming trapped due to excessive seat deformation. A four-point *AMSAFE* airbag seatbelt system was selected to further improve safety and crash survivability. Figure 79 shows the cockpit G-seats and seatbelts.



Fig. 79 Cockpit G-seats and seatbelts

### 15.4 Wings Folded

Considerations were made for the unlikely scenario in which the pilot must perform a takeoff or landing maneuver with folded wings. As the Pandion configuration has the ailerons located inboard of the folding section of the wing in case of such mishap, the craft maintains all modes of control and only flight dynamics and performance are slightly influenced. In order to quantify these effects, flight simulations were performed using *X-Plane 9*<sup>86</sup>, replicating a hot day (ISA+20 °C) takeoff from a runway at 2,000' altitude with the wingtip sections completely folded.

Figure 80 presents a snapshot of the virtual aircraft during the flight dynamic simulation. The analysis showed that Pandion can achieve a roll rate of  $15^\circ/\text{sec}$ , a climb rate of  $1,350 \text{ fpm}$ , and a sustained turn rate of  $3.2^\circ/\text{sec}$  while flying with folded wings. The general behavior of the airplane was satisfactory and the spiral modes at low altitude and low speed were improved due to the increase in the side area of the airplane.



**Fig. 80 Wings folded flight dynamic simulation**

### 15.5 Blade Loss

As the propeller for Pandion is located behind the fuselage, in case of a blade loss event no critical part of the aircraft is exposed to propeller debris. However, should a more catastrophic cause, such as a fracture in the propeller driveshaft, occurs the propeller disc may be able to inflict minor damage to the empennage section. In this unlikely event, the Pandion configuration contains multiple vertical surfaces (vertical tail and ventral fin) and fault tolerant flight control systems that will allow controlled flight even if limited damage is sustained.

### 15.6 Lightning Strike

Considering the heavy use of composites in the structure of Pandion, it is realized that a low-altitude lightning strike will present a serious threat to the integrity of the aircraft. This is caused by the non-conductive nature of composites, which results in significant structural damage when subject to high electric current. This damage is caused by high temperatures that result from the accumulation of charge in the structure at the strike point<sup>87</sup>. To remedy this issue, a network of conductors can be utilized or conductive material may be embedded in the CFRP composite matrix. Also, parts of the structure that have a higher probability of being struck by lightning (especially wingtips and the tips of empennage surfaces<sup>88</sup>) may be manufactured from metallic material to facilitate current transfer locally<sup>89</sup>. Pandion implements both approaches by having aluminum tips for the wing and empennage and an embedded copper mesh to improve the conductivity of the CFRP material.

## 16.0 Cost & Risk Analysis

### 16.1 Market Forecast

The LSA category was introduced by the FAA in 2004 with the implementation of Rule 69 FR 44772<sup>90</sup>. Since then, over 7,000 aircraft and 120,000 pilots have been registered or certified in the US in the LSA category. The FAA forecasts an average long-term annual growth of 3.3% in the LSA fleet in the US and 6.1% in the number of sport pilots<sup>91</sup>. Figure 81 shows the number of LSA-type aircraft and pilots forecasted by the FAA for 2005-2031. From this data, an average of 300 new LSAs will be added to the US fleet each year starting in 2013.

Considering that North America accounts for 53.4% of the total worldwide market for small aircraft<sup>92</sup>, UACC expects a worldwide market of over 600 LSA-units per year.

Assuming a 20-year production run of 500 or 1,500 aircraft would result in an average of 25 or 75 aircraft per year, respectively. From the projected worldwide annual sales of LSAs, an 4% to 12.5% market share is achievable depending on the rate of production. Given the ever-rising cost of aviation fuel and very low operating costs of an electric airplane, Pandion is expected to present a significant market advantage over competitor S-LSAs.

### 16.2 Project Risk Assessment

UACC has determined that the highest development risk item from the standpoint of the project schedule for Pandion is the Li-air battery pack. Correspondence with present-day developers indicates that they have high certainty of the pack being available well in advance of the 2016 entry into service for Pandion. However, should this projection fail to materialize, i.e. there is a delay in the development or certification of the battery, alternatives must be considered. There will be two options for Pandion, the first of which is to use readily available alternative battery technologies that may cause a significant reduction in the range and endurance of the aircraft due to their higher

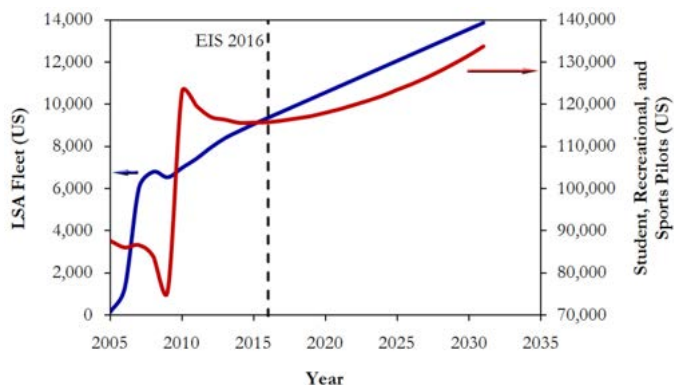


**Fig. 81 Results of number of LSAs and pilots forecasted from 2005-2031**

weight and reduced energy capacity. UACC has considered other possible battery technologies that could be applied in Pandion, including lithium-ion and zinc-air. Li-ion batteries have been developed and are approaching their maximum practical capacity<sup>93</sup>, which is around four times smaller than that of Li-air batteries. This would result in an increase of approximately 560 *lb.* to store the same amount of energy, which would result in a significant reduction in range and endurance. Rechargeable zinc-air batteries have been developed, and companies such as *ReVolt* are already planning on commercializing this type of battery in the near future<sup>94</sup>. Zinc-air batteries can store a similar amount of energy per unit volume as Lithium-air batteries<sup>95</sup>, which will make it possible to have the same size of battery as the one already designed. However, given the larger weight of Zn-air batteries, the range and endurance would be reduced by about 12.5 %. This would result in a maximum range of 205 *nmi.* and a maximum endurance of 2.5 *hrs.* for a Zn-air battery version of Pandion. It should be noted that this version of Pandion would still fulfill the RFP endurance requirements.

The second option is to delay the entry-into-service date to allow for the maturation of the Li-air battery technology. This option presents the lowest risk of meeting the performance target for the aircraft, which is a crucial marketing advantage for Pandion. However, it would increase the development costs and may delay and reduce the return on the original investment.

### 16.3 Itemized Cost Estimation

To obtain the most accurate estimation of the unit cost of Pandion, a method was synthesized using parts of methods presented by *Roskam* and the *RAND Corporation*. The method presented by *Roskam*<sup>96</sup> is applicable only to aircraft with metallic structures. This requires a modification to capture significant features of this aircraft that are otherwise unaccounted for, such as the extensive use of composite materials. For this purpose, parts of a methodology developed by the *RAND Corporation*<sup>97</sup> were used. This methodology assesses the effect of the type of the structural materials on the overall airframe cost by assigning complexity and cost factors to each material relative to aluminum. The method then calculates projected component costs of engineering,

tooling, materials, and labor based on the weight and type of raw material used. The method presented limitations given its publication date and the type of aircraft considered for the derivations (mainly fighter aircraft with weights greater than 10,000 lb.).

The empirical equations presented by *Roskam* were modified with the complexity factors from *RAND* to obtain accurate projected costs for each component from design to manufacture. The itemized cost breakdown for a production run of 500 aircraft is presented in table on the following page. In order to obtain flyaway costs, the itemized cost estimation process was repeated assuming different production runs as presented in Fig. 82. Flyaway costs of \$303,000 and \$144,000 were obtained for 100 and 500-unit production runs, respectively, using a US labor rate. Using a China labor rate, flyaway costs of \$200,000 and \$96,000 were obtained for 100 and 500 unit production runs, respectively.

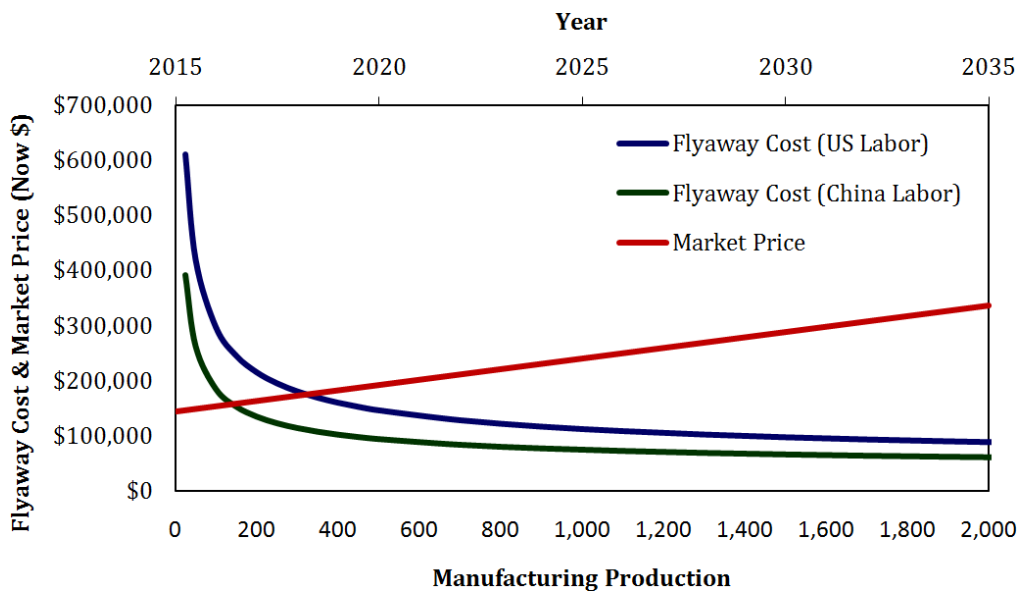


**Fig. 82 Flyaway Cost and Market Price at varying manufacturing productions, using US and Chinese labor rates**

Table 22 Flyaway cost calculation for a production run of 500 Units.

| #      | Component                   | Material Composition (%) |          |                  |       |                | Nonrecurring Engineering Hour for 500 Units (Hours) | Nonrecurring Tooling Hour for 500 Units (Hours) | Recurring Engineering Hour for 500 Units (Hours) | Recurring Tooling Hour for 500 Units (Hours) | Recurring Manufacturing Labor Hour for 500 Units (Hours) | Recurring Quality Assurance Hour for 500 Units (Hours) | Recurring Material Cost for 500 Units (\$) | Purchase Cost for 500 Units (\$) |
|--------|-----------------------------|--------------------------|----------|------------------|-------|----------------|---|---|--|--|--|--|--|----------------------------------|
|        |                             | Weight (lb)              | Aluminum | Titanium         | Steel | CFRP           |   |   |  |  |  |  |  |                                  |
| 1      | AMPR Weight (Reference)     | 526                      |          |                  |       |                | 6142.99   | 38998.17  | 16873.41   | 89692.11                                     | 586710.63  | 76272.38   | \$1,257,237.06                             |                                  |
| 1.1    | Wing                        |                          |          |                  |       |                |   |   |  |  |  |  |  |                                  |
| 1.1.1  | Wing Spars                  | 43                       | 0        | 0                | 0     | 100            | 0   | 550.05  | 3780.29  | 1698.00                                      | 10683.68   | 59041.66   | 7675.42                                    | \$233,412.51                     |
| 1.1.2  | Wing Ribs                   | 23                       | 0        | 0                | 0     | 100            | 0   | 289.35  | 1988.57  | 893.21                                       | 5620.00  | 31058.02   | 4037.54                                    | \$122,783.30                     |
| 1.1.3  | Wing Skin                   | 12                       | 0        | 0                | 0     | 100            | 0   | 151.74  | 1042.84  | 468.41                                       | 2947.22  | 16287.35   | 2117.36                                    | \$64,389.66                      |
| 1.1.4  | Wing Aileron                | 5                        | 0        | 0                | 0     | 100            | 0   | 60.72   | 417.31   | 187.44                                       | 1179.38  | 6517.67  | 847.30                                     | \$25,766.67                      |
| 1.1.5  | Wing Flap                   | 19                       | 0        | 0                | 0     | 100            | 0   | 243.90  | 1676.24  | 752.92                                       | 4737.31  | 26180.01   | 3403.40                                    | \$103,496.81                     |
| 1.1.6  | Wingtip                     | 5                        | 0        | 0                | 0     | 100            | 0   | 58.30   | 400.69   | 179.98                                       | 1132.41  | 6258.06  | 813.55                                     | \$24,740.32                      |
| 1.1.7  | Longeron                    | 19                       | 0        | 0                | 0     | 100            | 0   | 246.58  | 1694.61  | 761.17                                       | 4789.23  | 26466.95   | 3440.70                                    | \$104,633.20                     |
| 1.1.8  | Winglet                     | 3                        | 0        | 0                | 0     | 100            | 0   | 37.93   | 260.71   | 117.10                                       | 736.81   | 4071.84  | 529.34                                     | \$16,097.41                      |
| 1.1.9  | Folding Mechanism           | 12                       | 100      | 0                | 0     | 0              | 0   | 141.20  | 896.36   | 370.38                                       | 1968.78  | 12878.58   | 1674.22                                    | \$26,296.57                      |
| 1.1.10 | Wing Box                    | 15                       | 100      | 0                | 0     | 0              | 0   | 169.46  | 1075.79  | 444.52                                       | 2362.87  | 15456.42   | 2009.33                                    | \$31,560.24                      |
| 2      | Horizontal Tail             |                          |          |                  |       |                |   |   |  |  |  |  |  |                                  |
| 2.1    | H Tail Spar                 | 14                       | 0        | 0                | 0     | 100            | 0   | 184.20  | 1265.93  | 568.62                                       | 3577.71  | 19771.65   | 2570.31                                    | \$78,164.29                      |
| 2.2    | H Tail Rib                  | 6                        | 0        | 0                | 0     | 100            | 0   | 71.92   | 494.30   | 222.02                                       | 1396.96  | 7720.10  | 1003.61                                    | \$30,520.27                      |
| 2.3    | H Tail Skin                 | 5                        | 0        | 0                | 0     | 100            | 0   | 62.38   | 428.68   | 192.55                                       | 1211.53  | 6695.31  | 870.39                                     | \$26,468.90                      |
| 2.4    | Elevator                    | 5                        | 0        | 0                | 0     | 100            | 0   | 64.67   | 444.43   | 199.63                                       | 1266.03  | 6941.26  | 902.36                                     | \$27,441.23                      |
| 2.5    | Elevator Tab                | 0                        | 0        | 0                | 0     | 100            | 0   | 3.82  | 26.25  | 11.79  | 74.18  | 409.92   | 53.29                                      | \$1,620.55                       |
| 2.6    | Adapter                     | 35                       | 0        | 100              | 0     | 0              | 0   | 413.54  | 3097.89  | 1238.14                                      | 7668.28  | 46606.46   | 6058.84                                    | \$149,383.31                     |
| 3      | Vertical Tail               |                          |          |                  |       |                |   |   |  |  |  |  |  |                                  |
| 3.1    | V Tail Spar                 | 2                        | 0        | 0                | 0     | 100            | 0   | 23.30   | 160.10   | 71.91  | 452.47   | 2500.49  | 325.06                                     | \$9,885.33                       |
| 3.2    | V Tail Rib                  | 2                        | 0        | 0                | 0     | 100            | 0   | 28.26   | 194.22   | 87.24  | 548.90   | 3033.38  | 394.34                                     | \$11,992.03                      |
| 3.3    | V Tail Skin                 | 2                        | 0        | 0                | 0     | 100            | 0   | 22.66   | 155.73   | 69.95  | 440.11   | 2432.17  | 316.18                                     | \$9,615.23                       |
| 3.4    | Rudder                      | 1                        | 0        | 0                | 0     | 100            | 0   | 9.42  | 64.74  | 29.08  | 182.97   | 1011.13  | 131.45                                     | \$3,997.34                       |
| 3.5    | Adapter                     | 2                        | 0        | 100              | 0     | 0              | 0   | 27.91   | 209.09   | 83.57  | 517.57   | 3145.71  | 408.94                                     | \$10,082.63                      |
| 4      | Fuselage                    |                          |          |                  |       |                |   |   |  |  |  |  |  |                                  |
| 4.1    | Fuselage Frame              | 21                       | 0        | 0                | 0     | 100            | 0   | 268.47  | 1845.09  | 828.76                                       | 5214.51  | 28817.14   | 3746.23                                    | \$113,924.32                     |
| 4.2    | Fuselage Longeron           | 15                       | 0        | 0                | 0     | 100            | 0   | 196.29  | 1349.04  | 605.95                                       | 3812.60  | 21069.72   | 2739.06                                    | \$83,296.02                      |
| 4.3    | Fuselage Skin               | 10                       | 0        | 0                | 0     | 100            | 0   | 126.53  | 869.61   | 390.61                                       | 2457.67  | 13581.90   | 1765.65                                    | \$53,694.06                      |
| 4.4    | Seat Railings               | 7                        | 0        | 100              | 0     | 0              | 0   | 80.12   | 600.16   | 239.87                                       | 1485.58  | 9029.10  | 1173.78                                    | \$28,940.12                      |
| 4.5    | Cockpit Reinforcements      | 38                       | 0        | 0                | 100   | 0              | 0   | 457.78  | 2906.18  | 1257.42                                      | 7547.40  | 45604.93   | 5928.64                                    | \$77,552.29                      |
| 4.6    | Rail Support Frame          | 1                        | 0        | 0                | 0     | 100            | 0   | 18.20   | 125.11   | 56.19  | 353.57   | 1953.94  | 254.01                                     | \$7,724.60                       |
| 4.7    | Transparencies              | 24                       | 0        | 0                | 0     | 0              | 100   | 326.88  | 2233.45  | 897.87                                       | 6592.81  | 33601.34   | 4368.17                                    | \$143,438.80                     |
| 5      | Propeller System            |                          |          |                  |       |                |   |   |  |  |  |  |  | \$750,000.00                     |
| 5.1    | Propeller                   | 23                       | 33       | 0                | 0     | 67             | 0   |   |  |  |  |  |  |                                  |
| 5.2    | Drive Shaft                 | 18                       | 0        | 0                | 100   | 0              | 0   | 220.16  | 1397.69  | 604.74                                       | 3629.84  | 21933.16   | 2851.31                                    | \$37,297.87                      |
| 5.3    | Tilting System              | 1                        | 100      | 0                | 0     | 0              | 0   | 12.50   | 79.33  | 32.78  | 174.24   | 1139.79  | 148.17                                     | \$2,327.32                       |
| 5.4    | Tilting Motor Actuator      | 14                       | 0        | 0                | 100   | 0              | 0   | 170.86  | 1084.68  | 489.31                                       | 2816.95  | 17021.30   | 2212.77                                    | \$28,945.13                      |
| 5.5    | Propeller Motor (81 HP)     | 66                       |          |                  |       |                |   |   |  |  |  |  |  | \$6,000,000.00                   |
| 6      | Air Induction System        |                          |          |                  |       |                |   |   |  |  |  |  |  | \$5,000.00                       |
| 6.1    | Intakes                     | 1                        |          |                  |       |                |   |   |  |  |  |  |  |                                  |
| 7      | Flight Control System       |                          |          |                  |       |                |   |   |  |  |  |  |  |                                  |
| 7.1    | Control Systems & Equipment | 6                        | 86       | 0                | 14    | 0              | 0   | 73.22   | 464.81   | 193.38                                       | 1047.98  | 6767.69  | 879.80                                     | \$13,456.86                      |
| 7.2    | Nose Landing Gear           |                          |          |                  |       |                |   |   |  |  |  |  |  |                                  |
| 7.2.1  | Strut                       | 3                        | 100      | 0                | 0     | 0              | 0   | 34.10   | 216.49   | 89.45  | 475.50   | 3110.46  | 404.36                                     | \$6,351.20                       |
| 7.2.2  | Fairing                     | 3                        | 0        | 0                | 0     | 0              | 100   | 36.11   | 246.70   | 99.17  | 728.21   | 3711.45  | 482.49                                     | \$15,843.58                      |
| 7.2.3  | Electromechanical Steering  | 5                        |          |                  |       |                |   |   |  |  |  |  |  | \$500,000.00                     |
| 7.2.4  | Tire & Rim                  | 10                       |          |                  |       |                |   |   |  |  |  |  |  | \$125,000.00                     |
| 8      | Main Landing Gear           |                          |          |                  |       |                |   |   |  |  |  |  |  |                                  |
| 8.1    | Leaf Spring                 | 52                       |          |                  |       |                |   |   |  |  |  |  |  | \$125,000.00                     |
| 8.2    | Fairing                     | 7                        | 0        | 0                | 0     | 0              | 100   | 89.58   | 612.03   | 246.04                                       | 1806.63  | 9207.79  | 1197.01                                    | \$39,306.58                      |
| 8.3    | Hydraulic Braking System &  | 6                        |          |                  |       |                |   |   |  |  |  |  |  | \$700,000.00                     |
| 8.4    | Tire & Rim (x2)             | 20                       |          |                  |       |                |   |   |  |  |  |  |  | \$250,000.00                     |
| 9      | Cooling System              |                          |          |                  |       |                |   |   |  |  |  |  |  |                                  |
| 9.1    | Heat Exchangers             | 6                        |          |                  |       |                |   |   |  |  |  |  |  | \$150,000.00                     |
| 9.2    | Coolant & Reservoir         | 9                        |          |                  |       |                |   |   |  |  |  |  |  | \$10,000.00                      |
| 9.3    | Coolant Pump & Piping       | 9                        |          |                  |       |                |   |   |  |  |  |  |  | \$150,000.00                     |
| 10     | Electrical System           |                          |          |                  |       |                |   |   |  |  |  |  |  |                                  |
| 10.1   | Wiring                      | 2                        |          |                  |       |                |   |   |  |  |  |  |  | \$2,000.00                       |
| 10.2   | Circuit Breaker             | 4                        |          |                  |       |                |   |   |  |  |  |  |  | \$162,500.00                     |
| 10.3   | DC/DC Converter             | 5                        |          |                  |       |                |   |   |  |  |  |  |  | \$400,000.00                     |
| 10.4   | Power Control               | 22                       |          |                  |       |                |   |   |  |  |  |  |  | \$1,000,000.00                   |
| 10.5   | Avionics (Garmin GTN650)    | 7                        |          |                  |       |                |   |   |  |  |  |  |  | \$5,500,000.00                   |
| 10.6   | Battery (Li-Air)            | 160                      |          |                  |       |                |   |   |  |  |  |  |  | \$4,500,000.00                   |
| 11     | Furnishings, Safety & Etc.  |                          |          |                  |       |                |   |   |  |  |  |  |  |                                  |
| 11.1   | Cockpit Accessories         | 25                       |          |                  |       |                |   |   |  |  |  |  |  | \$225,000.00                     |
| 11.2   | Sunshade                    | 1                        |          |                  |       |                |   |   |  |  |  |  |  | \$25,000.00                      |
| 11.3   | Parachute                   | 33                       |          |                  |       |                |   |   |  |  |  |  |  | \$500,000.00                     |
| 11.4   | Paint                       | 3                        |          |                  |       |                |   |   |  |  |  |  |  | \$50,000.00                      |
|        | Total Hours                 | 4972.10                  |          | 33805.13         |       | 14659.19       |   | 91627.87  |  | 521033.84                                    |  | 67734.40   |  |                                  |
|        | Total Cost                  | \$401,746.00             |          | \$2,386,641.85   |       | \$1,184,462.27 |   | \$6,468,927.57                                  |  | \$10,420,676.75                              |  | \$4,443,376.56   |  | \$1,764,448.57                   |
|        | Unit Cost                   | \$96,399.56              |          | China Labor Rate |       |                |   |   |  |  |  |  |  | \$21,129,500.00                  |
|        |                             | \$144,438.88             |          | US Labor Rate    |       |                |   |   |  |  |  |  |  |                                  |

#### 16.4 Operating Cost

A revised version of the method of estimating operating cost for piston-engine aircraft presented by *Roskam*<sup>98</sup> was applied to Pandion. A modification was made to take into account the use of electricity instead of fuel as the source of energy for the aircraft. It was assumed that electricity was purchased at a rate of 0.07 USD/kW-hr. based on the current market price of electricity for industrial applications<sup>99</sup>. Table 22 presents a breakdown of operating costs for Pandion compared to Cessna 162 and Breezer 600L, which are similarly sized piston-engine LSAs. The comparison airplanes were analyzed using the *Roskam* method mentioned above for single-engine piston airplanes assuming an aviation fuel price of 5.25 USD/gal.<sup>100</sup>.

Fig. 22 Breakdown of Operating Costs

| Cost Item                      | Cessna 162  | Breezer 600L | Pandion     | Average Change from Conventional Competitors (Cessna 162, Breezer 600L) |
|--------------------------------|-------------|--------------|-------------|---|
| Annual Utilization (nm.)       | 43,640      | 38,640       | 33,560      | -----   |
| Crew (\$/nm.)                  | 0           | 0            | 0           | 0   |
| Fuel, Oil & Env. Tax (\$/nm.)  | 0.35        | 0.21         | 0.02        | -94.3%, -90.5%  |
| Insurance (\$/nm.)             | 0.05        | 0.05         | 0.09        | +50%, +50.0%  |
| Maintenance (\$/nm.)           | 0.29        | 0.32         | 0.24        | -17.2%, -25.0%  |
| Depreciation (\$/nm.)          | 0.26        | 0.30         | 0.33        | +26.9%, +10.0%  |
| Landing & Navigation Fees (\$) | 0.01        | 0.02         | 0.02        | -----   |
| <b>Total DOC* (\$/nm.)</b>     | <b>1.03</b> | <b>0.96</b>  | <b>0.75</b> | <b>-27.2%, -21.9%</b>   |

## References

---

- <sup>1</sup>Roskam, Jan., Airplane Design, Part I through VIII , DAR Corporation, 2003
- <sup>2</sup>Heinemann, E., Raussa, R. and Van Every, K., Aircraft Design, The Nautical and Aviation Publication Co., 1985
- <sup>3</sup>Eppinger, Steven D. and Ulrich, Karl T., Product Design and Development, Second Edition, Irwin McGraw-Hill, Boston, 2000
- <sup>4</sup>Roskam, Jan. Airplane Design Part I Sec. 341 p. 118-187. DAR Corporation. 1987
- <sup>5</sup>Roskam, Jan. Airplane Design Part II Fig. 12.7 p.286. DAR Corporation. 1997
- <sup>6</sup>“Engineering Science Data Unit”. *Volumes on Performance*, item 73018. “Estimation of Cruise Range: Propeller-Driven Aircraft.”August 1975
- <sup>7</sup>K. M. Abraham. A Brief History of Non-aqueous Metal-Air Batteries. ECS Transactions, 3(42) 67-71. 2008
- <sup>8</sup>MIT Professor
- <sup>9</sup>Yuneec International. Power Drive System Specifications. Acquired May 2011.  
[http://yuneeccouk.site.securepod.com/PowerMotor\\_Tech\\_spec.html](http://yuneeccouk.site.securepod.com/PowerMotor_Tech_spec.html)
- <sup>10</sup> Per suggestion of Dr. Lutgard C. De Jonghe, Faculty Senior Scientist at Lawrence Berkeley National Laboratory and Chairman of PolyPlus Battery Company
- <sup>11</sup> Appendix to Request for Proposal Document for Individual Aircraft Design Competition. AIAA. 2006-2007
- <sup>12</sup> University of Dayton Research Institute. Energy Storage & Generation. Electromechanical Power. Group Leader/Distinguished Research Engineer. Professor in the department of Aerospace and Mechanical Engineering, University of Dayton, OH.
- <sup>13</sup> Roskam, Jan. Airplane Design Part I Sects. 3.1-3.6 pgs 90-168. DAR Corporation 1997
- <sup>14</sup> “Engineering Science Data Unit”. *Volumes on Aerodynamics*, item 95021. “Wing Lift Coefficient Increment at Zero Angle of Attack”
- <sup>15</sup> FAA. “Aerospace Forecast Fiscal Years 2010-2030”. page 47
- <sup>16</sup> General Aviation Manufacturers Association. Industry Facts and Statistics. Statistical Databook and Industry Outlook publications 1999-2011. Acquired March 2011. <http://www.gama.aero/media-center/industry-facts-and-statistics/statistical-databook-and-industry-outlook>
- <sup>17</sup> Dan Johnson, President and Chairman of the Light Aircraft Manufacturers Association. Market Sales Information for LSA. Acquired March 2011. <http://www.bydanjohnson.com/index.cfm?b=1&m=5>
- <sup>18</sup> FAA. General Aviation and Part 135 Activity Surveys – CY 2009. Table 1.1. Acquired March 2011.  
[http://www.faa.gov/data\\_research/aviation\\_data\\_statistics/general\\_aviation/CY2009/](http://www.faa.gov/data_research/aviation_data_statistics/general_aviation/CY2009/)
- <sup>19</sup>Roskam, Jan. Airplane Design. Part III. DAR Corporation. 2003. Pgs 252-253
- <sup>20</sup> “Engineering Sciences Data Unit”. *Volumes on Aerodynamics*, item 71007. “Low Speed, Normal Force and Pitching Moment of Slender Wings in Ground Effect.”
- <sup>21</sup>Roskam, Jan. Roskam’s Airplane War Stories. DAR Corporation. 2002. Pg 82: Cessna 172’s sales have been increased by almost 30% as a result of similar changes affecting the look of the design.
- <sup>22</sup>Roskam, Jan. Airplane Design Part IV. DAR Corporation, 1997.
- <sup>23</sup> Redeker, G., Horstmann, K.H., Köster, H., and Quast A. Investigations on High Reynolds Number Laminar Flow Airfoils. Journal of Aircraft Vol. 25 № 7. July 1988.
- <sup>24</sup> University of Illinois at Urbana-Champaign Applied Aerodynamics Group. Department of Aerospace Engineering. Airfoil Coordinates Database. Acquired Sept-Dec. 2009.
- <sup>25</sup>Roskam, Jan. Airplane Design Part VI. DAR Corporation. 1990. Section 4.12.2, pgs 110-111
- <sup>26</sup>Oberg, Eric, et. al. Machinery’s Handbook. Industrial Press. 28<sup>th</sup> Edition. Feb 2008
- <sup>27</sup> “Engineering Science Data Unit”. *Volumes on Aircraft Aerodynamics*, item 98013. “Aerodynamic Principles of Winglets.” June, 1998.
- <sup>28</sup> Maughmer, Mark D. Design of Winglets for High-Performance Sailplanes. AIAA Journal of Aircraft. Vol. 40 № 6. Dec. 2003
- <sup>29</sup> “Engineering Science Data Unit”. *Volumes on Aerodynamics*, item 95021. “Wing Lift Coefficient Increment at Zero Angle of Attack”
- <sup>30</sup>Roskam, Jan. citing Torenbeek, E. Synthesis of Subsonic Airplane Design. Appendix G, p. 533. 1981
- <sup>31</sup>Roskam, Jan. Airplane Design Part VI. DAR Corporation. 1990. p. 21.

- <sup>32</sup> *Roskam, Jan.* Airplane Design. Part VI. DAR Corporation. 1990. All Sections relevant to Class II drag polar analysis for light airplanes were used.
- <sup>33</sup> *Torenbeek, E.* Synthesis of Subsonic Airplane Design. Chapters pertaining to low speed aerodynamic predictions. 1981
- <sup>34</sup> *Caralano, F.M.* and *Manusel, M.G.*, "Numerical and Experimental Analysis of the Effect of a Pusher Propeller on a Wing and Body." AIAA Meeting Papers on Disc. Jan., 1997.
- <sup>35</sup> *Manusel, M.G.* "A Study of Propeller/Wing/Body Interference for a Low Speed Twin-Engine Pusher Configuration" ICAS-90 5.4.3, 1990
- <sup>36</sup> *Koning, C.* "Influence of the Propeller on the Other Parts of the Aeroplane Structure" DIVM Aerodynamic Theory. Volume IV, Edited by Durand, W., CIT Cal, 1935.
- <sup>37</sup> *Roskam, Jan.* Airplane Design Part VI. DAR Corporation. 1990. Section 4.12.2, pgs 110-111
- <sup>38</sup> *Oberg, Eric, et. al.* Machinery's Handbook. Industrial Press. 28<sup>th</sup> Edition. Feb 2008
- <sup>39</sup> Advanced Aircraft Analysis help file on Structure. DAR Corporation. Keyword Libove's Axis. Wichita, Kansas. 2009.
- <sup>40</sup> *Roskam, Jan.* Airplane Design. Part IV. DAR Corporation, 1990. Section 2.4. Pg. 4. Note: Roskam derives his requirements from FAR §23.725.
- <sup>41</sup> *Oberg, Eric, et. al.* Machinery's Handbook. Industrial Press. 28<sup>th</sup> Edition. Feb 2008
- <sup>42</sup> *Molyneux, W.G.*, Hall, H. The Aerodynamic Effects of Aspect Ratio and Sweepback on Wing Flutter, Aeronautical Research Council-Reports & Memorandum . Her majesties Stationary Office, 1957
- <sup>43</sup> *Krishnan, R.* Permanent . Magnet Synchronous and Brushless DC Motor Devices. CRC Press. 2010.
- <sup>44</sup> *Hartzell Propeller Inc.* Advanced Propeller Design and Manufacturing. Technical Questions. 2009
- <sup>45</sup> *Dr. Lutgard C. De Jonghe*, Faculty Senior Scientist at Lawrence Berkeley National Laboratory and Chairman of PolyPlus Battery Company, and *Dr. Binod Kumar*, University of Dayton Research Institute. Energy Storage & Generation. Electromechanical Power. Group Leader/Distinguished Research Engineer. Professor in the department of Aerospace and Mechanical Engineering, University of Dayton, OH.
- <sup>46</sup> *Berchovsky, Gene et. al.* The Tesla Roadster Battery System. Tesla Motors, 2006.
- <sup>47</sup> Fokker Technologies. Fokker Services introduces Electronic Flight Bag hardware and mounting solution for iPad. 2011
- <sup>48</sup> *Berdichevsky, G., et. al.* The Tesla Roadster Battery System. Tesla Motors, 2006.
- <sup>49</sup> *Shah, R.K. and Sekulić, D.* Fundamentals of Heat Exchanger Design. John Wiley & Sons, 2003.
- <sup>50</sup> *Hesselgreaves, John E.* Compact Heat Exchangers: Selection, Design, and Operation. Pergamon, 2001.
- <sup>51</sup> "Engineering Science Data Unit". Volumes on Aircraft Performance, item 83042. "Estimation of Spray Patterns Generated from the Sides of Aircraft Tires Running in Water or Slush." Amendment A. April, 1998.
- <sup>52</sup> *Roskam, Jan.* Airplane Design Part V. DAR Corporation, 1997. p. 25
- <sup>53</sup> *Schmitt, R.L. et. al.* Weight Estimation Handbook for Light Aircraft. Cessna Aircraft Company, 1959.
- <sup>54</sup> *Torenbeek, E.* Synthesis of Subsonic Airplane Design. Kluwer Boston Inc., 1982.
- <sup>55</sup> *Roskam, Jan.* Airplane Design. Part V. DAR Corporation, 1990.
- <sup>56</sup> *Roskam, Jan.* Airplane Flight Dynamics and Automated Flight Controls. Part I Sec. 4.2.2. p. 205. 2003
- <sup>57</sup> *Roskam, Jan.* Airplane Design Part II. Section 11.1, pp. 24-25. DAR Corporation, 1997.
- <sup>58</sup> Military Specification MIL-F-8785 B Flying Qualities of Piloted Airplanes; 1969: Air Force Flight Dynamics Laboratory, WP AFB, Dayton, Ohio.
- <sup>59</sup> *Roskam, Jan.* Airplane Flight Dynamics and Automatic Flight Controls, Part I, DAR Corporation, 2003, p. 186.
- <sup>60</sup> *Roskam, Jan.* Airplane Flight Dynamics and Automatic Flight Controls, Part I, DAR Corporation, 2003, p. 143.
- <sup>61</sup> Military Specification MIL-F-8785 B Flying Qualities of Piloted Airplanes; 1969: Air Force Flight Dynamics Laboratory, WP AFB, Dayton, Ohio.
- <sup>62</sup> *Roskam, Jan.* Airplane Flight Dynamics and Automatic Flight Controls, Part I, DAR Corporation, 2003, p. 205.
- <sup>63</sup> *Roskam, Jan.* Airplane Flight Dynamics and Automatic Flight Controls, Part I, DAR Corporation, 1997, Secs. 5.3.2 & 5.3.10
- <sup>64</sup> *Hoak. D.E.* USAF Stability and Control DATCOM, Write Paterson AFB, OH
- <sup>65</sup> *Roskam, Jan.* Airplane Flight Dynamics and Automatic Flight Controls Part I, Section 5.2.4 & 5.2.5 PP 329-337 DAR Corp. 2003
- <sup>66</sup> *Roskam, Jan.* Airplane Design Part VI. Sec. 10. P 371-377. DAR Corporation. 1991.
- <sup>67</sup> *Roskam, Jan.* Airplane Design Part VI. Section 6.4, pp. 193-198. DAR Corporation, 1990.

- <sup>68</sup> “Engineering Science Data Unit”. *Volumes on Performance*, item 85029. “Calculation of Ground Performance in Takeoff and Landing”. Amendment A. March 2006.
- <sup>69</sup> “Engineering Science Data Unit”. *Volumes on Aerodynamics*, item 71007. “Low Speed Normal Force and Pitching Moment of Slender Wings in Ground Effects”. June 1971
- <sup>70</sup> *Roskam, Jan. Airplane Design Part VII Sec. 5.2 p. 117-123*. DAR Corporation. 1991
- <sup>71</sup> *Roskam, Jan. Airplane Design Part VII Sec 5.3. p. 124-130*. DAR Corporation. 1991.
- <sup>72</sup> *Roskam, Jan. Airplane Design Part VII Sec 5.7. p. 150-155*. DAR Corporation. 1991.
- <sup>73</sup> Engineering Science Data Unit. *Volumes on Performance*, item 91032. “Estimation of Airborne Performance and Landing”. October 1991.
- <sup>74</sup> Engineering Science Data Unit. *Volumes on Performance*, item 92020. “Energy Method for Analysis of Measured Airspeed Change in Landing Airborne Maneuvers.” Amendment A, December 1996.
- <sup>75</sup> Engineering Science Data Unit. *Volumes on Performance*, item EG6/4. “Estimation of Ground Run During Landing.” Amendment B, February 1992.
- <sup>76</sup> *Roskam, Jan. Airplane Design, Part VII. Sec. 5.1, pp. 113-116*. DAR Corporation, 1991.
- <sup>77</sup> Marte, Jack E. A Review of Aerodynamic Noise from Propellers, Rotors, and Lift Fans. National Aeronautics and Space Administration. Jet Propulsion Laboratory. Technical Report 32-1462. 1970
- <sup>78</sup> *SAE International*. SAE Electric Vehicle Conductive Charge Coupler. 2001.
- <sup>79</sup> Kumar, B. Personal correspondence. 2011.
- <sup>80</sup> *Gunawardana, S.* Electric Airplane Research Program. Stanford University. 2009.
- <sup>81</sup> *National Transport Safety Board*. Annual Review of Aircraft Accident Data: U.S. General Aviation. 2005.
- <sup>82</sup> *Knacke, Theo W.* Parachute Recovery Systems Design Manual. Naval Weapons Center, 1991.
- <sup>83</sup> *Cesaroni Technology*. Pro 29 2010 Catalog. V 1.0. Sarasota, FL.
- <sup>84</sup> *BRS Aerospace*. Recovery Systems Spec Sheet.
- <sup>85</sup> *Orgeon Aero High-G Seat*. <http://www.oregonaero.com/seat-systems/oem-high-g>. Accessed April 3, 2011.
- <sup>86</sup> *Laminar Research*. X-Plane v. 9.00. Created by Austin Meyer. <http://www.x-plane.com>.
- <sup>87</sup> *Szatkowski, George*. Lightning Strike Protection for Composite Aircraft. NASA Langley Research Center, 2009.
- <sup>88</sup> *Roskam, Jan. Airplane Design*. Part III. DAR Corporation. 1991.
- <sup>89</sup> *Szatkowski, George*. Lightning Strike Protection for Composite Aircraft. NASA Langley Research Center, 2009.
- <sup>90</sup> Federal Aviation Administration. “Certification of Aircraft and Airmen for the Operation of Light-Sport Aircraft”. July, 2004.
- <sup>91</sup> Federal Aviation Administration. “2011-2031 Aerospace Forecast”. 2011.
- <sup>92</sup> General Aviation Manufacturer Association. “General Aviation: Statistical Databook & Industry Outlook”. 2010.
- <sup>93</sup> *Linden, David and Reddy, Thomas*. “Handbook of Batteries” 3<sup>rd</sup> Edition. McGraw-Hill, 2001.
- <sup>94</sup> *Bullis, Kevin*. High-Energy Batteries Coming to Market. Technology Review, MIT. 2009.
- <sup>95</sup> *Linden, David and Reddy, Thomas*. “Handbook of Batteries” 3<sup>rd</sup> Edition. McGraw-Hill, 2001.
- <sup>96</sup> *Roskam, Jan. Airplane Design*. Part VIII. DAR Corporation, 1991.
- <sup>97</sup> *Resetar, Susan et. al*. “Advanced Airframe Structural Materials: A Primer and Cost Estimating Methodology”. RAND Corporation, 1991.
- <sup>98</sup> *Roskam, Jan. Airplane Design*. Part VIII. DAR Corporation, 1991.
- <sup>99</sup> US Energy Information Administration. “Monthly Electric Sales and Revenue Report with State Distribution Reports” Jan. 2011.
- <sup>100</sup> Cessna. Skycatcher: Performance and Specifications. <http://www.cessna.com/single-engine/skycatcher/skycatcher-performance.html>. Accessed May 2011.